The Pennsylvania State University

The Graduate School

DESIGN OF CONTACT-AIDED COMPLIANT CELLULAR MECHANISMS FOR USE AS AN ENERGY ABSORBING STRUCTURE

A Thesis in

Mechanical Engineering

by

Jennifer Elizabeth Hyland

Submitted in Partial Fulfillment

of the Requirements

for the Degree of

Master of Science

August 2012

The thesis of Jennifer Elizabeth Hyland was reviewed and approved* by the following:

Mary I. Frecker
Professor of Mechanical Engineering
Thesis Advisor

Martin W. Trethewey
Professor of Mechanical Engineering

Karen A. Thole
Professor of Mechanical Engineering
Department Head of Mechanical and Nuclear Engineering

*Signatures are on file in the Graduate School.

Abstract

Contact-Aided Compliant Cellular Mechanisms (C^3M) are compliant cellular structures with integrated contact mechanisms. While extensive work has been reported in the literature on traditional honeycombs of varying geometries under dynamic and static loading, contact-aided compliant cellular mechanisms under quasi-static crushing or impact have not been previously considered. This thesis addresses this void through the optimization of a hexagonal honeycomb unit cell containing a contact mechanism. The focus of the thesis is on the design, fabrication, and testing of C^3M structures for energy absorbing applications. The addition of contact mechanisms increases cell performance via changing the loading path.

The honeycomb unit cell, defined by a set of variables, is analyzed using finite element analysis. Each unit cell is subjected to an input velocity over some time. Two optimization problems were formulated using MATLAB and finite element analysis to find the best cells for different input velocities. The optimization problem that is formulated maximizes the strain energy per area of a contact-aided compliant cellular mechanism. Two- and three-variable optimization problems are considered, using variables that define the cell geometry and the initial contact gap. It is found that with the addition of a contact mechanism, more strain energy can be absorbed when compared to the same cell without a contact mechanism.

The lost mold rapid infiltration forming (LM-RIF) microfabrication process is used to fabricate C^3M structures from metallic (mesoscale 316L Stainless Steel) materials. The parts are also fabricated through laser micro-machining. Both processes directly fabricate the structures from the use of CAD models. After the parts are fabricated, they are tested experimentally and the results are compared.

Table of Contents

List of Figures…… vi

List of Tables……. xi

Acknowledgements…… xii

Nomenclature…… xiii

Chapter 1: Background and Motivation…… 1
1.1 Introduction 1
1.2 Research Objectives 2
1.3 Literature Review 2
1.3.1 Cellular Structures 3
1.3.2 Compliant Mechanisms 6
1.3.3 Fabrication of Meso-scale Structures 9
1.3.4 Methods for the design and analysis of energy absorbing structures 11
1.4 Thesis Outline 14

Chapter 2: Modeling of Cells and Optimization Problem Formulation…….. 15
2.1 Unit Cell 15
2.2 Modeling the Unit Cell 16
2.2.1 Straight-wall Cell Geometry 16
2.2.2 Curved-wall Cell Geometry 17
2.2.3 Finite Element Analysis 17
2.3 Optimization Problem Formulation 22
2.3.1 Two-Variable Optimization 22
2.3.2 Three-Variable Optimization 23
2.4 Summary 24

Chapter 3: Optimization Results……. 25
3.1 Selection of Bounds for Honeycomb Cells 25
3.1.1 Cell Geometry and Stress Limit 25
3.1.2 Contact Mechanism Width 27
3.1.3 Other User Defined Variables 30
3.2 Constrained Versus Unconstrained by the Manufacturing Process Results 32
3.2.1 Straight-walled Two-variable 32
3.2.2 Straight-walled Three-variable 37
3.2.3 Curved-walled Two-variable 42
3.2.4 Curved-walled Three-variable 48
3.3 Straight-walled Versus Curved-walled Results 55
3.3.1 Two-variable Constrained by the Manufacturing Process 55
3.3.2 Two-variable Unconstrained by the Manufacturing Process 58
3.3.3 Three-variable Constrained by the Manufacturing Process 61
3.3.4 Three-variable Unconstrained by the Manufacturing Process 64

3.4 Summary of Results 67
3.5 Summary 69

Chapter 4: Fabrication and Testing…… 71
4.1 Designs for Fabrication Using LM-RIF 71
4.2 Mask Design 73
4.3 Fabrication using LM-RIF 77
4.4 Fabrication via Laser Micro-machining 79
4.5 Test Rig 81
4.6 Testing Procedure 82
4.7 Results 83
4.8 Summary 90

Chapter 5: Conclusion, Recommendations, and Future work……. 91
5.1 Summary and Conclusions 91
5.2 Contributions 92
5.3 Recommendations for Future Work 93

Appendix A: Node Location Results……... 96

Appendix B: Computer Codes……. 98

Appendix C: Metal Shims Material Testing Report…….. 96

Appendix D: Stress Distribution Plot for Testing Simulations……. 116

Bibliography…….. 123

List of Figures

1.1 An example of contact-aided cellular mechanism showing a contact mechanism inside a cellular cell (right). The cellular cell without the contact mechanism is non-contact cellular structure (left)..... 1
1.2 Fabricated NiTi Honeycomb Structure [4]..... 3
1.3 Example of the sandwich structure [3]..... 4
1.4 Positive (left), Negative (middle), and Zero (right) Poisson's ratio cells [8].. 4
1.5 Cells designed for strain relief [1]..... 5
1.6 Diamond design [20]..... 5
1.7 Chiral Cells [13]..... 5
1.8 MEMs application [9]..... 5
1.9 Star design [22] 6
1.10 Curved Auxetic Cell [2]..... 6
1.11 Combination of traditional and auxetic honeycomb [22] 6
1.12 Grippers that grasp and pull [26] 7
1.13 Dental Floss mechanism [26] 7
1.14 C3M devices with straight walls [11,30]..... 7
1.15 Undeformed (left) and deformed (right) C^3M structures with curved walls where the grey region represents the footprint of the undeformed cell [32]… 8
1.16 Straight and curved walled gripper [33] 8
1.17 Compliant testing bar [9] 9
1.18 Comparison of Fabrication Techniques [58,63] 10
1.19 Mold Fabrication Layering Sequence [29] 11
1.20 Common simulation set-up using an impact plate [68] 12
1.21 FEA set-up for crushing honeycomb using a input displacement [71]..... 12
1.22 Previous research in the design and analysis of honeycomb structures [65]... 13
2.1 Traditional cellular honeycomb used to generate all designs [32] 15
2.2 Curved cellular honeycomb used to generate curved-wall designs [32] 15
2.3 Geometry defining the straight-walled contact-aided unit cells..... 16
2.4 Geometry defining the curved-walled contact-aided unit cells..... 17
2.5 Boundary Conditions Applied Using FEA..... 18
2.6 Cellular structure and boundary conditions applied for FE simulation [11] ... 19
2.7 Location of Beam Element Nodes Used for Parameter Variation Study..... 20
2.8 Normalized Stress at Different Integration Points..... 21
2.9 Optimization Algorithm..... 23
3.1 Geometry defining the straight-walled contact-aided unit cells..... 26
3.2 Stress-strain Curve Utilized for Design..... 27
3.3 Objective Function *E/(H*L)* as a Function of w_{cm} and θ..... 28
3.4 Objective Function *E/(H*L)* as a Function of w_{cm} and *h/l*..... 29
3.5 Dimensions Used to Determine w_{cm}..... 30
3.6 Normalized Convergence History..... 32
3.7 Comparison of θ for the Straight-walled Two-variable Optimization as Input Velocity Increases 34
3.8 Comparison of *h/l* for the Straight-walled Two-variable Optimization as Input Velocity Increases 34

3.9 Comparison of the Maximum Stress for the Straight-walled Two-variable Optimization as Input Velocity Increases Shows the Maximum Stress is Similar at Most Input Velocities……... 35
3.10 Comparison of *E/(H*L)* for the Straight-walled Two-variable Optimization as Input Velocity Increases Shows that the Constrained Cells have a Lower Value for Most Input Velocities……... 35
3.11 Comparison of θ for the Straight-walled Three-variable Optimization as Input Velocity Increases……... 39
3.12 Comparison of *h/l* for the Straight-walled Three-variable Optimization as Input Velocity Increases……... 39
3.13 Comparison of γ for the Straight-walled Three-variable Optimization as Input Velocity Increases……... 40
3.14 Comparison of the Maximum Stress for the Straight-walled Two-variable Optimization as Input Velocity Increases Shows the Maximum Stress is Similar at Most Input Velocities……... 40
3.15 Comparison of *E/(H*L)* for the Straight-walled Two-variable Optimization as Input Velocity Increases Shows that the Constrained Cells have a Lower Value …… 41
3.16 Comparison of θ for the Curved-walled Two-variable Optimization as Input Velocity Increases…… 44
3.17 Comparison of *h/l* for the Curved-walled Two-variable Optimization as Input Velocity Increases……... 44
3.18 Comparison of the Maximum Stress for the Curved-walled Two-variable Optimization as Input Velocity Increases……. 45
3.19 Comparison of *E/(H*L)* for the Curved-walled Two-variable Optimization as Input Velocity Increases……... 45
3.20 Radii of Different Fillets for Varying *h/l* and θ Values Shows that with Increasing *h/l* and Decreasing θ the Radius Increases…….. 46
3.21 *E/(H*L)* Decreases with Increasing Contact Gap for a Constant θ of 40°….. 49
3.22 *E/(H*L)* Decreases with Increasing Contact Gap for a Constant *h/l* of 1.0…. 49
3.23 Comparison of θ for the Curved-walled Three-variable Optimization as Input Velocity Increases……... 52
3.24 Comparison of *h/l* for the Curved-walled Three-variable Optimization as Input Velocity Increases……... 52
3.25 Comparison of γ for the Curved-walled Three-variable Optimization as Input Velocity Increases……... 53
3.26 Comparison of the Maximum Stress for the Curved-walled Three-variable Optimization as Input Velocity Increases……. 53
3.27 Comparison of *E/(H*L)* for the Curved-walled Three-variable Optimization as Input Velocity Increases……... 54
3.28 Comparison of θ for the Two-variable Optimization Constrained by the Manufacturing Process as Input Velocity Increases……. 56
3.29 Comparison of *h/l* for the Two-variable Optimization Constrained by the Manufacturing Process as Input Velocity Increases……. 57
3.30 Comparison of the Maximum Stress for the Two-variable Optimization Constrained by the Manufacturing Process as Input Velocity Increases……. 57

3.31 Comparison of *E/(H*L)* for the Two-variable Optimization Constrained by the Manufacturing Process as Input Velocity Increases……... 58
3.32 Comparison of θ for the Two-variable Optimization Unconstrained by the Manufacturing Process as Input Velocity Increases……. 59
3.33 Comparison of *h/l* for the Two-variable Optimization Unconstrained by the Manufacturing Process as Input Velocity Increases……. 59
3.34 Comparison of the Maximum Stress for the Two-variable Optimization Unconstrained by the Manufacturing Process as Input Velocity Increases…. 60
3.35 Comparison of *E/(H*L)* for the Two-variable Optimization Unconstrained by the Manufacturing Process as Input Velocity Increases…….. 60
3.36 Comparison of θ for the Three-variable Optimization Constrained by the Manufacturing Process as Input Velocity Increases……. 61
3.37 Comparison of *h/l* for the Three-variable Optimization Constrained by the Manufacturing Process as Input Velocity Increases……. 62
3.38 Comparison of γ for the Three-variable Optimization Constrained by the Manufacturing Process as Input Velocity Increases……. 62
3.39 Comparison of the Maximum Stress for the Three-variable Optimization Constrained by the Manufacturing Process as Input Velocity Increases……. 63
3.40 Comparison of *E/(H*L)* for the Three-variable Optimization Constrained by the Manufacturing Process as Input Velocity Increases……... 63
3.41 Comparison of θ for the Three-variable Optimization Unconstrained by the Manufacturing Process as Input Velocity Increases……. 64
3.42 Comparison of *h/l* for the Three-variable Optimization Unconstrained by the Manufacturing Process as Input Velocity Increases……. 65
3.43 Comparison of γ for the Three-variable Optimization Unconstrained by the Manufacturing Process as Input Velocity Increases……. 65
3.44 Comparison of the Maximum Stress for the Three-variable Optimization Unconstrained by the Manufacturing Process as Input Velocity Increases…. 66
3.45 Comparison of *E/(H*L)* for the Three-variable Optimization Unconstrained by the Manufacturing Process as Input Velocity Increases…….. 66
4.1 The designs to be fabricated, a single contact-aided cell (A), a single non-contact cell (B), a 2x2 contact-aided array (C), and a 2x2 non-contact array (D) using the LM-RIF process based on the optimized results in Chapter 3... 74
4.2 The designs to be fabricated, a single straight-walled contact-aided cell (A), a straight-walled single non-contact cell (B), a straight-walled 2x2 contact-aided array (C), and a straight-walled 2x2 non-contact array (D) using the LM-RIF process. …….. 74
4.3 The designs to be fabricated, a single curved-walled contact-aided cell (A), a single curved-walled non-contact cell (B), a 2x2 curved-walled contact-aided array (C), and a 2x2 curved-walled non-contact array (D) using the LM-RIF process……... 75
4.4 Mask layout…….. 76
4.5 Fabrication of C3M structures: the mask (A), the empty mold (B), the filled mold (C) and a finished part (D)…….. 78
4.6 Zoomed in view of the contact mechanism…….. 78
4.7 The same optimized cell fabricated using the raster method (top) and the

vector method (bottom)…… 79
4.8 The three C3M cells, optimized cell (top), straight-walled comparison cell (middle), and curved-walled comparison cell (bottom), fabricated using the raster method…… 80
4.9 The back side of the part showing that the laser did cut all the way through the metal shim……... 80
4.10 Schematic of test rig fabricated for use with the Instron for compression testing…… 81
4.11 Test rig fabricated for use with the Instron for compression testing with a part inserted…….. 82
4.12 The complete test set-up including the test rig and the video camera…….. 83
4.13 Stress-strain curve extracted from the material testing report found in Appendix B used for simulation to compare to test results…….. 84
4.14 Boundary Conditions Applied Using FEA for Second Simulation Run……... 85
4.15 Comparison of Instron Compression Testing and ANSYS Simulation Results for the Straight-walled Comparison Cell……. 86
4.16 Deformed Cell After Compression Testing…….. 86
4.17 Deformed Cell Via Simulation where the Top Wall was not Constrained….. 86
4.18 Comparison of Instron Compression Testing and ANSYS Simulation Results for the Curved-walled Comparison Cell…….. 87
4.19 Comparison of Instron Compression Testing and ANSYS Simulation Results for the Optimized Cell for an Input Velocity of 30 microns/sec for 2 seconds…….. 89
4.20 Comparison of Instron Compression Testing and ANSYS Simulation Results for the Optimized Cell for an Input Velocity of 50 microns/sec for 2 seconds…… 89
5.1 Potential design for a honeycomb structure with a different contact location and design [11]……. 92
5.2 Potential design for a honeycomb structure with multiple contact points [11] 92
5.3 A cellular array, a single cell and a full scale single cell all fabricated via the raster method…… 93
5.4 Four cells cut out of aluminum foil then bent up to a 90° angle…… 93
A.1 Location of Beam Element Nodes Used Reproduced from Figure 2.7…… 94
A.2 Stress Distribution for Node Indicated by ▲……... 94
A.3 Stress Distribution for Node Indicated by ●……... 95
A.4 Stress Distribution for Node Indicated by ■……... 95
D.1 Stress Distribution for the Straight-wall Comparison Cell Deformed Using an Input Velocity of 75 microns/sec for 2 seconds where the Top and Bottom Walls are Constrained to Represent a Unit Cell…….. 118
D.2 Stress Distribution for the Straight-wall Comparison Cell Deformed Using an Input Velocity of 75 microns/sec for 2 seconds where the Top Wall is not constrained…… 119
D.3 Stress Distribution for the Curved-wall Comparison Cell Deformed Using an Input Velocity of 60 microns/sec for 2 seconds where the Top and Bottom Walls are constrained to Represent a Unit Cell…….. 120
D.4 Stress Distribution for the Curved-wall Comparison Cell Deformed Using

an Input Velocity of 60 microns/sec for 2 seconds where the Top Wall is not constrained…… 120
D.5 Stress Distribution for the Optimized Cell Deformed Using an Input Velocity of 30 microns/sec for 2 seconds where the Top and Bottom Walls are constrained to Represent a Unit Cell…….. 121
D.6 Stress Distribution for Optimized Cell Deformed Using an Input Velocity of 30 microns/sec for 2 seconds where the Top Wall is not constrained…….. 121
D.7 Stress Distribution for the Optimized Cell Deformed Using an Input Velocity of 50 microns/sec for 2 seconds where the Top and Bottom Walls are constrained to Represent a Unit Cell……. 122
D.8 Stress Distribution for Optimized Cell Deformed Using an Input Velocity of 50 microns/sec for 2 seconds where the Top Wall is not constrained……. 122

List of Tables

3.1	Limits selected for various design variables……	26
3.2	User Defined Variables and Chosen Values…….	31
3.3	Cell Geometry is Diamond Shaped and *h* Varies for Straight-walled Two-variable Optimization Constrained by the Manufacturing Process……..	36
3.4	Cell Geometry Changes from a Diamond Shape to a Traditional Honeycomb with Increasing Input Velocity for Straight-walled Two-variable Optimization Unconstrained by the Manufacturing Process……	36
3.5	Cell Geometry is Diamond Shaped and *h* Varies for Straight-walled Three-variable Optimization Constrained by the Manufacturing Process……..	41
3.6	Cell Geometry Changes from a Diamond Shape to a More of a Traditional Honeycomb with Increasing Input Velocity for Straight-walled Three-variable Optimization Unconstrained by the Manufacturing Process……..	42
3.7	Cell Geometry Barely Changes Shape with Increasing Input Velocity for Curved-walled Two-variable Optimization Constrained by the Manufacturing Process…….	46
3.8	Cell Geometry Varies in Shape with Increasing Input Velocity for Curved-walled Two-variable Optimization Unconstrained by the Manufacturing Process……..	47
3.9	Cell Geometry Changes from a Diamond Shape to a Curved Honeycomb Design with Increasing Input Velocity for Curved-walled Three-variable Optimization Constrained by the Manufacturing Process……	54
3.10	Cell Geometry Changes from a Diamond Shape to a More of a Traditional Honeycomb with Increasing Input Velocity for Curved-walled Three-variable Optimization Unconstrained by the Manufacturing Process……..	55
3.11	Ideal Cell Shape for Various Input Velocities While Constrained by the Manufacturing Process…….	68
3.12	Ideal Cell Shape for Various Input Velocities While Not Constrained by the Manufacturing Process…….	69
4.1	Dimensions for each of the manufactured C^3M designs……..	73

Acknowledgements

I would like to first gratefully acknowledge the support provided by the National Science Foundation Grant No. 0900368. I would like to thank my advisor Dr. Frecker for her guidance and advice while getting my Masters. I would also like to extend my thanks to Dr. Trethewey for serving as a reader for my thesis.

There are many other people who helped me greatly during my time at Penn State. I would especially like to thank Samantha Cirone for all of her help and guidance in the design of C^3M structures. I would also like to thank Benjamin Hall and Dr. Ted Reutzel at Penn State Applied Research Lab for fabricating the laser micro-machined parts and Brian Babcox and Chris Leh for fabricating the C^3M structures, building the test rig, and assisting in the testing of the parts. I would also like to thank the rest of the C^3M team for their guidance and support, including Dr. Adair and Dr. Lesieutre.

I would also like to thank my fellow EDOG lab members for their support and friendship. Finally, I would like to extend a huge thank you to my friends and family for all of their love and support through my six years at Penn State.

Nomenclature

h = length of horizontal walls
l = length of oblique walls
θ = angle between oblique wall and vertical line
t = in-plane wall thickness
d = out-of-plane wall thickness
H = overall cell height
L = overall cell length
S_c = contact surface
S_t = target surface
γ = contact gap
w_{cm} = contact mechanism width
σ = maximum stress in the cell
σ_{max} = allowable stress
E = modulus of elasticity
r = radius of fillet added to curved cell
h/l_{min} = lower bound for h/l for the optimization problem
h/l_{max} = upper bound for h/l for the optimization problem
θ_{min} = lower bound for θ for the optimization problem
θ_{max} = lower bound for θ for the optimization problem
γ_{min} = lower bound for γ for the optimization problem
γ_{max} = lower bound for γ for the optimization problem
t_{min} = minimum in-plane wall thickness
d_{min} = minimum out-of-plane wall thickness
AR_{max} = Maximum aspect ratio
AR = Aspect ratio

Chapter 1: Background and Motivation

1.1 Introduction

Cellular contact-aided compliant mechanisms (C^3M) are cellular structures with integrated contact mechanisms. Compliant mechanisms are flexible mechanisms that transfer motion, force or energy from an input to an output. Contact-aided compliant mechanisms are mechanisms in which compliant segments come into contact with each other during deformation thus resulting in a change of the load path. Figure 1.1 shows two cellular arrays, one without (left) and one with (right) a contact mechanism.

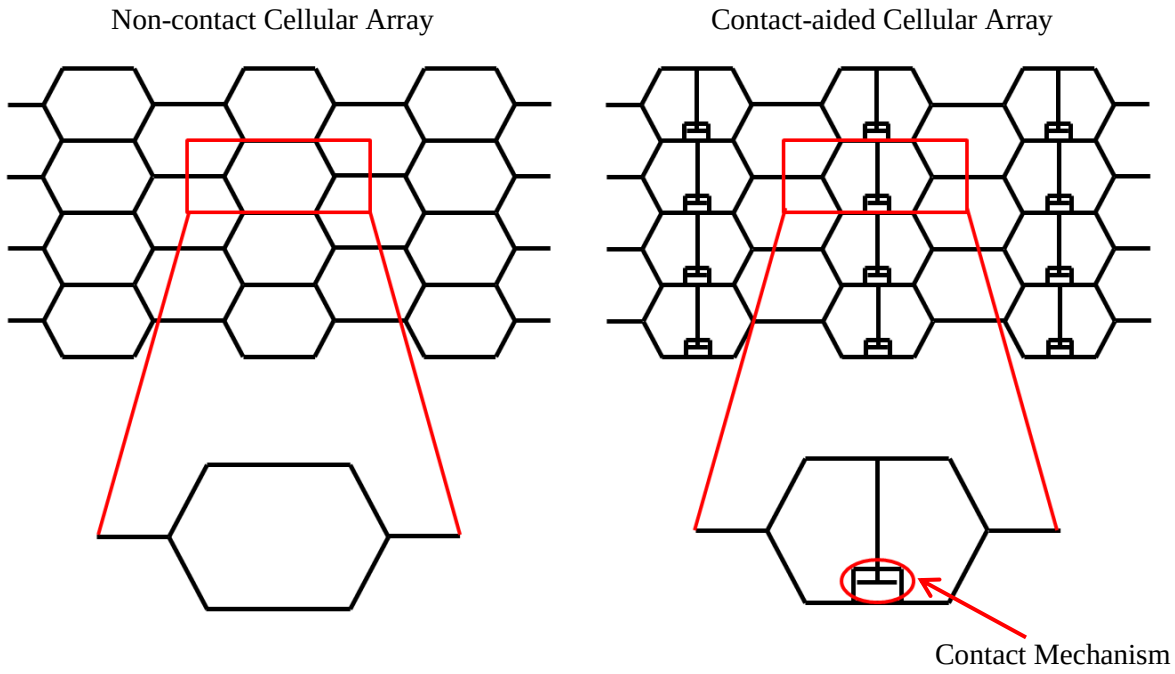

Figure 1.1: An example of contact-aided cellular mechanism showing a contact mechanism inside a cellular cell (right). The cellular cell without the contact mechanism is non-contact cellular structure (left).

The goal of this research is to develop methods for design of energy absorbing structures that utilize contact to take advantage of changing the load path. In the literature, there is a lot of research that has been completed using cellular structures as a way to absorb energy. This work does not use an internal contact mechanism. The use of the contact

mechanism causes a change in the load path. Previously, these C^3M structures were developed for quasi-static high strain applications such as a morphing aircraft skin. The addition of the contact mechanism allowed for greater global strains when compared to the same cell without a contact mechanism. The motivation of this research is to create structures that can absorb more energy by combining cellular structures as a way to absorb energy and the addition of a contact mechanism to change the load path.

1.2 Research Objectives

The objectives of this research involve the design of C^3M structures for use as an energy absorbing structure. The main research objectives are as follows:

1. Explore a range of straight walled C^3M geometries and select the most promising design.
2. Establish a methodology for calculating the energy absorbed.
3. Develop an optimization routine to obtain the best C^3M unit cell dimensions for cells that are capable of dissipating more energy when compared to cells without a contact mechanism.
4. Design cells for fabrication using the LM-RIF micro-fabrication process.
5. Mechanically test the meso-scale C^3M structures and compare with simulation results.

1.3 Literature Review

This section presents a review of the related work in the areas of cellular structures, contact-aided compliant mechanisms, meso-scale fabrication, and methods used for the design and analysis of energy absorbing structures.

1.3.1 Cellular Structures

Nature is full of many different cellular structures including bee's honeycomb, trabecular bone, toucan beak, plant parenchyma, cork and wood. The most common uses of a cellular structure include thermal insulation, buoyancy control, structural applications, and packaging. The reason that there is a wide range of usage for cellular structures is that they can withstand high strains when compared to bulk materials, with the ability to maintain a lower weight. These cellular structures fall into two categories – honeycombs, which are two dimensional, and foams, which are three dimensional [1].

For the purpose of this review, the focus will remain on the two dimensional cellular structure, the honeycomb. Honeycomb structures are most commonly fabricated through molding [2], extrusion and gluing [5], and brazing [4] or epoxying [6] ribbons of material together to create the honeycombs [1]. Ribbons are either flat sheets that are expanded once the glue dries or sheet material that has been bent into the desired shape [5,6]. Glue or epoxy may be used to attach the ribbons to other shapes including tubing [7]. Other fabrication approaches, although less common, include rapid prototyping [8] and laser micromachining [9]. Due to the various fabrication methods, the list of fabrication materials is extensive. Metals such as aluminum [3,6,7] and steel [10,11] can be used along with plastics [8,12,13], glass [9], ceramic [11], rubber [14], and paper [15]. Active materials such as shape memory alloys [2] and shape memory polymers [4] are also used. An example of a fabricated Nitinol honeycomb structure can be seen in Figure 1.2. The Nitinol honeycomb structure was fabricated by joining individual corrugated Nitinol strips through a niobium-based reactive brazing technique [4].

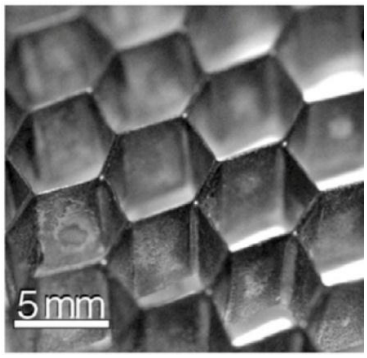

Figure 1.2: Fabricated NiTi Honeycomb Structure [4]

A very common application that utilizes the honeycomb structure is the sandwich structure. The cellular structures are the core components to the sandwich structures as seen in Figure 1.3. The benefit of the sandwich structure is that the area moment of inertia is increased when compared to just the honeycomb layer without increasing weight which results in a high out-of-plane stiffness [1]. The utilization of the sandwich structure can be

seen in nature and in manmade items. Both the iris leaf and the human skull use the sandwich structure [16]. The sandwich structure can also be found in sports equipment [1], aerospace applications [1], structural applications [17], and as a morphing aircraft skin [3,8,18,19].

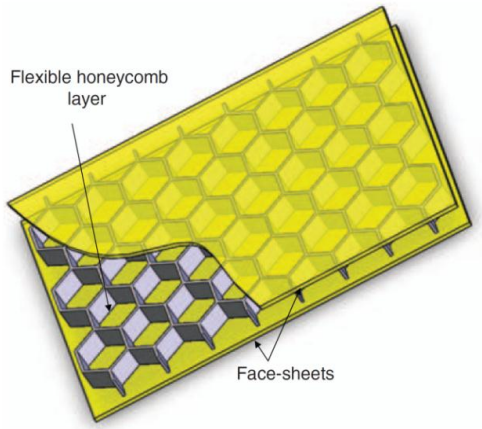

Figure 1.3: Example of the sandwich structure [3]

When looking closer at the honeycomb structure within the sandwich structure, the Poisson's ratio describes the behavior of the deformation of the cell. The Poisson's ratio is the ratio of the displacement in the loading direction to the displacement in the direction perpendicular to the loading. Each honeycomb can be classified as a positive, negative, or zero Poisson's ratio cell. When the cell is stretched in one direction and contracts in the other, the cell has a positive Poisson's ratio. The positive Poisson's ratio is seen in most bulk materials and in traditional honeycombs. Figure 1.4 (left) shows a positive Poisson's ratio cell. As the cells are stretched vertically, they contract horizontally. As shown in Figure 1.4, the positive Poisson's ratio array is created by repeating hexagons. These cells are easy to fabricate by gluing or epoxying ribbons of material together and are easy to fabricate from paper materials [15]. The positive Poisson's ratio cells have a higher out-of-plane stiffness when compared to the negative Poisson's ratio honeycomb [3]. The positive Poisson's ratio cell is useful for in-plane compression, such as lightweight armor, energy absorption application and in smart structures [4]. Other examples of positive Poisson's ratio cellular arrays can be seen in Figures 1.5 and 1.6

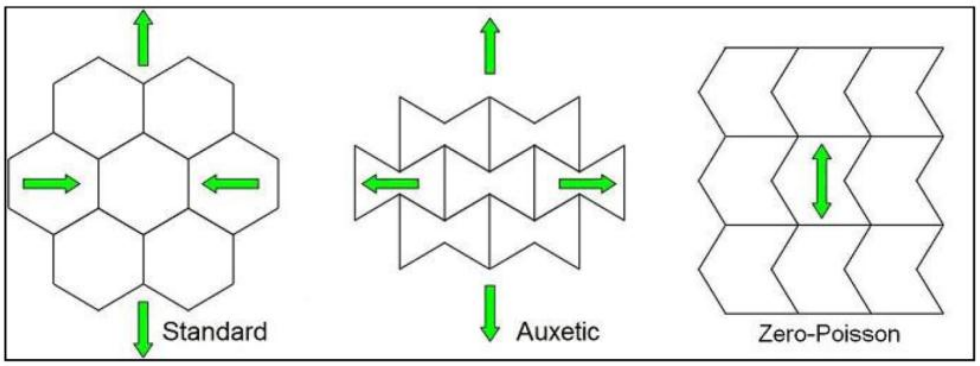

Figure 1.4: Positive (left), Negative (center), and Zero (right) Poisson's ratio cells [8]

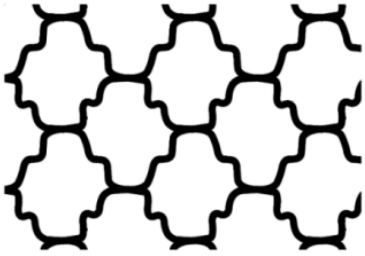

Figure 1.5: Cells designed for strain relief [1]

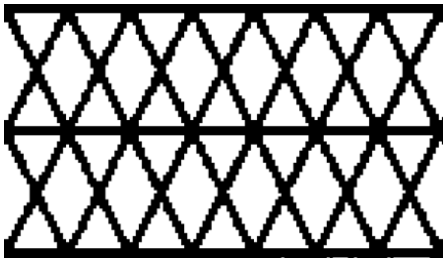

Figure 1.6: Diamond design [20]

When a cell is stretched in one direction and expands in the other, the cell has a negative Poisson's ratio. The negative Poisson's ratio is also known as the auxetic structure or reentrant honeycomb. Figure 1.4 (center) shows a negative Poisson's ratio cell. As the cells are stretched vertically, they expand horizontally. Unlike the positive Poisson's ratio cells, these cells are more difficult to manufacture and are commonly fabricated using molding or extruding techniques [21]. The benefits of the negative Poisson's ratio cells include very large shear moduli and high out-of-plane strength along with large out-of-plane deformations for curved sandwich structures when used as the core material [2,21]. Finite element simulations have also shown that there is a dependence of the in-plane mechanical properties of the auxetic honeycombs when subjected to uniaxial loading [22]. The chiral structure, as seen in Figure 1.7, is a very common auxetic structure that has be analyzed for high-strain applications [12] due to its high out-of-plane compressive strength and resistance to out-of-plane shear loading [21]. Other examples of negative Poisson's ratio cells include the double arrowhead design for MEMs applications as shown in Figure 1.8 [9], the star design shown in Figure 1.9 [23], and the curved auxetic cell for high strain applications, shown in Figure 1.10 [2].

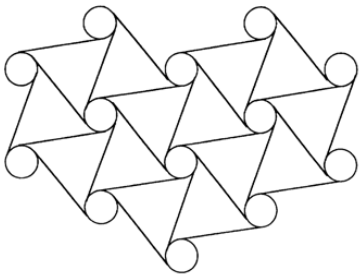

Figure 1.7: Chiral Cells [13]

Figure 1.8: MEMs application [9]

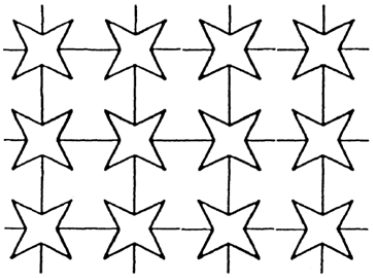

Figure 1.9: Star design [23]

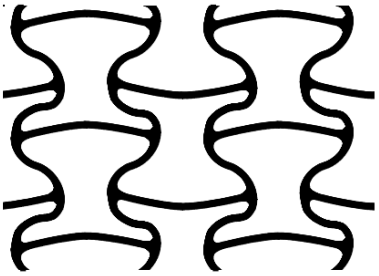

Figure 1.10: Curved Auxetic Cell [2]

When a cell is stretched in one direction and there is no change in the other, the cell has a zero Poisson's ratio. Figure 1.4 (right) shows a zero Poisson's ratio. As the cells are stretched vertically, there is no change in the horizontal direction. These cells are very desirable in applications where one dimensional shape change is desired such as a wing span change in a morphing aircraft [18]. One way to achieve the zero Poisson's behavior is by combining the traditional, positive Poisson's ratio, and auxetic, negative Poisson's ratio, cells into an array as seen in Figure 1.11 [18]. This combination of cells was found to have similar strain and stiffness properties of the traditional honeycomb [18]. The array can be constrained in the direction of loading and the cellular structure stiffness remains unchanged [18].

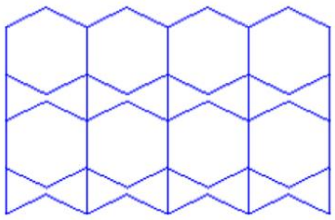

Figure 1.11: Combination of traditional and auxetic honeycomb [23]

1.3.2 Compliant Mechanisms

Compliant mechanisms are flexible mechanisms that transfer motion, force, or energy from an input to and output. One of the benefits of compliant mechanisms is that they can be more reliable with increase resistance to wear and tear due to the fact that they do not have hinge joints [24]. Compliant mechanisms can achieve very high precision. One of the weaknesses of compliant mechanisms is that they may not be able to achieve the same range of motion as a rigid link mechanism [24]. For applications with repeat loading, fatigue could become an issue depending on the application. By ensuring that the mechanism remains within the elastic region, plastic deformation can be avoided even though fatigue cannot be prevented.

One subdivision of compliant mechanisms is contact-aided compliant mechanisms, or CCM. CCM have compliant segments that come into contact with one another during deformation. This contact can be used for path generation [25]. The grippers have the ability to both grasp and pull an object as seen in Figure 1.12 [25]. Contact can also be used to cause an abrupt change the stiffness of a mechanism as seen in Figure 1.13 [26]. The dental floss mechanism becomes stiff to ensure that the floss is taught, but the displacement is limited by a second contact mechanism to ensure that the floss does not break. Contact can also reduce stress concentrations and increase the range of motion via stress relief [11,29,30,31,32]. These CCM can also be used on the meso-scale and are called contact-aided compliant cellular mechanisms or C^3M. These structures have been used to achieve higher global strains by providing stress relief when contact occurs thus keeping the material in the elastic region [11,19,30,32]. An example a C3M structure with straight walls can be see in Figure 1.14. Having contact occur after a certrain deformation that prevents buckling is an expamle of how contact can increase the load bearing capacity of a mechanism [27].

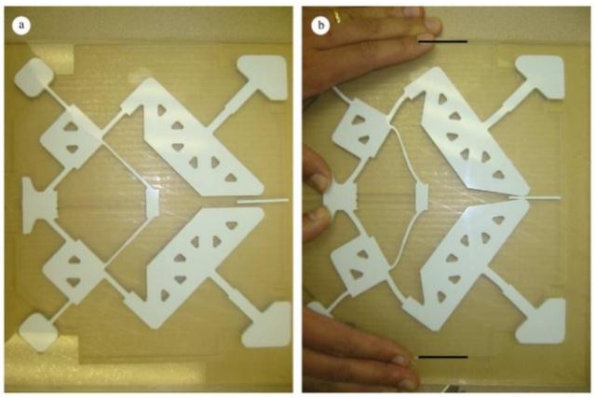

Figure 1.12: Grippers that grasp and pull [25]

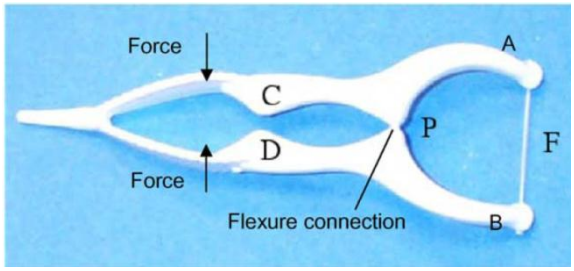

Figure 1.13: Dental Floss mechanism [26]

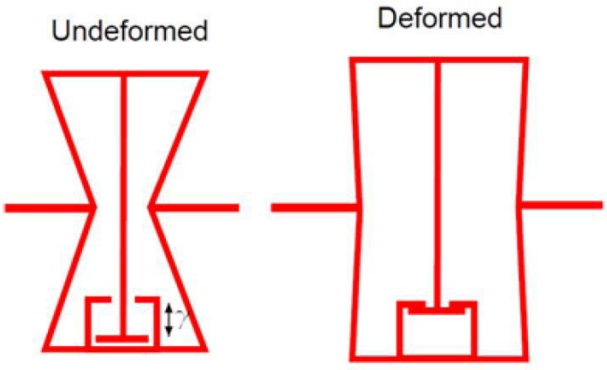

Figure 1.14: C3M devices with straight walls [11,30]

Contact-aided compliant mechanisms can be improved through the use of curved walls in place of straight walls. The use of curved walls helps to reduce stress concentrations while also making the parts easier to manufacture. The use of curved-walls in place of the straight-walls for C^3M improved the global strain of the cell [32]. The C^3M structures with curved walls are always able to achieve higher global strains when compared with the straight-walled C^3M structures [32]. An example of a curved-wall C^3M structure can be seen in Figure 1.15. Zhou *et al.* developed a method for increasing the performance of a compliant mechanism by using shape synthesis of compliant mechanisms using wide curve theory. The method was demonstrated through the optimization of a compliant gripper shown in Figure 1.16. The use of curved walls increased the gripping force by 45% when compared to the gripper with straight walls [33]. Although, gripper design is not a contact-aided; the use of curved walls improve its performance. Xu *et al.* developed a process for shape optimization of compliant mechanisms. The process represents segments of the compliant mechanism topology as Bezier curves, and was demonstrated through the optimization of the compliant gripper. The optimized gripper was found to have 67% improvement over the original design, where a successful design is measured as having a high ratio of flexibility to stiffness [34].

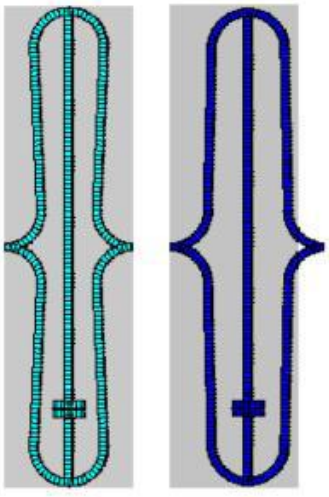

Figure 1.15: Undeformed (left) and deformed (right) C^3M structures with curved walls where the grey region represents the footprint of the undeformed cell [32]

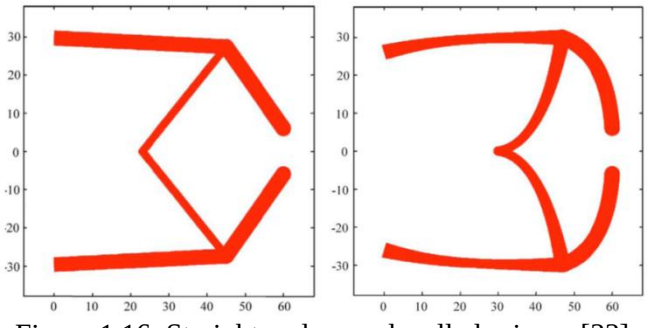

Figure 1.16: Straight and curved walled gripper [33]

1.3.3 Fabrication of Meso-scale Structures

Fabrication techniques are well developed for macro- and micro-scale structures and are actively being developed for nano-scale structures. Between the macro-scale and the micro and nano-scales, there are meso-scale structures. These structures have footprints that are measured in millimeters and features that are measured in microns. Microfabrication has been used to fabricate meso-scale devices from ceramic and stainless steel for MEMs components [35,36,37,38], micro-components including microgears and micropistons [39,40], surgical tools [29,31], and cellular structures with various Poisson's ratios including the compliant testing bar shown in Figure 1.17 [9,11,41,42,43,44,45].

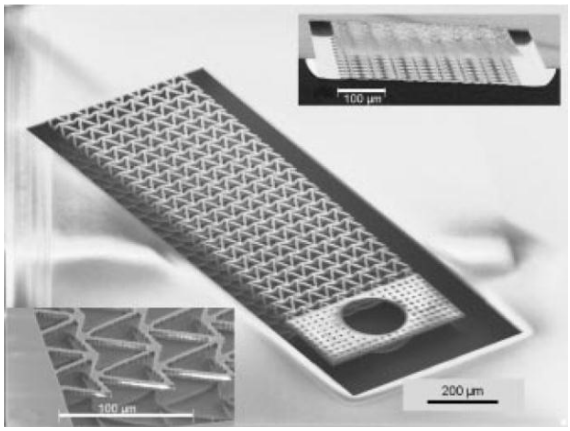

Figure 1.17: Compliant testing bar [9]

There are two types of fabrication techniques, top-down and bottom-up, which can be used to fabricate free standing parts [46]. Top-down fabrication starts with a larger block of material and the material is removed through conventional machining techniques [47]. An example of the top-down technique being utilized is how Mount Rushmore was created. Parts of stone were removed from the mountain leaving just the faces behind. With this technique, only a few parts can be produced at a time [46]. Another major constraint is that the final parts are constrained by the tooling sizes [48]. Bottom-up fabrication uses smaller particles or components to build a bigger structure [47]. Bottom-up fabrication can be broken in to two categories: self-assembly [49] and directed assembly. Self-assembly involves the organization of molecules that result in an organized structure [50]. Examples of self-assembly involve microcontact printing [51] and microtransfer molding [52]. Directed assembly allows the fabrication of large arrays of free standing part. Direct writing is when material is printed like a printer. Rapid prototyping is an example of direct writing [54]. Hot-melt printing, 3D printing, robocasting, and micropen writing are also examples of direct writing [53]. Lithography mold-based methods are also used for directed assembly as seen using the lost mold process

[55, 56]. Lithography mold-based methods are less expensive [57] and allow for a large variety of materials.

Due to the fact that lithography mold-based methods are compatible with the requirements for fabricating the C^3M structures, a novel directed assembly microfabrication technique is being developed, called the lost mold-rapid infiltration forming (LM-RIF) process. The LM-RIF process is being developed by our collaborators on the C^3M project, Dr. James Adair and student, and is summarized here. Figure 1.18, developed by Greg Hayes, further shows the advantages of the LM-RIF process, when compared to other manufacturing processes [58]. The advantages of utilizing LM-RIF include the ability to fabricate large arrays of parts, parts with high aspect ratios, parts with fine edge resolution, 3D parts, and parts out for multiple materials. As seen in Figure 1.18, all of the top-down approaches and most of the bottom-up approaches are not feasible due to their inability to fabricate larger arrays of part. Out of the remaining techniques, only two are capable of 3D fabrication: the LM-RIF process and the EFAB process [59]. The EFAB process is limited to manufacturing parts from only metals. This figure clearly shows that the LM-RIF process is unique and very suitable for the fabrication of the C^3M structures.

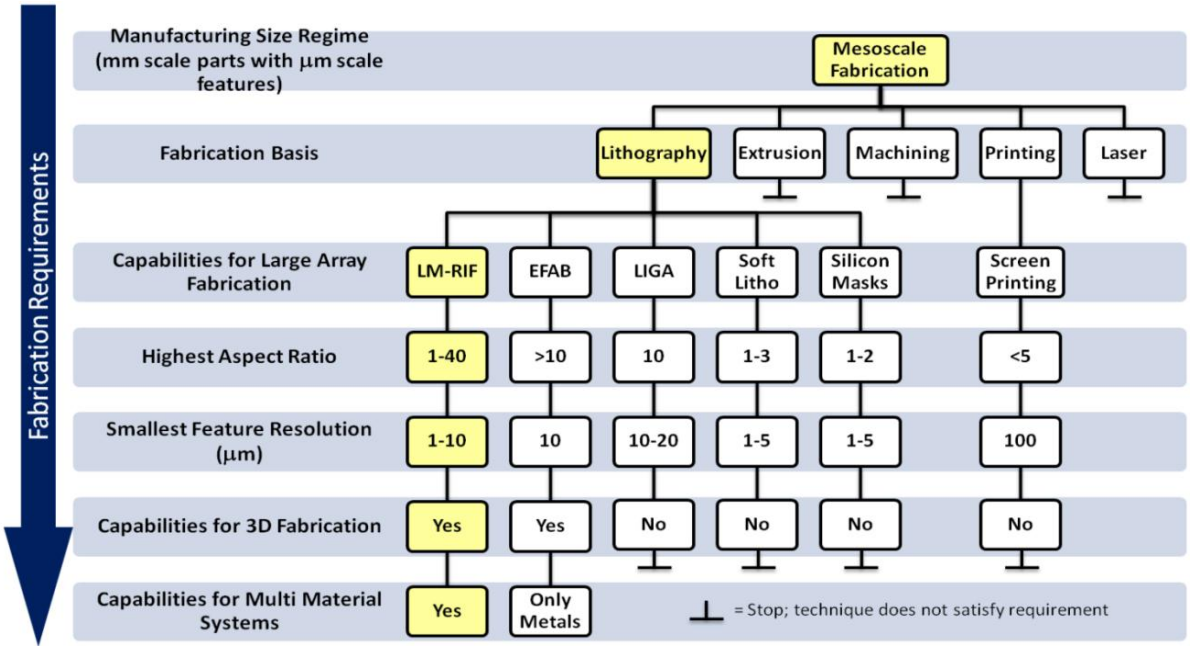

Figure 1.18: Comparison of Fabrication Techniques [58,63]

The process itself consists of four parts: mold fabrication, formulation of the colloidal suspension, casting, and sintering. The mold is fabricated using UV lithography. The layering sequence as seen in Figure 1.19 is followed by the exposure, baking, and developing of the mold. Once the mold is fabricated the colloidal suspension is formulated to use in the casting stage. The casting of the parts is done by hand using a squeegee to ensure that the molds are filled. The final step is sintering which leaves the parts free standing and the mold is lost in the process. More details on the LM-RIF process can be found in [31, 58, 60, 61, 62, 63].

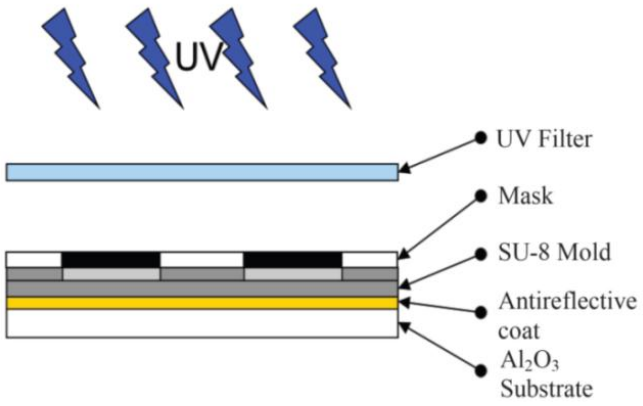

Figure 1.19: Mold Fabrication Layering Sequence [29]

1.3.4 Methods for the design and analysis of energy absorbing structures

Beyond the quasi-static applications mentioned thus far, cellular structures can be used for energy absorption. Key applications include structural protection [64] and shock mitigation [67] which are used in products such as electronic devices, helmets, and various types of shielding. The benefit of using a cellular material over a bulk material is that the cellular material is lightweight but still effective [65].

When reviewing related work, a focus was placed on the crushing honeycomb structures along with other applications that utilized cellular fillers. It was found that filling aluminum tubes with low weight filler improves crash efficiency [70]. The materials that were used for the cellular structures include aluminum [64, 65, 70] and Nitinol shape memory alloy [66].

There are several papers that touch on modeling of the crushing of honeycombs. The finite element method is commonly used for modeling purposes [64, 65, 66, 67, 68, 69, 70, 71]. Large arrays are also used to model the crushing as seen in Figures 1.20 and 1.21 [64, 65, 66, 67, 68, 70, 71]. The approach for modeling the crushing varies from impact or high speed [64, 65, 69, 70] to quasi-static [65, 70, 71]. Some use the application of a constant

force [64] or a displacement [71]. Sometimes voids and defects within the cellular structure are also considered [64, 70].

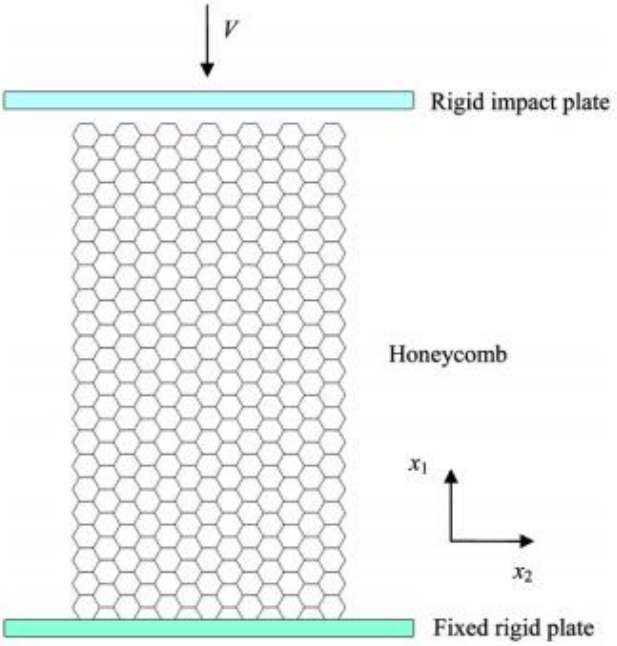

Figure 1.20: Common simulation set-up using an impact plate [68]

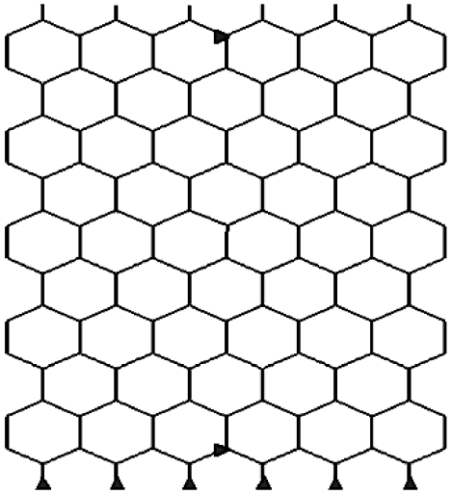

Figure 1.21: FEA set-up for crushing honeycomb using a input displacement [71]

Different tubes, cylindrical and square [69], have also been used to analyze how the honeycomb structure affects the crush resistance of tubes. The honeycomb structure is within the tubes and then tubes are crushed axially and obliquely [69]. The cylindrical and square tubes were crushed both with and without the honeycomb structures and the simulation results were compared to the experimental results [69]. The honeycomb structure has also been simulated utilizing axial crushing where the cells have non-uniform thicknesses or irregular shapes [70].

An extensive summary of work found in the literature can be found in [65] and the summary table can be found in Figure 1.22. Figure 1.22 summarizes several studies based on the design and analysis of honeycomb cellular structures for both static and dynamic loading situations [65]. Previous researchers have found that by increasing the side wall thickness, performance of energy absorption improves [65]. For energy absorption, it was found that an angle of about 10.5 degrees, measured from the vertical to the oblique wall, would absorb the most energy [65]. Whereas, Atli-Veltin and Gandhi found that increasing

the cellular honeycomb angle, the energy absorption capability increased [71]. It was also found that shorter walls, parallel to the direction of crushing, were beneficial in increasing the energy absorption [71]. Also, doubling the wall thickness of the top and bottom walls was shown to increase the crushing strength1.3 times [68] but the walls should only be thick enough to prevent buckling and no thicker [71]. It has also been found that contact between two members in a compliant mechanism can significantly enhance the mechanism's deformation and it has been hypothesized that contact-aided compliant mechanisms have the potential to exhibit a wide range of complex prescribed deformation and energy storage characteristics [72].

Author	**Dynamic Loading**	**Experiments**	**Simulation**	Out-of-Plane	Varying Velocity	Stress-Strain	Crushing Mechanism Definitions	Static Loading	Relative Density Effects	Random / Irregular Geometry	Inclusions / Defects	**In-Plane**	**Varying Geometry**	**Auxetic Geometry**	**Strain Energy Calculations**	**Geometric Effects**	**Force-Displacement**
Ajdari [**5**]	x		x						x				x		x		
Atli [**12**]						x	x	x				x	x		x	x	
Deqiang [**4**]	x	x	x	x	x	x							x				
Hu [**13**]	x				x	x	x					x					
Ju [**20**,**21**,**22**]			x			x		x				x	x	x		x	
Li [**10**]	x		x		x		x			x		x					x
Lira [**23**]			x					x						x		x	
Liu [**9**]	x				x		x					x	x			x	
Nakamoto [**7**,**8**]	x	x	x			x			x		x	x			x		
Pattofatto [**24**,**17**]	x	x	x	x	x	x	x						x			x	x
Sibeaud [**18**]	x	x	x	x			x										
Wang [**3**]	x			x		x							x				
Wu [**16**]	x	x		x	x	x	x	x					x				x
Yamashita [**25**]	x	x	x	x		x											
Yasui [**26**]	x	x		x	x	x											
Zarei [**15**]	x	x	x	x			x								x		x
Zhang [**14**]	x		x		x	x	x		x		x						
Zheng [**6**]	x		x		x		x		x			x					x
Zou [**11**]	x		x		x	x	x					x			x		

Figure 1.22: Previous research in the design and analysis of honeycomb structures [65]

1.4 Thesis Outline

The focus of this research is an investigation of high strain C^3M unit cells with curved cell walls. In this thesis, Chapter 2 presents the C^3M design and the methods used for analysis. Specifically, the geometry of the cells will be defined. Finite element analysis of the C^3M unit cells will be described. Using finite element analysis, the C^3M unit cells will be characterized in terms of their defining variables, and the best fillet size will be determined. Finally, a methodology will be developed to determine the energy of the contact-aided cells.

Chapter 3 will present the predicted results obtained through finite element analysis. First, the bounds for the optimization problems will be determined. The FEA optimization results will be presented and compared. Finally, the ideal C^3M structure for each input velocity will be presented when constrained and not constrained by the manufacturing process.

In Chapter 4, the meso-scale curved C^3M parts will be presented. The designs to be fabricated will be presented. The mask layout for fabrication will be presented, as well as photographs of the fabrication process and final parts. The test rig will be described and the experimental procedure will be presented. Predicted and experimental data will be shown and compared for the different types of cells.

Chapter 5 presents a summary of the work as well as major conclusions drawn. It also presents contributions of the research, and states potential future work.

Chapter 2: Modeling of Cells and Optimization Problem Formulation

This chapter details the process of selecting and modeling the cellular structure. It describes the unit cell geometry as well as the finite element analysis used to calculate strain energy in the cell. The variables that define the unit cell that are presented followed by the constraints imposed using the finite element code. Two optimization problems are then formulated to determine the best C^3M structure.

2.1 Unit Cell

The unit cell is the most basic unit of any cellular structure and is repeated in an array to create a cellular structure [16]. The goal of this research is to design a unit cell that has the ability to absorb maximum strain energy. Each of the designs is based on a traditional cellular honeycomb with a non-dimensional base length of 1, and an overall height of 1, shown in Figure 2.1. The honeycomb design was selected because it is the cellular structure that is most often used as an energy absorbing structure. The honeycomb cell also allows for easy integration of a contact mechanism. Curved-wall designs are also important to consider. As mentioned in Chapter 1, there are many benefits to curved structures such as improved performance including stress relief and ease of manufacturing. The basis for the curved wall designs, along with a corresponding straight walled skeleton (shown as dotted lines), is shown in Figure 2.2. The curved hexagonal cells are created by adding fillets to the corners of the traditional positive Poisson's ratio honeycomb. The size of the fillet will be determined later as part of the optimization procedure.

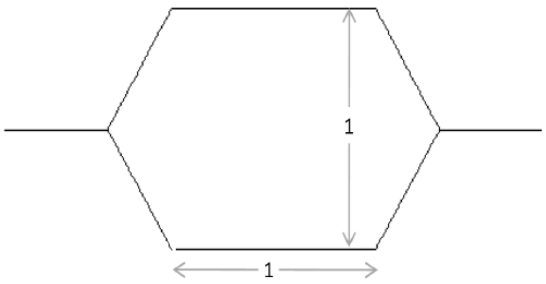

Figure 2.1: Traditional honeycomb cell used as a baseline for all designs [32]

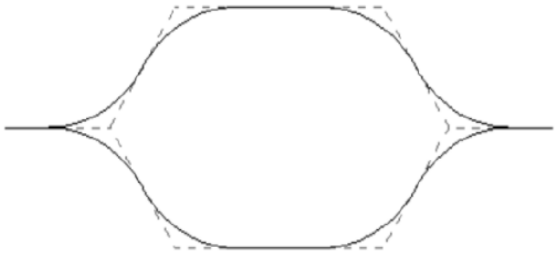

Figure 2.2: Curved honeycomb cell used as a baseline for curved-wall designs [32]

2.2 Modeling the Unit Cell

2.2.1 Straight-wall Cell Geometry

The proposed straight-walled C^3M unit cell and the variables that define its geometry are shown in Figure 2.3. Here, h is the length of the horizontal members in the cell, l is the length of the oblique walls, and θ is the angle measured from a vertical line to the oblique wall (positive when clockwise). The width of the contact mechanism is defined as w_{cm}. The in-plane cell wall thickness is defined by t and the out-of-plane wall depth is defined by d. In Figure 2.3, S_c and S_t are the contact surface and target surface of the contact mechanism, respectively. As the cell is compressed in the horizontal direction, these two surfaces will come into contact, resulting in a change in the loading path. The initial distance between S_c and S_t is defined as the contact gap, represented by γ. The key variables used to define the cell geometry are h, l, θ, and γ.

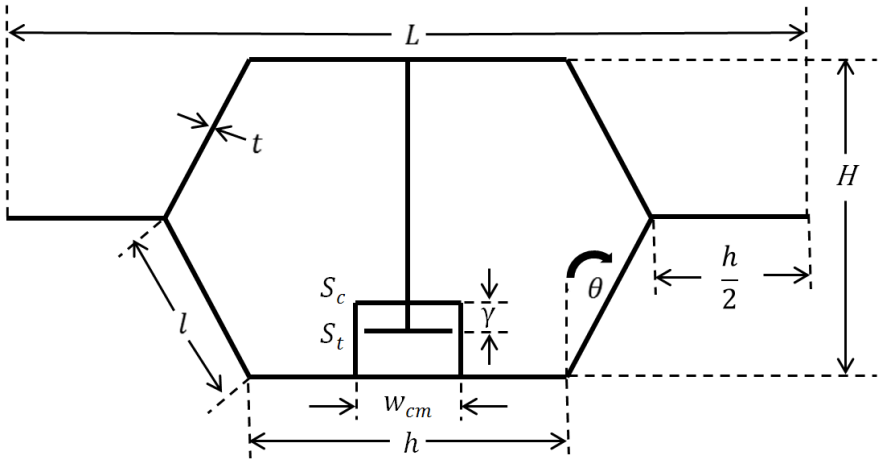

Figure 2.3: Geometry defining the straight-walled contact-aided unit cells

The overall height and width of the cell are referred to as H and L respectively, both of which are functions of h, l and θ. The variables H and L can be calculated using Equations 2.1 and 2.2.

$$H = 2 * l * \cos\theta \quad (2.1)$$

$$L = 2 * (h + l \sin\theta) \quad (2.2)$$

2.2.2 Curved-wall Cell Geometry

The proposed curved-walled geometry is based off of that of the straight-walled cell and can be seen in Figure 2.4. The only difference is that fillets are applied at the six corners of the honeycomb. It was shown in [32] that cells with curved-walls sometimes perform better and are easier to manufacture than those with straight-walls. It was found that as the magnitude of the fillet increased, the performance of the cell, with respect to global strain, increased [32].

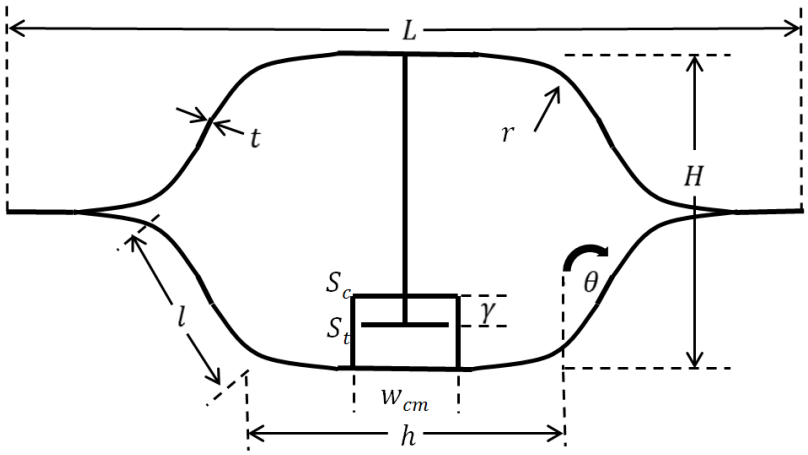

Figure 2.4: Geometry defining the curved-walled contact-aided unit cells

The radius of the fillet is calculated using Equation 2.3. The calculated radius is the maximum radius that is possible in each unit cell. The maximum radius was chosen to ease the manufacturing process along with creating a cell that looks most like the one in Figure 2.4. If the radius was smaller, the cell would look very similar to the straight-walled cell.

$$r = \frac{h}{2} * (1 - w_{cm}) * \tan\frac{90° + \theta}{2} \qquad (2.3)$$

2.2.3 Finite Element Analysis

Finite element analysis was used to model and analyze the unit cells. ANSYS was used as the finite element solver, and the cells walls were modeled using beam elements

(BEAM 23), where the element edge length is equal to 0.1 mm. This means that if *h* was 0.4 mm and there would be 4 elements along the bottom of the cell. As the cell increases in size, the number of elements also increases. Contact was modeled using CONTA172 for the contact surface S_c and TARGE169 for the target surface S_t. To account for the likelihood that the materials will experience deformation beyond the linear elastic range, a nonlinear material model (KINH) is used as the material model. The stress-strain data for the material of interest is input by the designer.

Finite element analysis was used to model and analyze the unit cells as using the boundary conditions shown in Figure 2.5. The cells are constrained in a way that represents the boundaries imposed if the unit cell were part of an infinite 2D cellular sheet. The nodes on the entire bottom edge of the cell are permitted to displace only in the X-direction, i.e., there is no Y-displacement and no rotation. The nodes on the entire top edge of the cell are constrained to have the same Y-displacement, and are fixed in rotation, as indicated by the plus signs in Figure 2.5. The right side of the cell is subjected to an input velocity, *V*, in the negative X-direction, and the left most node of the cell is fixed in the X- and Y-directions.

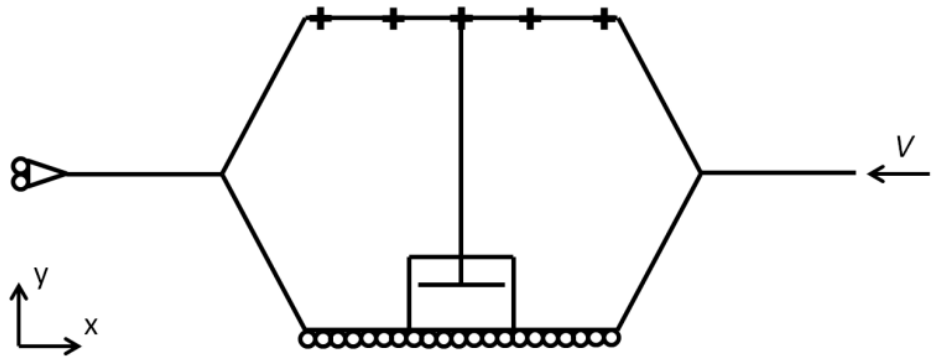

Figure 2.5: Boundary Conditions Applied Using FEA

Using the defined constraints, ANSYS is used to calculate the strain energy for any given cell geometry and input velocity. The total strain energy is determined by summing the element strain energies within the cellular structure when the simulation is complete and the cell has reached its final deformed shape, i.e. when the prescribed input displacement over the prescribed time is reached. Transient FE analysis was used for all simulations. A large deformation analysis was performed.

It is important to look into the stresses seen in the cell. Previous work was done on the analysis for the appropriate stress to use for quasi-static simulations [11]. In the previous work, auxetic cells were analyzed as seen in Figure 2.6. The cells were stretched quasi-statically as seen by the blue arrows on the right-hand side. In auxetic cells, the oblique walls experience compressive axial stress while the contact mechanism experiences tensile stress. Several engineering materials including alloys, ceramics, and some polymers fail at a critical tensile stress. For other materials such as ductile polymers, von Mises stress governs the material failure. Because in the current work, we are using a traditional honeycomb and compressing the cell, the oblique walls will experience compressive axial stress while the contact mechanism will experience tensile stress. In the present analysis, it is assumed that the material failure is due to a normal stress.

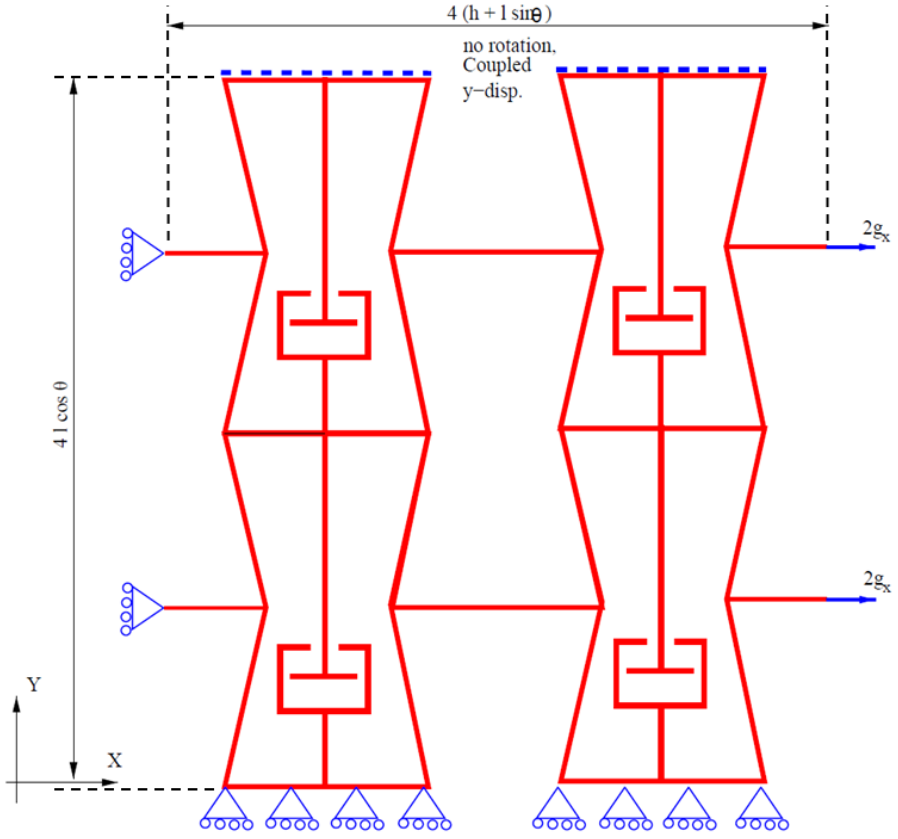

Figure 2.6: Cellular structure and boundary conditions applied for FE simulation [11]

The BEAM23 elements have 15 nodes that can be used to extract stress data from. Two-parameter variation studies were performed to help determine which node to use. The

nodes in the center along the length of the beam do not experience any bending and experience only axial stress. One of these nodes is indicated by the triangle in Figure 2.7. The elements along the edges of the beam experience both axial and bending stresses. These nodes are indicated by the square and the circle in Figure 2.7. The parameters that were varied were *h/l* and θ. In the first study, θ was held constant at 30° and *h/l* was varied from 0.5 to 1.5 in increments of 0.05. In the next study, *h/l* was held constant at 1.0 and θ was varied between 5° and 80° in increments of 5°. For each set of parameters, the input velocity was varied from 0.025 mm/s to 0.125 mm/s in increments of 0.0125 mm/s using the boundary conditions shown in Figure 2.5. The stresses of the three nodes were normalized to the stress limit, σ_{max}. Figure 2.8 shows the case where *h/l* is equal to 0.5 and θ is equal to 30°. The shapes in Figure 2.8 correspond to the node locations found in Figure 2.7. When the other cases were analyzed, the results were all very similar. The maximum stress was always located at the first node which is indicated by the square; therefore the stress at this node was used to define σ in the optimization problem. The stress plots for each node location from ANSYS are shown in Appendix A.

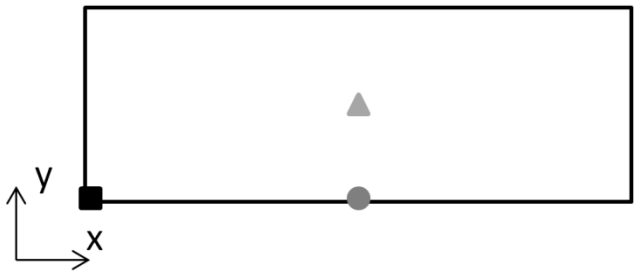

Figure 2.7: Location of Beam Element Nodes Used for Parameter Variation Study

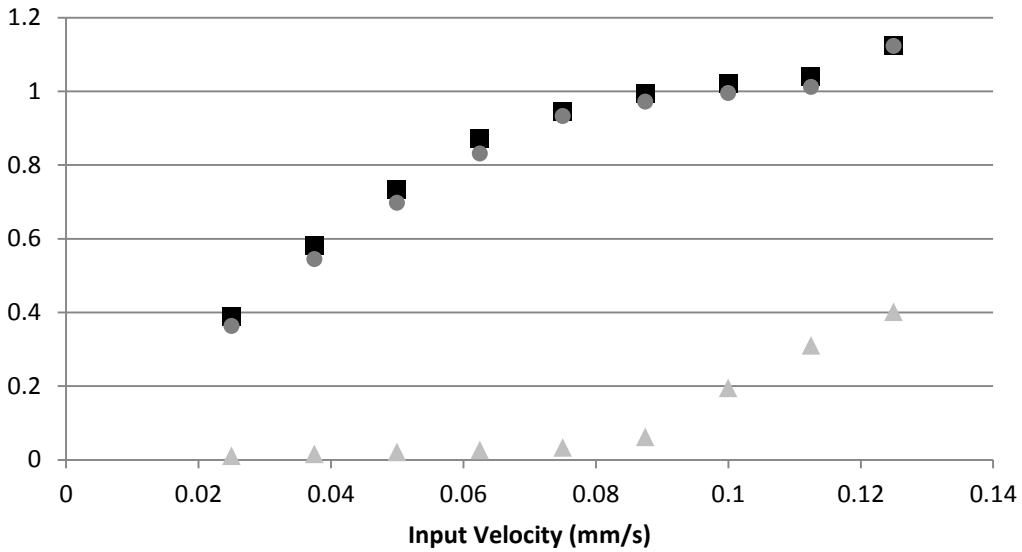

Figure 2.8: Normalized Stress at Different Integration Points

To validate the strain energy, *E*, results from ANSYS, several simulations were run. When within the elastic limit of a material, the energy in the cell is the same as the area under the force-deflection curve. When moving into the plastic region, the value of the energy of the cell will be larger than the area under the force-deflection curve due to plastic deformation. Four different cases were run comparing a contact-aided cell to a non-contact cell. For all cases, the l was set to 4 mm, h was set to 4.4 mm and θ was set to 60°. The input velocity was varied to control the maximum stress in the cell but was always applied over a time of 2 seconds. The contact gap was also varied to ensure that contact would occur. To calculate the area under the curve, the trapezoidal rule was utilized. For the first set, the cell was kept within the elastic limit of the material model. The input velocity was chosen to be 0.005 mm/s. For the non-contact cell, the ratio of the strain energy, *E*, calculated by ANSYS to the area under the curve is 1.00078. For the contact-aided cell, with a contact gap of 15 microns, the ratio of the strain energy, *E*, to the area under the curve is also 1.00078. For the next set, the cells maximum stress was over the elastic limit of the cell. To achieve this, the input velocity was chose to be 0.025 mm/s. For the non-contact cell, the ratio of the strain energy, *E*, calculated by ANSYS to the area under the curve is 1.00087. For the contact-aided cell, with a contact gap of 80 microns, the ratio of the strain energy, *E*, to the area under the curve is 1.00114. As expected, when moving into the plastic region, the cell has a higher energy when compared to the area under the curve.

2.3 Optimization Problem Formulation

2.3.1 Two-Variable Optimization

In order to determine the best possible C^3M unit cell geometry for a given scenario, an optimization problem was formulated. First, two design variables are considered, h/l and θ, and the initial contact gap, γ, is held constant. The non-dimensional parameter h/l is used while l is held constant. The variable σ is the maximum stress found in any given cell. The variables h/l_{min} and h/l_{max} are the lower and upper bounds for the non-dimensional paramenter h/l. The variables θ_{min} and θ_{max} are the lower and upper bounds for the angle θ. The maximum allowable stress, σ_{max}, is determined by the user based on the material used. The values of these variables, h/l_{min}, h/l_{max}, θ_{min}, θ_{max}, σ_{max}, will be determined in Chapter 3.

For the two-variable optimization problem, the problem formulation is shown in Equation 2.4. The objective function is formulated to maximize the strain energy of the cell per area. The area is defined as the effective rectangular area occupied by the cell, or ($H*L$), where H and L are found from Equations 2.1 and 2.2. The solution to this optimization problem will have a maximum value of $E/(H*L)$ for the prescribed input velocity. $E/(H*L)$ was chosen as the objective function in an effort to find the smallest cellular structure that could absorb the most energy. This could be important in applications where the space for the energy-absorbing cellular structure is limited.

$$\begin{aligned} &\text{Minimize:} && -E/(H*L) \\ &\text{Subject to:} && h/l_{min} \le h/l \le h/l_{max} \\ & && \theta_{min} \le \theta \le \theta_{max} \\ & && \sigma \le \sigma_{max} \\ &\text{Variables:} && h/l,\ \theta \end{aligned} \tag{2.4}$$

The optimization was performed using the *fmincon* function in the Optimization Toolbox in MATLAB. *Fmincon* is a gradient-based solver, which is ideal for problems

whose derivatives cannot be calculated explicitly. Within the optimizer, the finite element based solver is called to calculate the sum of the element strain energies, E. Figure 2.9 shows the optimization algorithm. By using a large number of different starting points, and selecting the solution with the best objective function, it is likely that a global optimum is found. Convergence is obtained using a tolerance of 0.001 on the objective in Equation 2.4. All computer codes can be found in Appendix B.

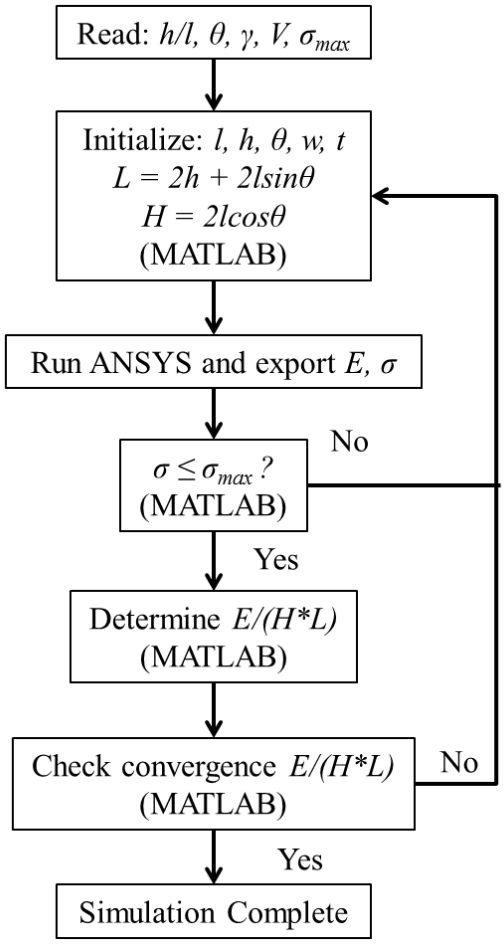

Figure 2.9: Optimization Algorithm

2.3.2 Three-Variable Optimization

To fully exploit the benefit of the contact mechanism, the contact gap, γ, is added as a variable in the optimization problem. The variable γ_{min} and γ_{max} represent the lower and

upper bounds imposed on the contact gap, γ, and will be determined in Chapter 3. The three-variable optimization problem can be seen in Equation 2.5

$$\begin{aligned} &\text{Minimize:} && -E/(H*L) && (2.5)\\ &\text{Subject to:} && h/l_{min} \le h/l \le h/l_{max} \\ & && \theta_{min} \le \theta \le \theta_{max} \\ & && \gamma_{min} \le \gamma \le \gamma_{max} \\ & && \sigma \le \sigma_{max} \\ &\text{Variables:} && h/l,\ \theta,\ \gamma \end{aligned}$$

The same optimization problem solution algorithm is used for the three-variable optimization problem. The upper and lower limits on the geometric variables can be adjusted by the designer based on the intended manufacturing process.

2.4 Summary

This chapter has described the modeling of the C^3M structure and the formulation of the optimization problem. It first introduced the straight-walled unit cells and showed the process by which the curved-walled cell was created. It showed the geometry of the unit cells as well as the modeling of the unit cell using finite element analysis. The designs were then used to implement an optimization procedure in order to determine the best possible C^3M structure. The objective function was shown, along with the variables to be optimized. The optimization algorithm was presented. The results from both cell types and optimization problems will be presented in Chapter 3.

Chapter 3: Optimization Results

This chapter presents the results from the optimization problems presented in Chapter 2. It explains what bounds were selected for the optimization problem and why they were chosen. The results are then presented and compared.

3.1 Selection of Bounds for Honeycomb Cells

In order to run the optimization problem described in Section 2.3, the upper and lower limits on the design variables need to be determined. Some limits are determined by the manufacturing constraints others are determined by the design.

3.1.1 Cell Geometry and Stress Limit

The variables that govern the cell geometry are h/l, θ, and γ. Figure 3.1 is reproduced from Chapter 2 to show the cell's defining variables. Table 3.1 shows the limits selected for various design variables. In all of the optimization problems, l is held constant at 4 mm to ensure that the cell is large enough to fabricate. The upper limit on h/l is based on previous work on designing C^3M with curved-walls [73], where it was found that cells with h/l larger than 1.5 became difficult to manufacture. The limits on θ were selected to ensure that the cell maintains the traditional honeycomb shape while keeping the cell tall enough to include the internal contact mechanism. When θ becomes less than zero, the cell becomes auxetic and behaves like a negative Poisson's ratio cell. When θ becomes greater than 80°, the cell is too short to include the contact mechanism.

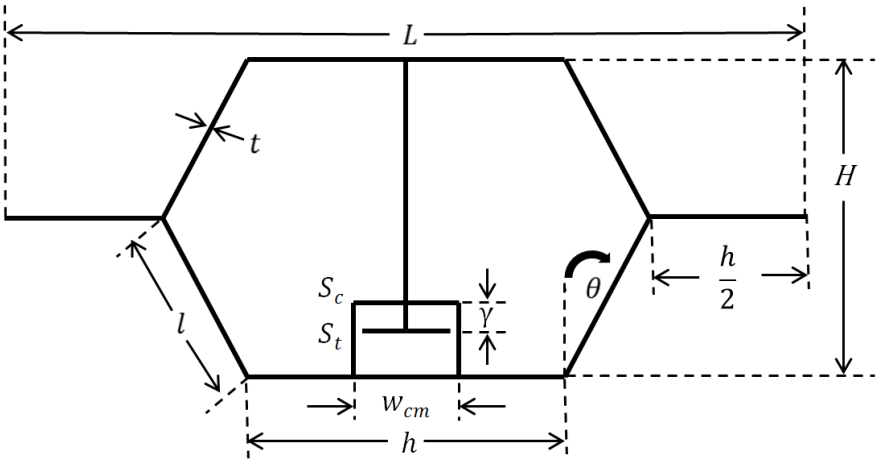

Figure 3.1: Geometry defining the straight-walled contact-aided unit cells

Table 3.1: Limits selected for various design variables

Variable	Value
h/l_{max}	1.5
θ_{min}	0°
θ_{max}	80°
γ_{min}	0.08 mm
γ_{max}	0.25 mm
σ_{max}	832 MPa

The contact gap, γ, has a lower limit of 80 microns because this is the expected minimum that can be reliably manufactured using a meso-scale fabrication process currently being developed as part of this project [31, 63]. The upper limit was selected because it was found that beyond a contact gap of about 240 microns, the contact mechanism no longer benefited the cell. These limits can be adjusted by the designer based on the intended manufacturing process.

The optimization problem also requires that the user inputs a maximum allowable stress for the cell to limit the deformation of the cell. The stress limit, σ_{max}, was selected to so that the maximum element axial stress is within the non-linear elastic region but will not experience failure; it can be thought of as the product of a scaling factor and the yield stress of the material. Meso-scale stainless steel will be used for the fabrication of these C^3M parts. The complete stress-strain behavior of the meso-scale stainless steel is not yet known, but it is known that the initial modulus is approximately 200 GPa [61,62]. A material model for

0.62% stainless steel alloy was selected that has a very similar initial modulus [74]. Figure 3.2 shows the stress-strain curve that was utilized for the design of these C^3M structures.

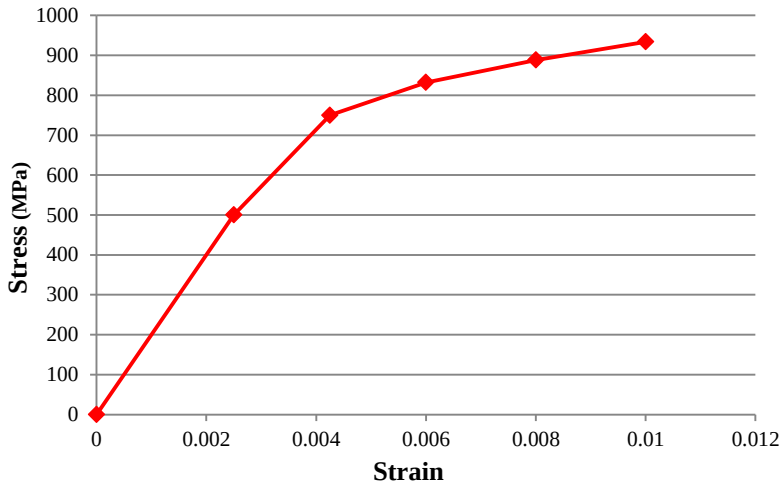

Figure 3.2: Stress-strain Curve Utilized for Design

The other bound that needs to be determined is h/l_{min}. In order to determine this lower limit, the contact mechanism geometry needs to be analyzed.

3.1.2 Contact Mechanism Width

A number of FEA on honeycomb cells were performed to determine the effect of the contact mechanism width. Several values of h/l were used while γ was set to 0.08 mm, and the input velocity, V, was set at 0.1 mm/s. The cell angle, θ, was varied along with the width of the contact mechanism, w_{cm}, as a percentage of h. θ was varied between 20° and 35° while w_{cm} was varied between 30% and 90% of h. Figure 3.3 shows the case where h/l is set to 1.2. As shown in Figure 3.3, as the cell angle increases, the objective function is higher for smaller contact mechanism widths. For a θ of 20°, contact just occurs for the given input. As the angle increase, contact occurs sooner and improves the objective function. The smaller contact mechanism widths see more deformation within the contact mechanism, whereas the larger widths result in more deformation within the cell.

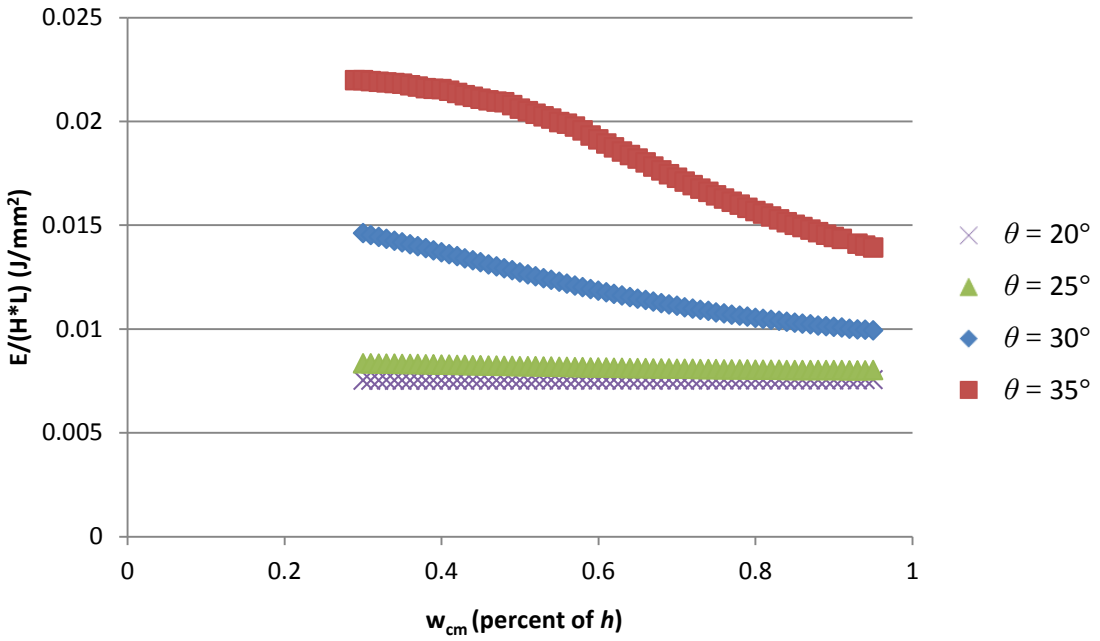

Figure 3.3: Objective Function *E/(H*L)* as a Function of w_{cm} and θ

To confirm that the objective function is always better for smaller widths, θ was held constant at 35° and *h/l* was varied from 1.0 to 1.5. Again, w_{cm} was varied between 30% and 90% of *h*. As shown in Figure 3.4, as *h/l* decreases, the objective function is higher for smaller contact mechanism widths. Both figures show that the ideal contact mechanism has a smaller width.

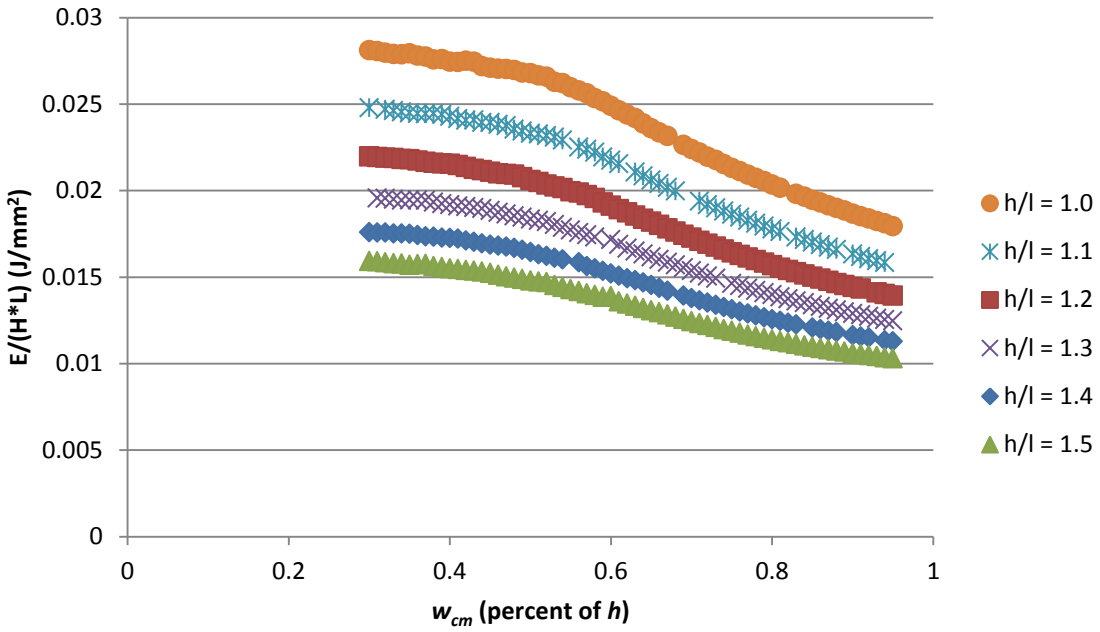

Figure 3.4: Objective Function *E/(H*L)* as a Function of w_{cm} and *h/l*

The other constraint that affects the contact mechanism is implied by the manufacturing process. To ensure that the parts are manufacturable, the overall contact mechanism width needed to be determined. Figure 3.5 shows the key dimensions of the contact mechanism. Length A is set to 0.2 mm while dimension B is set to 0.51 mm. A is chosen so that there will be a sufficient gap for reliable manufacturing. The overlap, dimension B, is chosen so the contact mechanism will be large enough to support the deformation of the cell without failure. The overall contact mechanism width is calculated using Equation 3.1.

$$w_{cm} = 4A + 2B + 2t \tag{3.1}$$

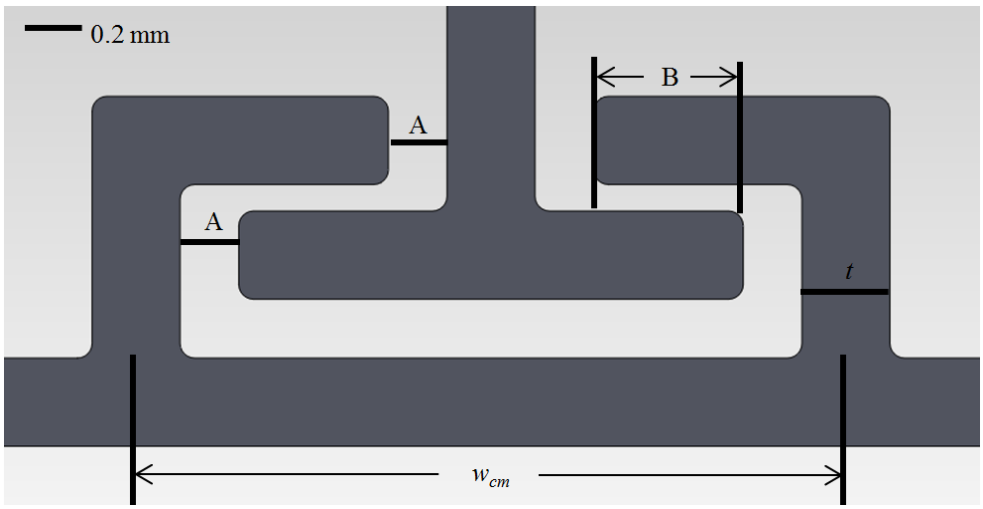

Figure 3.5: Dimensions Used to Determine w_{cm}

Based on the above dimensions, the lower bound for *h/l* was determined to be 0.65. This value was calculated assuming *t* to be 0.3 mm, a manufacturable thickness, and that the contact mechanism would be no larger than 93% of the base, to ensure enough space between the contact mechanism and the oblique wall. The contact mechanism width, w_{cm}, will then always be fixed at 2.42 mm. As shown in Figures 3.3 and 3.4, as w_{cm}, as a percentage of *h*, decreases, the objective function improves. So as *h/l* increases, the contact mechanism will become a smaller percentage of *h* and performance will improve. A second lower bound was set to 0.08 for parts that are not constrained by the manufacturing process to ensure that if a tall and slim cell is optimum, the cell would be a possible solution. For this lower bound, it is assumed that w_{cm} will always be 30% of *h* because that is where the objective function is maximum according to the results shown in Figures 3.3 and 3.4.

3.1.3 Other User Defined Variables

Because the optimization problem allows a user to vary parameters, the limits for the cells can vary greatly. In this study the wall thickness, *t*, the wall depth, *w*, and the length of the oblique walls, *l*, are all held constant as shown in Table 3.2. The wall thickness, *t*, was chosen because the manufacturable range for the in-plane thickness is from 200 to 500 microns [63]. The wall depth, *d*, was chosen because the manufacturable range for the out-of-plane thickness range is from 300 to 500 microns [63]. When contact gap, γ, is held

constant, it is held constant at 90 microns. By choosing a contact gap of 90 microns, contact will always occur for the cell geometries considered. The input velocity is varied by changing the applied input displacement over a time of 2 seconds. The input velocities were increased to a point where the FE analysis would no longer converge.

Table 3.2: User Defined Variables and Chosen Values

Variable	Input Value
l	4 mm
t	300 microns
d	400 microns
V	0.025 to 0.175 mm/s

Due to the possibility of finding local minima, several different starting points were chosen. For the runs considering the constrained contact mechanism width, 162 starting points were utilized. The starting values for *h/l* ranged from 0.65 to 1.5 in increments of 0.05. The starting values for θ ranged from 0° to 80° in increments of 10°. For the problems where the contact mechanism width was unconstrained by the manufacturing process, 73 different starting points were selected. The starting values for *h/l* ranged from 0.08 to 1.5 in increments of 0.02. The starting values for θ ranged from 0° to 80° in increments of 10°. Figure 3.6 shows the convergence history for one of the runs completed. The values are normalized with respect to the starting point for each value. *E* increases, and at a faster rate, when compared to *(H*L)* which decreases. This combination results in a rapid increase in *E/(H*L)* over the convergence history.

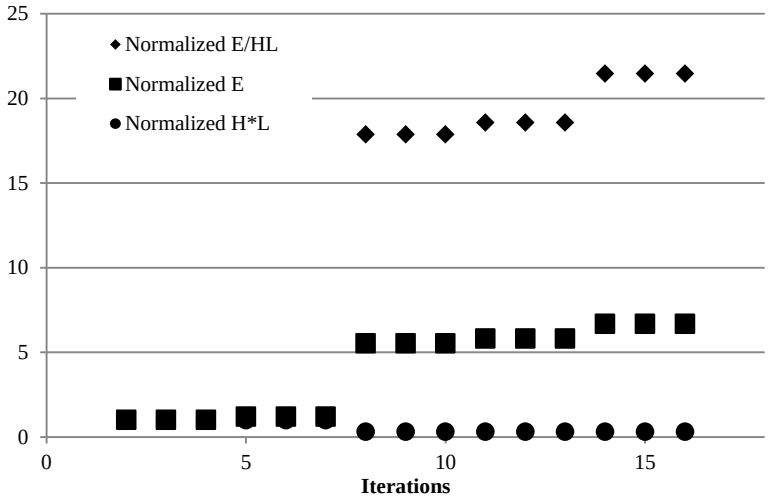

Figure 3.6: Normalized Convergence History

3.2 Constrained Versus Unconstrained by the Manufacturing Process Results

For the two-variable optimization problem, two different problems were considered. The first run was where the contact mechanism geometry was constrained by the manufacturing process. The second run was completed where the contact mechanism geometry was not constrained. The optimization algorithm has been run for the range of starting points over the range of input velocities. For all figures in Section 3.2, the results, where the contact mechanism geometry is constrained by the manufacturing process, are indicated by the red squares. The results, where the contact mechanism geometry is not constrained by the manufacturing process, are indicated by the blue diamonds. Each point on the plot represents the optimal design for that particular input velocity.

3.2.1 Straight-walled Two-variable

For the constrained contact mechanism width designs, the optimum cell wall angle is always approximately 80°, as shown in Figure 3.7. As the input velocity increases, the optimal *h/l* changes very little until a velocity of 0.1 mm/s, as shown in Figure 3.8. The large change in *h/l* is attributed to the values selected for the stress limit. If the stress limit is increased, the optimal value of *h/l* stays at the lower limit, and if the stress limit is decreased, the optimal value of *h/l* approaches the upper limit. Figure 3.9 shows that the

maximum stress in the optimal cell tends to increase with an increase in input velocity. It was also observed that the maximum elemental strain energy in the cells is located in the contact mechanism for all cases. The optimal objective function values are shown in Figure 3.10. The optimal cell geometries as a function of input velocity can be seen in Table 3.3.

For the unconstrained contact mechanism width designs, the results show that as the input velocity increases, the optimum cell wall angle, θ, decreases as shown in Figure 3.7. As the input velocity increases, the optimal *h/l* changes very little until a velocity of 0.1375 mm/s as shown in Figure 3.8. Again, the jump in *h/l* is attributed to the values selected for the stress limit. Figure 3.9 shows that the maximum stress in the optimal cell increases with an increase in input velocity. By comparing the blue diamonds in Figures 3.8 and 3.9, it can be seen that the designs in which the maximum stress is at or near the limit correspond to those with *h/l* near the upper limit. It was also observed that the maximum element strain energy in the cells is located in the contact mechanism for the cells with a small *h/l* value, while the maximum strain energy is located at the corners where the side tabs meet the honeycomb for cells with large *h/l* values. This large change in *h/l* results in a large change in *E/(H*L)* because as *h/l* increases, *(H*L)* increases. The optimal objective function values can be seen in Figure 3.10. The optimal cell geometries as a function of input velocity can be seen in Table 3.4. As the stress in the cell increases with increasing input velocity, the cell transitions from nearly a diamond shape to a honeycomb shape. The transition to a honeycomb shape is achieved by an increasing *h/l* and decreasing θ. As reported in [75], the hexagon shape and the triangle shape have approximately the same energy absorption per unit mass. The nearly diamond shape that is the optimized design presented here can be thought of as simply two triangles once contact occurs.

The comparison of the straight-walled two-variable results is important. Figure 3.8 shows that for *h/l*, most of the results jump between the two bounds set for the optimization problem. For most input velocities, the maximum stress is very similar. The constrained contact mechanism width designs have a lower *E/(H*L)* compared to the unconstrained contact mechanism width designs as shown in Figure 3.10. This is a result of the constraint on the width of the contact mechanism. The designs that are unconstrained by the manufacturing process have a contact mechanism that is always 30% of *h*, whereas the

designs that are constrained by the contact mechanism have a contact mechanism that ranges between 40% and 93% of *h*.

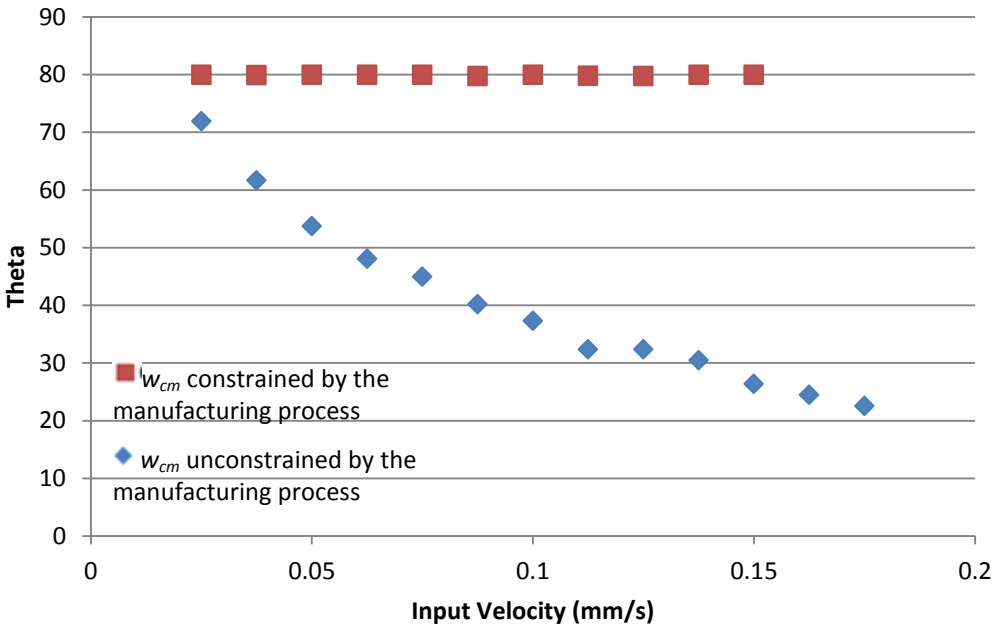

Figure 3.7: Comparison of θ for the Straight-walled Two-variable Optimization as Input Velocity Increases

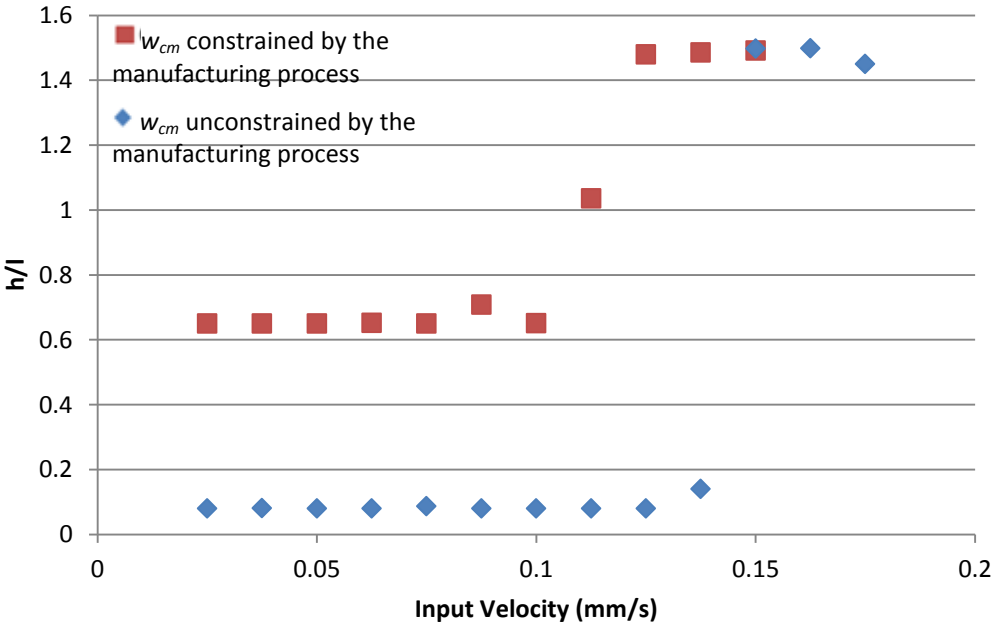

Figure 3.8: Comparison of *h/l* for the Straight-walled Two-variable Optimization as Input Velocity Increases

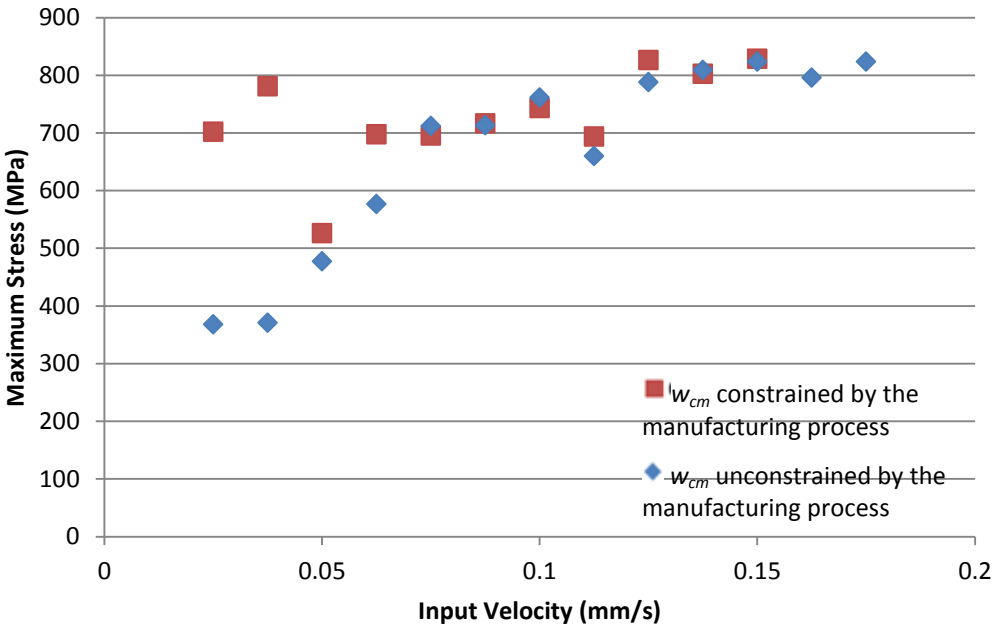

Figure 3.9: Comparison of the Maximum Stress for the Straight-walled Two-variable Optimization as Input Velocity Increases Shows the Maximum Stress is Similar at Most Input Velocities

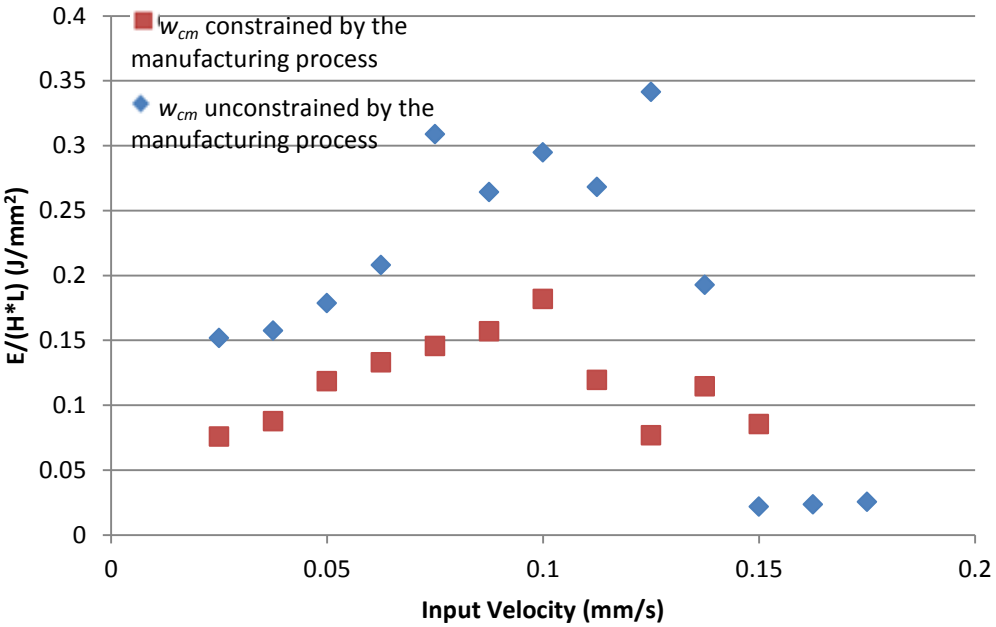

Figure 3.10: Comparison of *E/(H*L)* for the Straight-walled Two-variable Optimization as Input Velocity Increases Shows that the Constrained Cells have a Lower Value for Most Input Velocities

Table 3.3: Cell Geometry is Diamond Shaped and *h* Varies for Straight-walled Two-variable Optimization Constrained by the Manufacturing Process

Input Velocity (mm/s)	Cell Shape ——— 4mm
0.025 – 0.1	
0.1125	
0.125-0.1625	

Table 3.4: Cell Geometry Changes from a Diamond Shape to a Traditional Honeycomb with Increasing Input Velocity for Straight-walled Two-variable Optimization Unconstrained by the Manufacturing Process

Input Velocity (mm/s)	Cell Shape ——— 4 mm	Input Velocity (mm/s)	Cell Shape ——— 4 mm
0.025	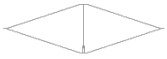	0.1	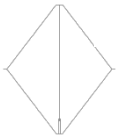
0.0375	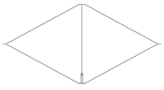	0.1125	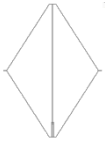
0.05	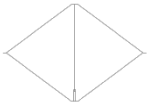	0.125	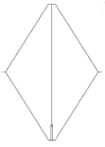
0.0625	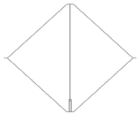	0.1375	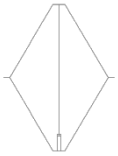
0.075	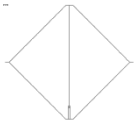	0.15	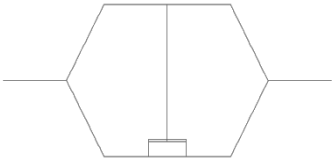
0.0875	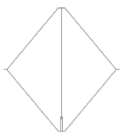	0.1625	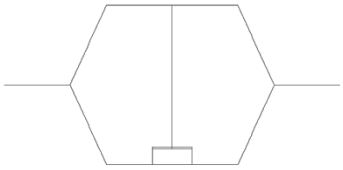

A benefit of employing the contact mechanism can be illustrated by considering, for example, the solution for the input velocity of 0.15 mm/s and comparing the optimized contact-aided cell and the same cell without a contact mechanism. The contact-aided cell has a *E/(H*L)* of 0.02176 J/mm^2 and the cell without a contact mechanism has a *E/(H*L)* of 0.01354 J/mm^2. Both cells have the same *H*L* value although the contact-aided cell also has slightly more material than the non-contact cell. This shows that the use of contact improves the strain energy absorption of the structure by changing the load path of the cellular structure. For other cell geometries, an improvement is always seen with the addition of a contact mechanism as long as contact occurs.

3.2.2 Straight-walled Three-variable

The optimization problem was expanded to include the contact gap, γ, as a variable. Again, the results where the contact mechanism geometry is constrained by the manufacturing process are indicated by the red squares. The results where the contact mechanism geometry is not constrained by the manufacturing process are indicated by the blue diamonds. For the constrained contact mechanism width designs the optimum cell wall angle is always approximately 80°, as shown in Figure 3.11. The optimal *h/l* does not change much until larger velocities, where is tends to increase rapidly, as shown in Figure 3.12. The optimal contact gap varies greatly with an increase in velocity, shown in Figure 3.13. Figure 3.14 shows that as the velocity increases, the maximum stress in the cell also increases. The objective function values can be seen in Figure 3.15. Table 3.5 shows how the optimal cell geometry changes as the input velocity increases. The cells here are wide and short due to the constraint on the contact mechanism width.

For the unconstrained contact mechanism width designs, the results show that as the input velocity increases, the angle, θ, decreases as shown in Figure 3.11. The optimal *h/l* does not change much as shown in Figure 3.12. The optimal contact gap varies greatly with an increase in velocity, shown in Figure 3.13. Most of the optimum contact gaps are found to be between 0.08 and 0.11 mm. When the contact gap increases, so does the maximum stress in the cell, while the smaller contact gaps limit the maximum stress in the cell. For the

larger input velocities, the maximum stress is closer to the limit no matter what the contact gap is as shown in Figure 3.14. The objective function values can be seen in Figure 3.15. Table 3.6 shows how the optimal cell geometry changes as the input velocity increases. As the stress in the cell increases with increasing input velocity, the cell transitions from a diamond shape to a honeycomb shape. The transition to a honeycomb shape is achieved by an increasing *h/l* and decreasing θ and a large variation in the contact gap, γ.

The comparison of the straight-walled three-variable results is important. For most input velocities, the maximum stress if very similar. As shown in the two-variable problem, the constrained contact mechanism width designs have a lower *E/(H*L)* compared to the unconstrained contact mechanism width designs as shown in Figure 3.15. Again, this is a result of the constraint on the width of the contact mechanism. The designs that are unconstrained by the manufacturing process always have a contact mechanism that is always 30% of *h*, whereas the designs that are constrained by the contact mechanism have a contact mechanism that ranges between 43% and 93% of *h*.

There is benefit found by employing γ as a variable. For some input velocities, the addition of γ does nothing. For the straight-walled cells where w_{cm} is constrained by the manufacturing process, at input velocities of 0.025 mm/s and 0.15 mm/s the objective function is very similar. For other input velocities, such as 0.0125 mm/s the difference is very large. For the three-variable design, the objective function is 0.14216 J/mm^2; whereas for the two-variable design, the objective function is 0.07669 J/mm^2. Now looking at the results that where the contact mechanism is not constrained by the manufacturing process, the addition of the γ again provides benefit to some input velocities and not others. For input velocities of 0.05 mm/s and 0.1375 mm/s the objective function is similar. However, a much larger improvement can be seen at an input velocity of 0.15 mm/s where for the three-variable design, the objective function has a value of 0.27363 J/mm^2 and for the two-variable design, the objective function has a value of 0.02176 J/mm^2. The addition of γ as a variable can improve the objective function.

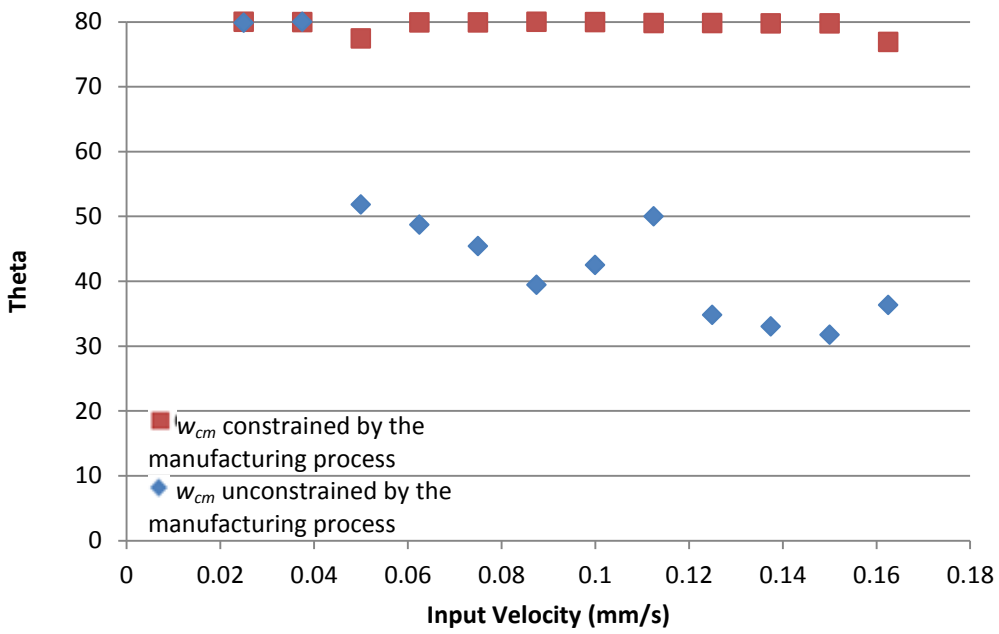

Figure 3.11: Comparison of θ for the Straight-walled Three-variable Optimization as Input Velocity Increases

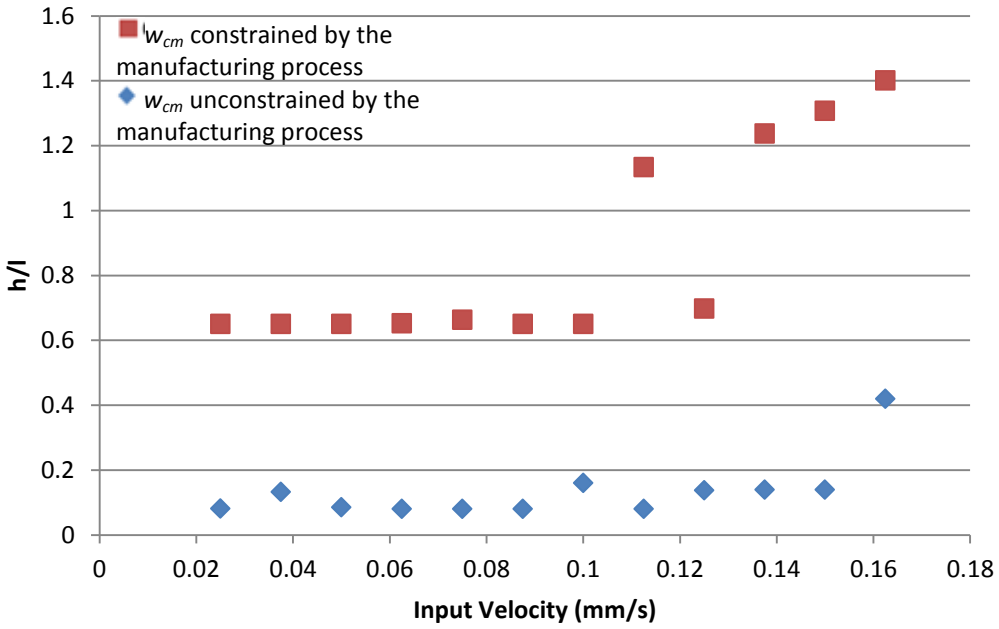

Figure 3.12: Comparison of *h/l* for the Straight-walled Three-variable Optimization as Input Velocity Increases

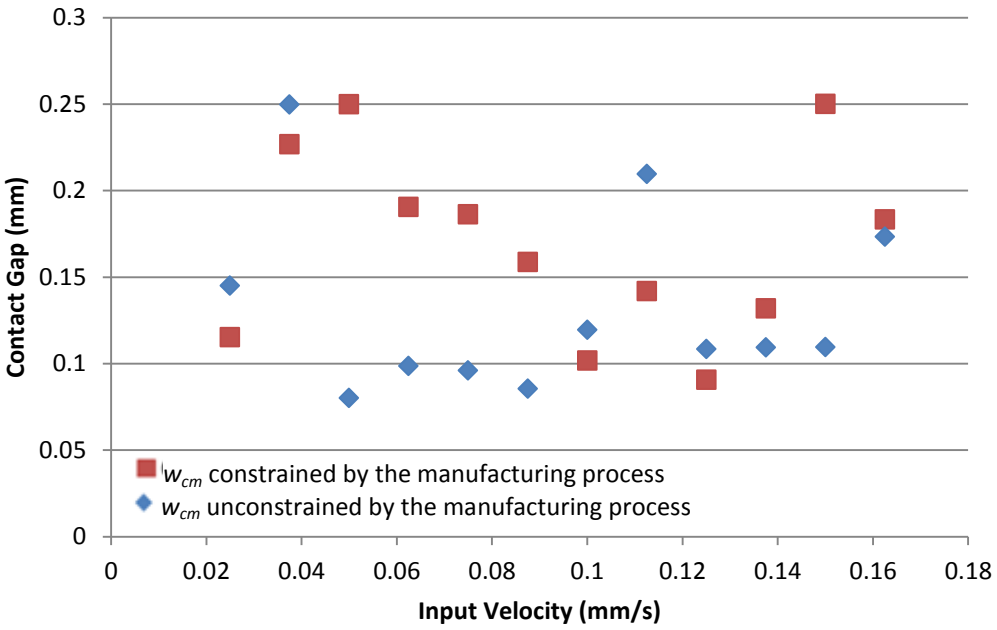

Figure 3.13: Comparison of γ for the Straight-walled Three-variable Optimization as Input Velocity Increases

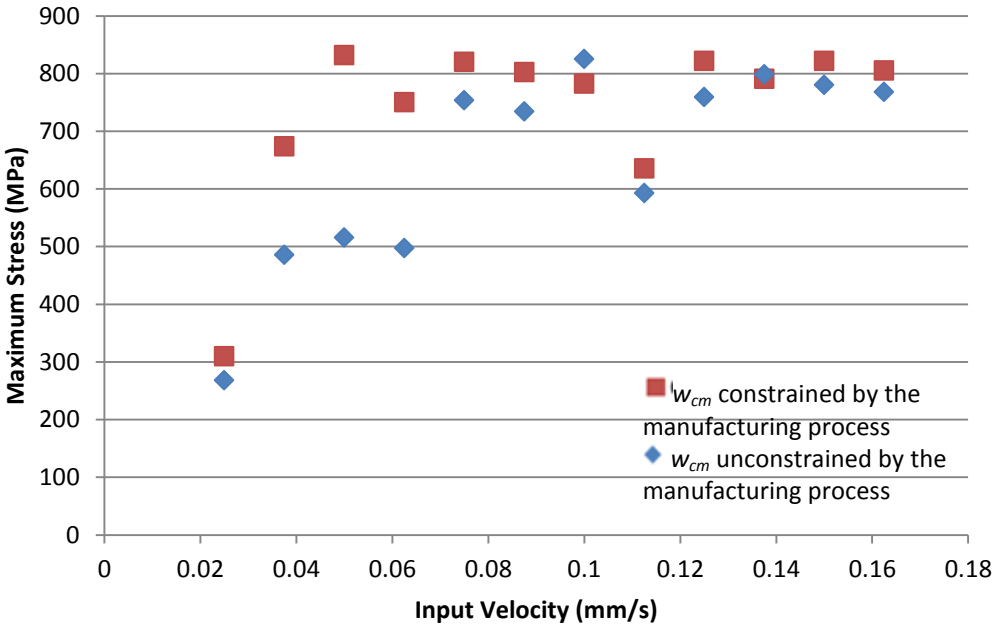

Figure 3.14: Comparison of the Maximum Stress for the Straight-walled Two-variable Optimization as Input Velocity Increases Shows the Maximum Stress is Similar at Most Input Velocities

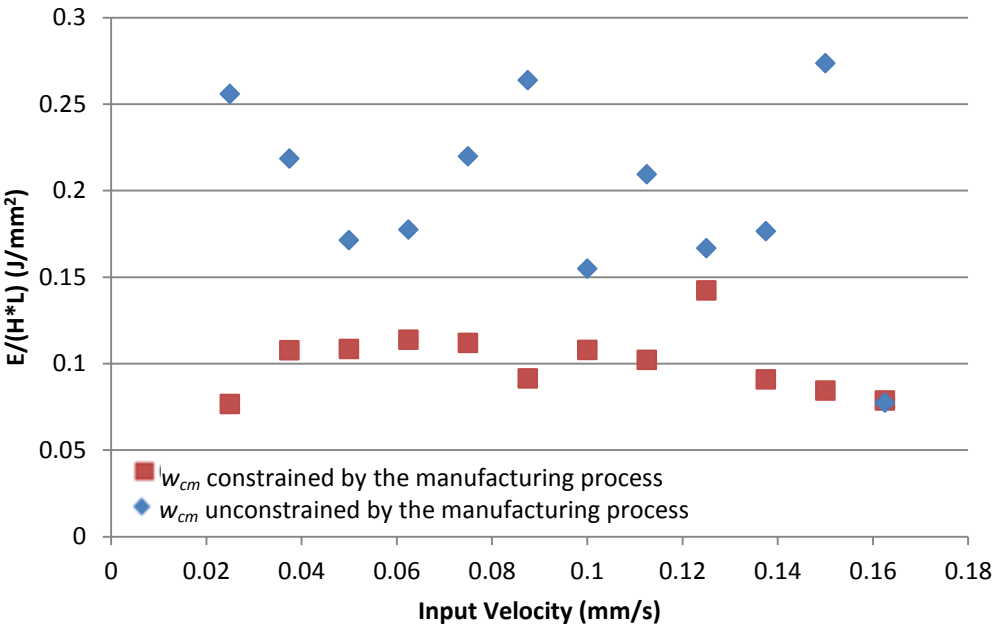

Figure 3.15: Comparison of *E/(H*L)* for the Straight-walled Two-variable Optimization as Input Velocity Increases Shows that the Constrained Cells have a Lower Value

Table 3.5: Cell Geometry is Diamond Shaped and *h* Varies for Straight-walled Three-variable Optimization Constrained by the Manufacturing Process

Input Velocity (mm/s)	Cell Shape –––––– 4mm
0.025 – 0.1, 0.125	
0.1125	
0.1375-0.1625	

Table 3.6: Cell Geometry Changes from a Diamond Shape to a More of a Traditional Honeycomb with Increasing Input Velocity for Straight-walled Three-variable Optimization Unconstrained by the Manufacturing Process

Input Velocity (mm/s)	Cell Shape -------- 4mm	Input Velocity (mm/s)	Cell Shape -------- 4mm
0.025	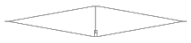	0.1	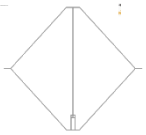
0.0375		0.1125	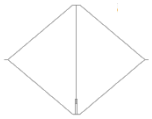
0.05	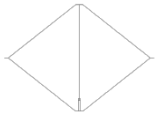	0.125	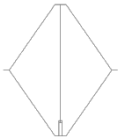
0.0625	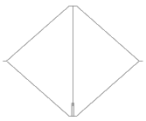	0.1375	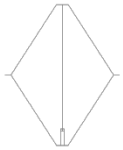
0.075	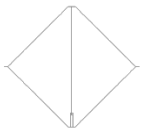	0.15	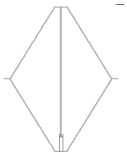
0.0875	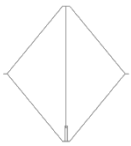	0.1625	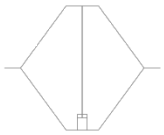

3.2.3 Curved-walled Two-variable

As discussed in Section 1.3.2, curved-walled cells are easier to manufacture using the LM-RIF process; therefore, two different problems were considered for the two-variable optimization problem. The first run was where the contact mechanism width was constrained by the manufacturing process, indicated by the red squares. The second run was completed where the contact mechanism width was not constrained, indicated by the blue diamonds.

For the constrained contact mechanism width designs, the optimum cell wall angle is always approximately 80° as shown in Figure 3.16. As the input velocity increases, the optimal *h/l* changes very little, as shown in Figure 3.17. Figure 3.18 shows that the maximum stress is always close to the stress limit. The optimal objective function values can be seen in Figure 3.19. The optimal cell geometries as a function of input velocity can be seen in Table 3.7. The diamond shaped cells shown for the input velocities show almost no curvature in the walls. This is because *h* is so small and θ is so large. As *h* increases and θ decreases, the curvature increases. To understand how *h/l* and θ affect the radius of the fillet, a parameter variation study was performed. Figure 3.20 shows the resulting radius of the fillet for three different values of *h/l* as θ ranges from 10° to 80°. The figure illustrates how the shape of the cell changes as both *h/l* and θ change. It shows that when *h/l* is small, independent of θ, the radius of the fillet is very small. As *h/l* increase, θ has a larger effect on the resulting fillet.

For the unconstrained contact mechanism width designs, the optimum cell wall angle is decreases with increasing input velocity as shown in Figure 3.16. As the input velocity increases, the optimal *h/l* jumps between the two limits, as shown in Figure 3.17. Figure 3.18 shows that the maximum stress increases with an increase in input velocity. The optimal objective function values, which increase with an increase in input velocity, can be seen in Figure 3.19. The optimal cell geometries as a function of input velocity can be seen in Table 3.8. For the results presented thus far, this is the first time that the results do not show a gradual transition. The large changes in *h/l* cause this lack of a gradual transition.

The comparison of the curved-walled two-variable results is important. Figure 3.16 shows the comparison of θ between the results constrained by the manufacturing process, indicated by the red squares, and those not constrained by the manufacturing process, indicated by the blue diamonds. Figure 3.17 shows the comparison of *h/l* between the results constrained by the manufacturing process and those not constrained by the manufacturing process. Most of the results jump between the two bounds set for the optimization problem for the unconstrained problem and remain at the lower limit for the constrained problem. Figure 3.18 shows the comparison of the maximum stress for the two optimization problems. For most input velocities, the maximum stress is lower for the unconstrained cells. Because the cells are not at the stress limit set, the constrained contact mechanism

width designs have a higher *E/(H*L)* compared to the unconstrained contact mechanism width designs as shown in Figure 3.19. For the curved-walled problem, the constrained results have a better objective function.

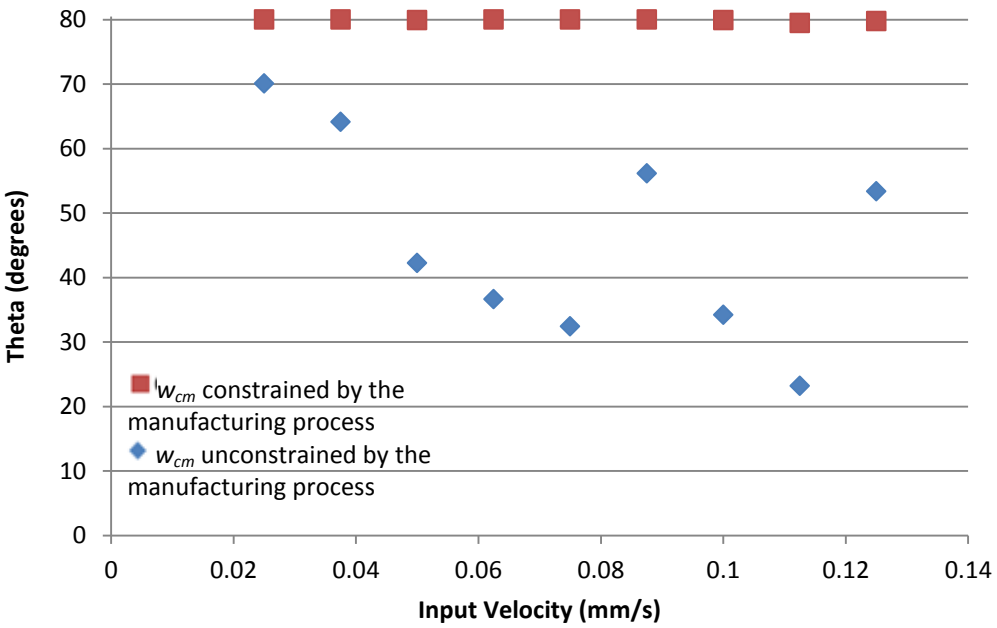

Figure 3.16: Comparison of θ for the Curved-walled Two-variable Optimization as Input Velocity Increases

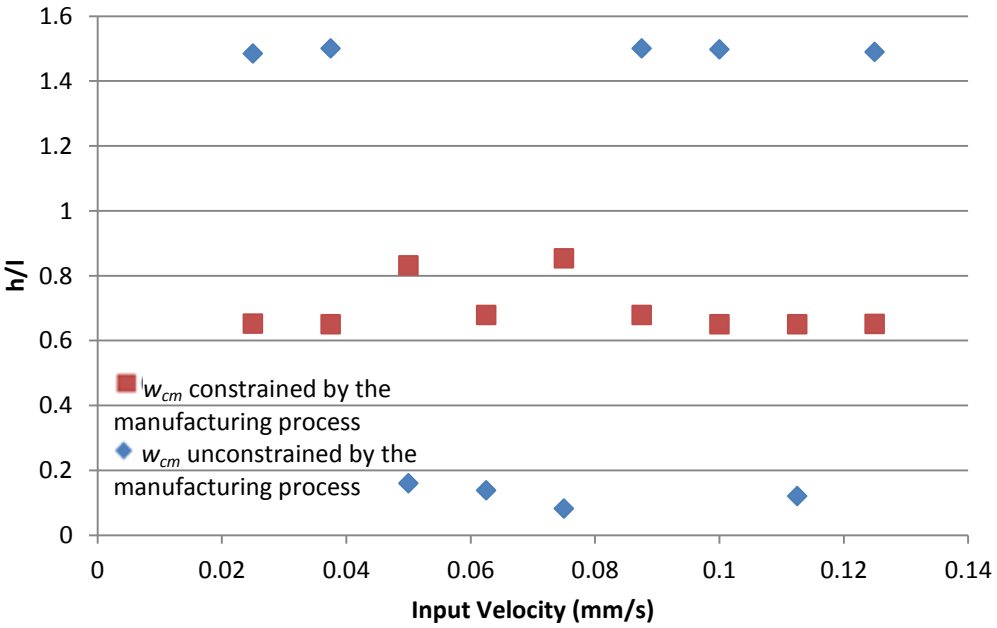

Figure 3.17: Comparison of *h/l* for the Curved-walled Two-variable Optimization as Input Velocity Increases

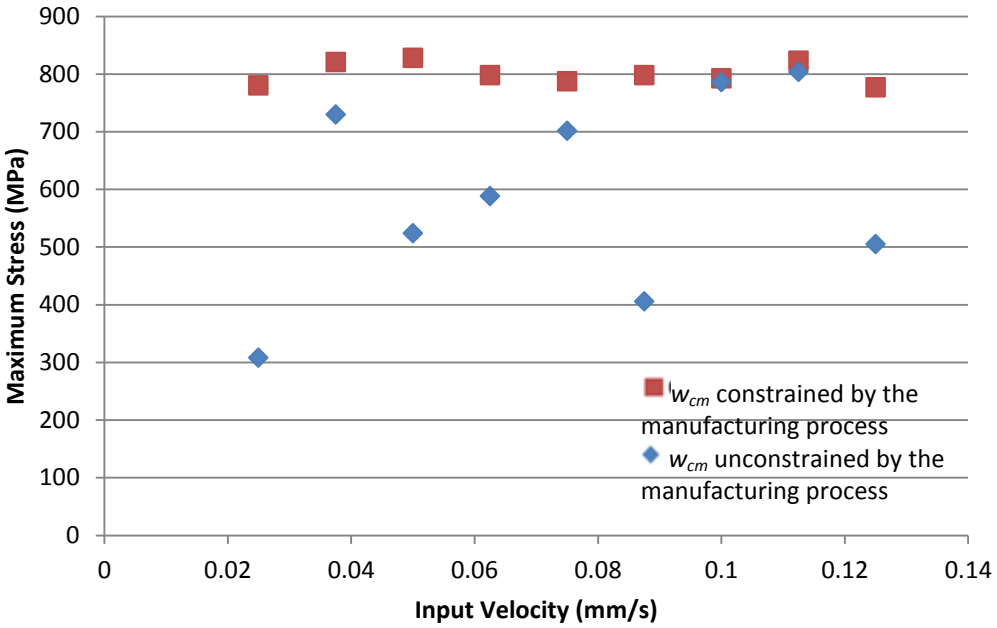

Figure 3.18: Comparison of the Maximum Stress for the Curved-walled Two-variable Optimization as Input Velocity Increases

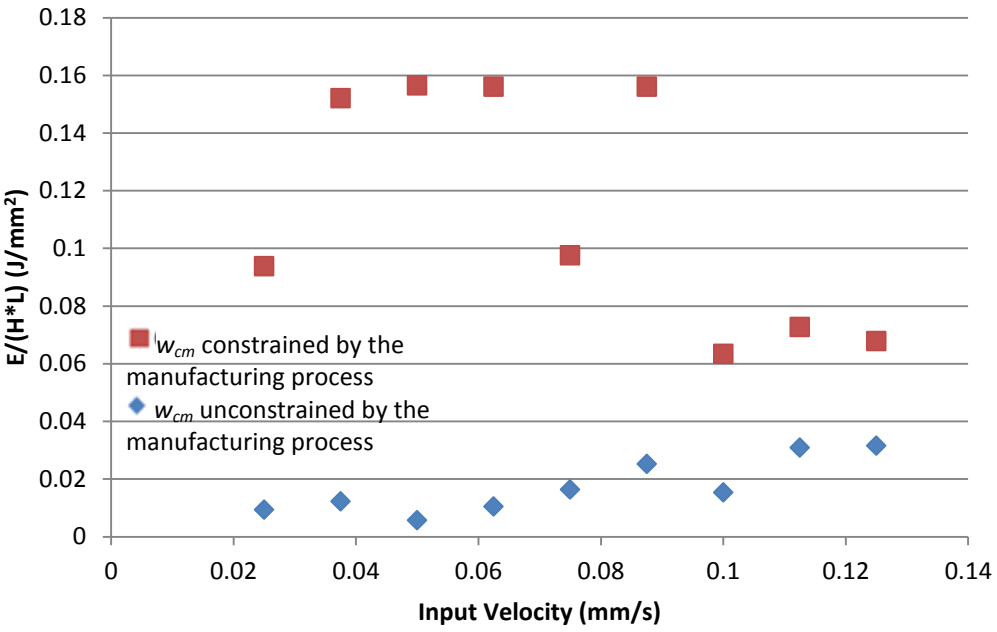

Figure 3.19: Comparison of *E/(H*L)* for the Curved-walled Two-variable Optimization as Input Velocity Increases

Table 3.7: Cell Geometry Barely Changes Shape with Increasing Input Velocity for Curved-walled Two-variable Optimization Constrained by the Manufacturing Process

Input Velocity (mm/s)	Cell Shape ——— 4mm	Input Velocity (mm/s)	Cell Shape ——— 4mm
0.025 – 0.0375, 0.0625, 0.0875-0.125		0.05, 0.075	

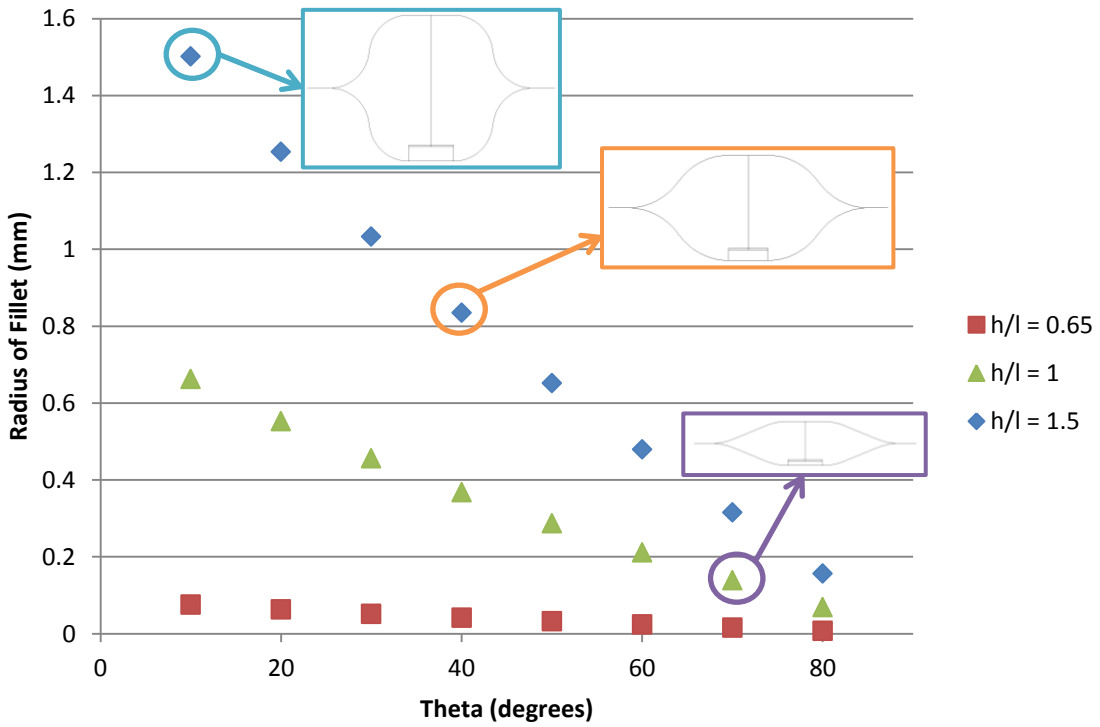

Figure 3.20: Radii of Different Fillets for Varying *h/l* and θ Values Shows that with Increasing *h/l* and Decreasing θ the Radius Increases

Table 3.8: Cell Geometry Varies in Shape with Increasing Input Velocity for Curved-walled Two-variable Optimization Unconstrained by the Manufacturing Process

Input Velocity (mm/s)	Cell Shape –––––– 4mm
0.025	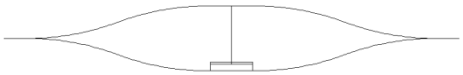
0.0375	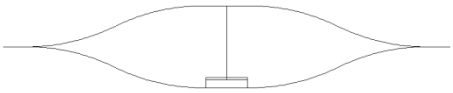
0.05	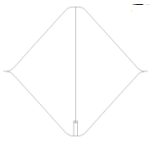
0.0625	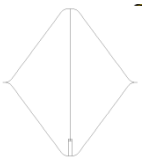
0.075	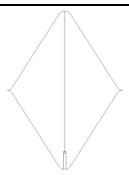
0.0875	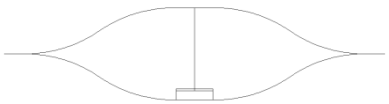
0.1	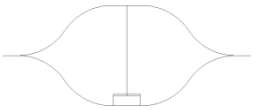
0.1125	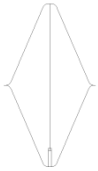
0.125	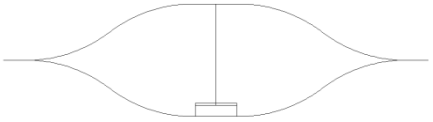

3.2.4 Curved-walled Three-variable

For the curved-walled cell, a parameter variation study was performed to see if the addition of the contact gap was beneficial. The cells that were analyzed were cells that look similar to the cell outlined in orange in Figure 3.20. This provided a radius in the middle of the range of possible radii for this particular cell. The angle was either 40° or 50° and h/l was either 0.9 or 1.0. The cells had an input velocity of 0.075 mm/s over a time of two seconds. The contact gap was varied between 0.08 mm and 0.25 mm. Figure 3.22 shows that for the same angle, θ, a smaller h/l is only slightly more beneficial. However, Figure 3.21 shows that for the same h/l, a larger angle, θ, is more beneficial. For the cells analyzed, contact only occurred in the smaller contact gaps as shown in both figures by the filled in shapes. The open shapes indicate that contact does not occur. The reason that contact does not occur is that the cell did not deform enough due to the prescribed input for contact to occur. If the input velocity were larger, contact would eventually occur assuming that the stress limit is not reached beforehand. The results do show that the sooner contact occurs, which is achieved through a smaller contact gap, the higher the objective function. Also, if contact does not occur, the objective function is unchanged independent of the magnitude of the contact gap.

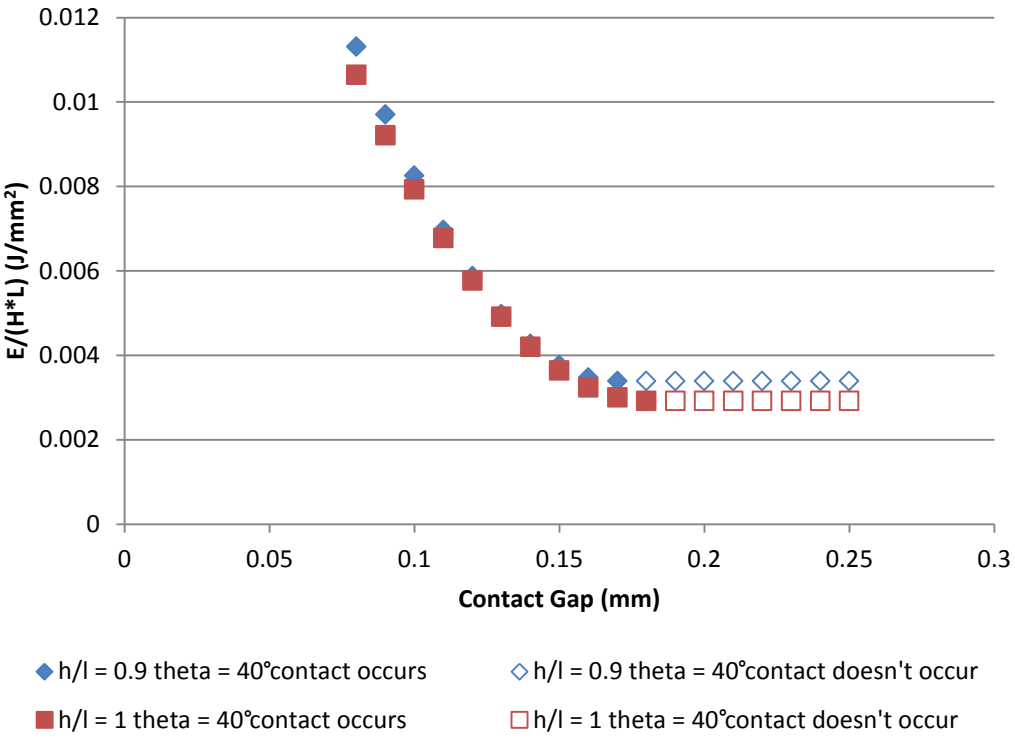

Figure 3.21: *E/(H*L)* Decreases with Increasing Contact Gap for a Constant θ of 40°

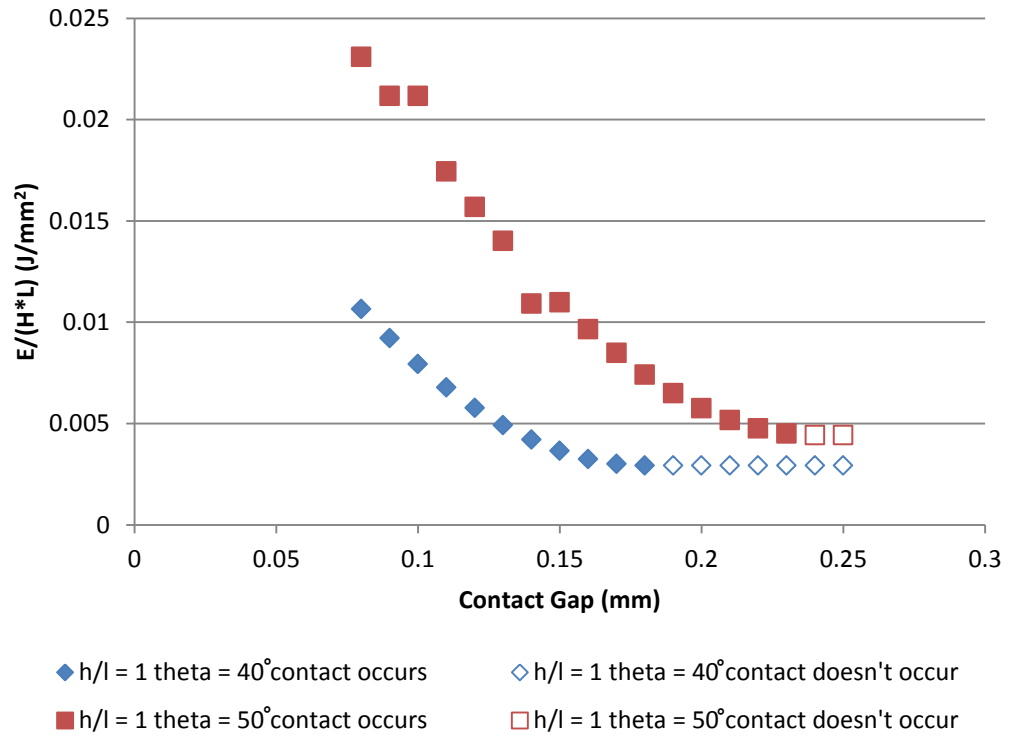

Figure 3.22: *E/(H*L)* Decreases with Increasing Contact Gap for a Constant *h/l* of 1.0

For the constrained contact mechanism width designs, the optimum cell wall decreases with an increase in input velocity as shown in Figure 3.23. As the input velocity increases, the optimal *h/l* also increases, as shown in Figure 3.24. Figure 3.25 indicates that with increasing input velocity, the contact gap also increases. Figure 3.26 shows that the maximum stress is always close to the stress limit. The optimal objective function values can be seen in Figure 3.27. The optimal cell geometries as a function of input velocity can be seen in Table 3.9. The diamond shaped cells shown for input velocities of 0.025, 0.0375, 0.0875 mm/s show almost no curvature in the walls. This is because *h* is so small and θ is so large.

The optimization algorithm was also run for the unconstrained case. Figure 3.23 shows that the optimum θ changes with increasing input velocity. The optimum *h/l* increases with increasing input velocity as shown in Figure 3.24. The optimum contact gap, γ, decreases with increasing input velocity shown in Figure 3.25. Figure 3.26 shows that the maximum stress remains close to the stress limit for most cells. Figure 3.27 shows that the optimum *E/(H*L)* mirrors the maximum stress in the cell. The optimal cell geometries as a function of input velocity can be seen in Table 3.10.

The comparison of the curved-walled three-variable results is also important. Figure 3.23 shows the comparison of θ between the results constrained by the manufacturing process, indicated by the red squares, and those not constrained by the manufacturing process, indicated by the blue diamonds. The overall trend is that with increasing input velocity, the value of θ decreases. Figure 3.24 shows the comparison of *h/l* between the results constrained by the manufacturing process and those not constrained by the manufacturing process. The results for the unconstrained cells jump between the two bounds set for the optimization problem and are spread out between bounds for the designs constrained by the manufacturing. Figure 3.25 shows the comparison of γ. The optimum contact gap is lower for the constrained contact mechanism width because of the amount of material. The unconstrained contact mechanism width has much less material and therefore a larger contact gap is needed. Figure 3.26 shows the comparison of the maximum stress for the two optimization problems. For the larger input velocities, the maximum stress is lower for the unconstrained cells. The constrained width designs have a maximum stress that is much closer to the stress limit. The constrained contact mechanism width designs have a

higher *E/(H*L)* compared to the unconstrained contact mechanism width designs for most input velocities as shown in Figure 3.27. When compared to the two-variable results, the addition of the contact gap allows the objective function to become more similar for the three-variable results and at a few of the input velocities, the cells are very similar.

There is benefit found by employing γ as a variable. For some input velocities, the addition of γ does nothing. For the curved-walled cells where w_{cm} is constrained by the manufacturing process, at input velocities of 0.025 mm/s, 0.0375mm/s, and 0.05 mm/s the objective function is very similar. For other input velocities, such as 0.01 mm/s there is more of a difference. For the three-variable design, the objective function is 0.07120 J/mm^2; whereas for the two-variable design, the objective function is 0.06332 J/mm^2. Although the difference is small, there is still an improvement seen through the addition of γ. Now looking at the results that where the contact mechanism is not constrained by the manufacturing process, the addition of the γ provides a benefit to almost all input velocities. For an input velocity of 0.1125 mm/s the objective function is similar. For all other input velocities, the addition of γ as a variable causes improvement. For example, at an input velocity of 0.025 mm/s, the three- variable design has an objective function with a value of 0.06823 J/mm^2 and the two-variable design has objective function with a value of 0.00937 J/mm^2. At the other end, with an input velocity of 0.125 mm/s, the three- variable design has an objective function with a value of 0.08721 J/mm^2 and the two-variable design has objective function with a value of 0.03151 J/mm^2. The addition of γ as a variable can improve the objective function.

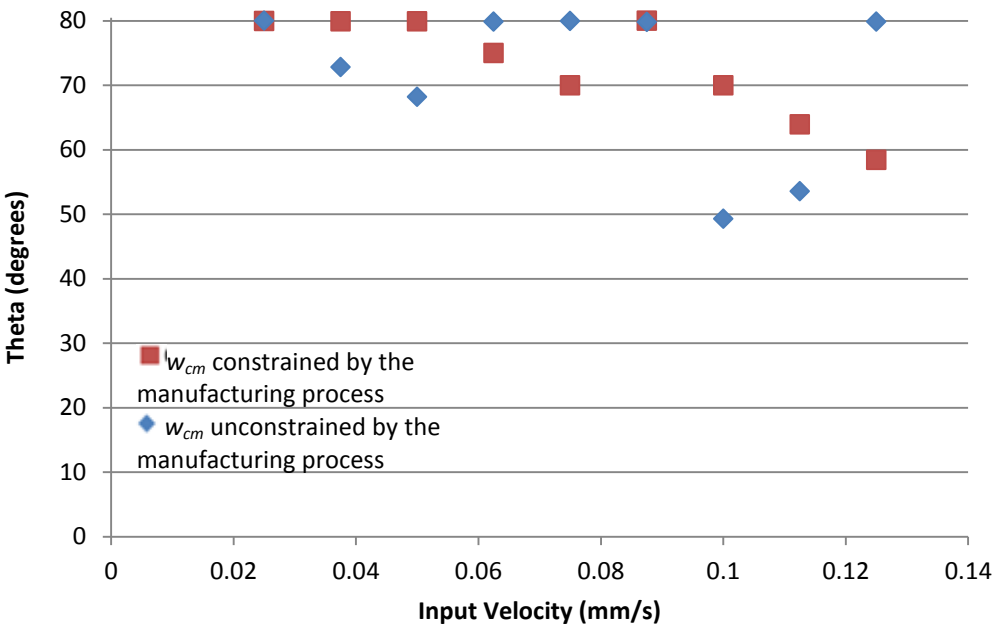

Figure 3.23: Comparison of θ for the Curved-walled Three-variable Optimization as Input Velocity Increases

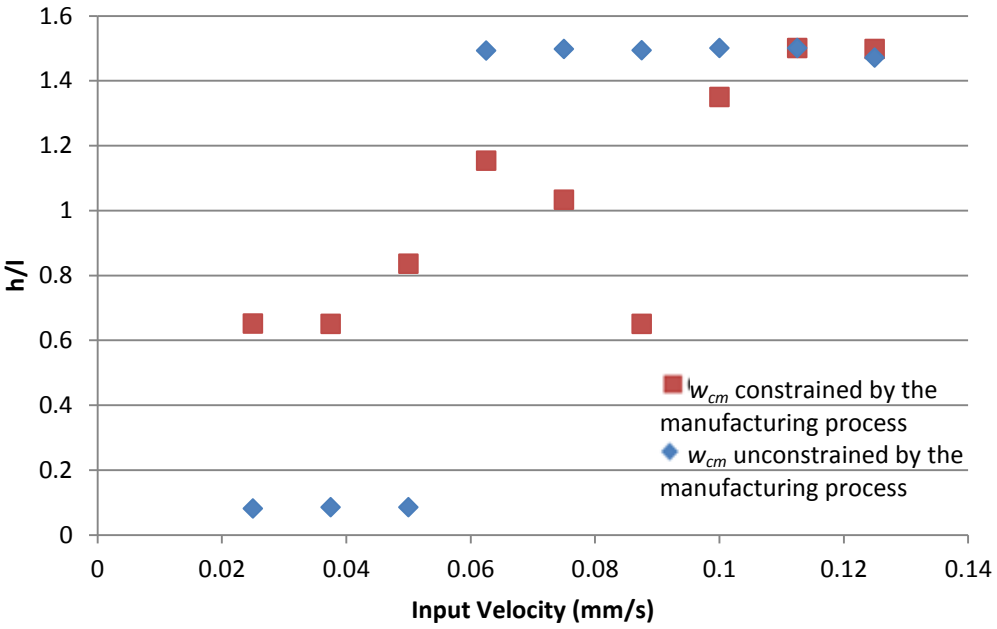

Figure 3.24: Comparison of *h/l* for the Curved-walled Three-variable Optimization as Input Velocity Increases

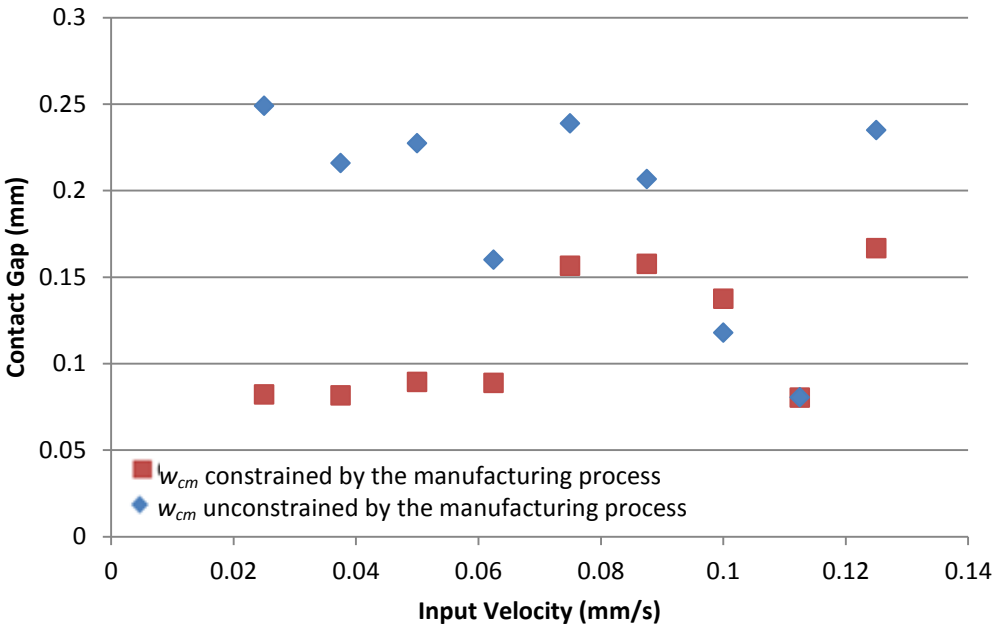

Figure 3.25: Comparison of γ for the Curved-walled Three-variable Optimization as Input Velocity Increases

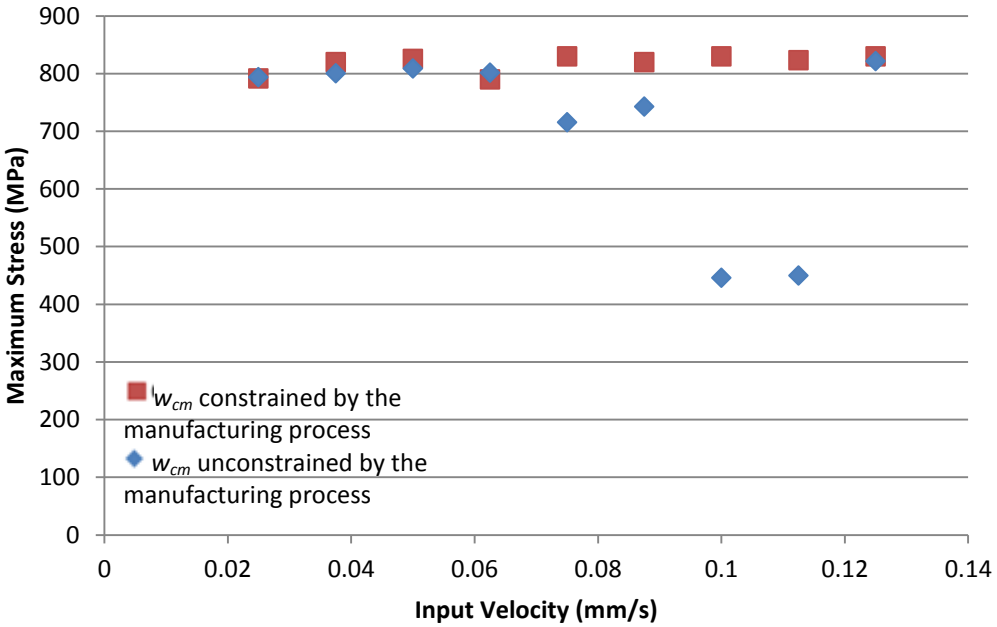

Figure 3.26: Comparison of the Maximum Stress for the Curved-walled Three-variable Optimization as Input Velocity Increases

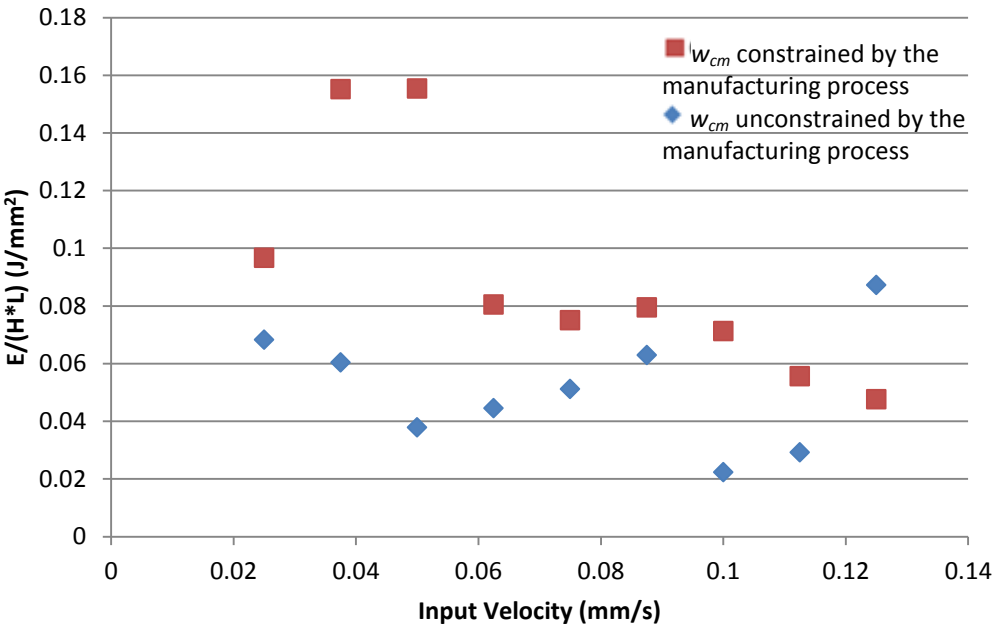

Figure 3.27: Comparison of *E/(H*L)* for the Curved-walled Three-variable Optimization as Input Velocity Increases

Table 3.9: Cell Geometry Changes from a Diamond Shape to a Curved Honeycomb Design with Increasing Input Velocity for Curved-walled Three-variable Optimization Constrained by the Manufacturing Process

Input Velocity (mm/s)	Cell Shape -------- 4mm	Input Velocity (mm/s)	Cell Shape -------- 4mm
0.025		0.0875	
0.0375		0.1	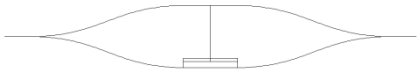
0.05		0.1125	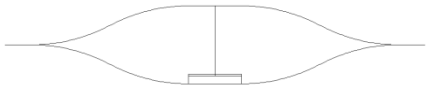
0.0625	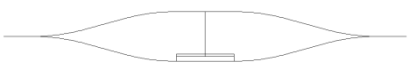	0.125	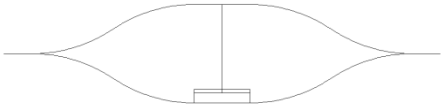
0.075	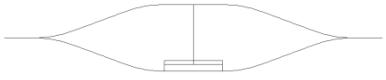		

Table 3.10: Cell Geometry Changes from a Diamond Shape to a More of a Traditional Honeycomb with Increasing Input Velocity for Curved-walled Three-variable Optimization Unconstrained by the Manufacturing Process

Input Velocity (mm/s)	Cell Shape -------- 4mm	Input Velocity (mm/s)	Cell Shape -------- 4mm
0.025	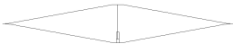	0.0875	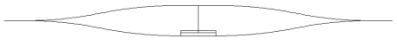
0.0375	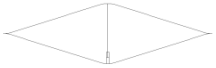	0.1	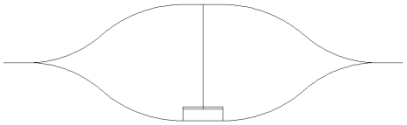
0.05		0.1125	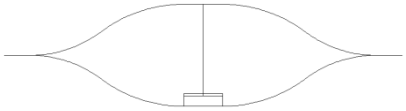
0.0625	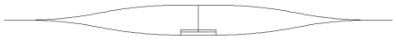	0.125	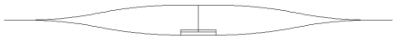
0.075			

3.3 Straight-walled Versus Curved-walled Results

The comparison of the straight-walled cells versus the curved-walled cells is important because it determines which cell is the best to manufacture. For all figures in Section 3.3, the results for the straight-walled cells are indicated by the red squares. The results for the curved-walled cells are indicated by the blue diamonds. Each point on the plot represents the optimal design for that particular input velocity.

3.3.1 Two-variable Constrained by the Manufacturing Process

There is no difference in the optimum cell angle for the straight- and curved-walled cells as shown in Figure 3.28. For the curved-walled cells, the optimum *h/l* is always closer to the lower limit whereas the straight-walled cells approach the upper limit as shown in Figure 3.29. Figure 3.30 shows that the maximum stress in the cell is closer to the stress

limit for the curved-walled cells. At the lower input velocities, the curved-walled cells have a better objective function but, as the input velocity increases, the straight-wall cells have a better objective function as shown in Figure 3.31. When looking at the input velocity of 0.125 mm/s, the both cells have the same value of θ but the values of *h/l* are very different. Even though the *h/l* values are different, the objective function is similar. The straight-walled cell can absorb more energy, *E*, but the value for *(H*L)*, is also higher. The increase in both values results in a similar objective function. Both cells also have similar maximum stress values. Because the objective function is *E/(H*L)*, as *E* increases so does *(H*L)* thus, the change in *h/l* does not have a large affect on the objective function.

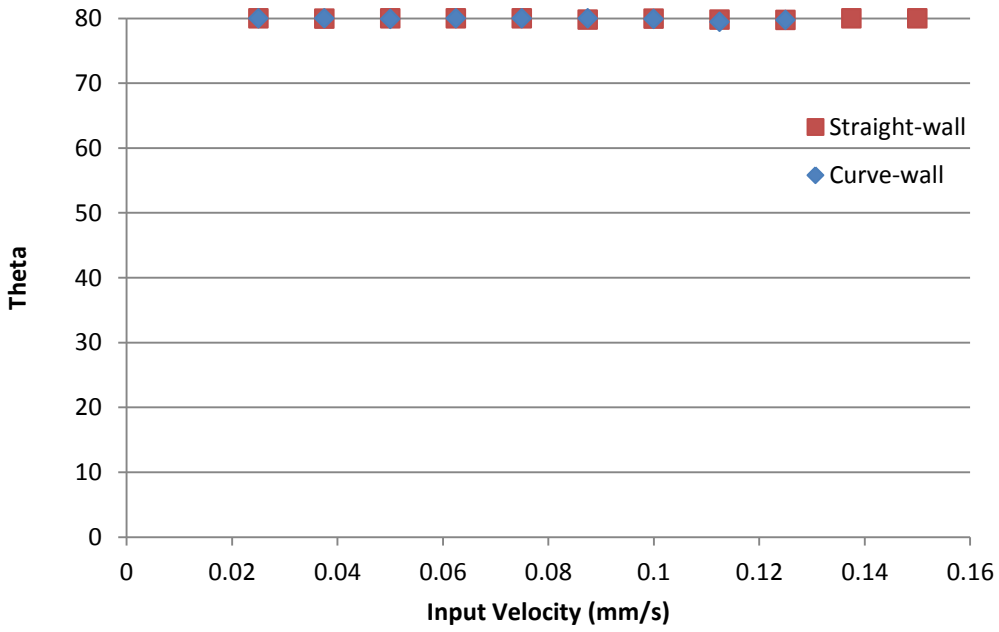

Figure 3.28: Comparison of θ for the Two-variable Optimization Constrained by the Manufacturing Process as Input Velocity Increases

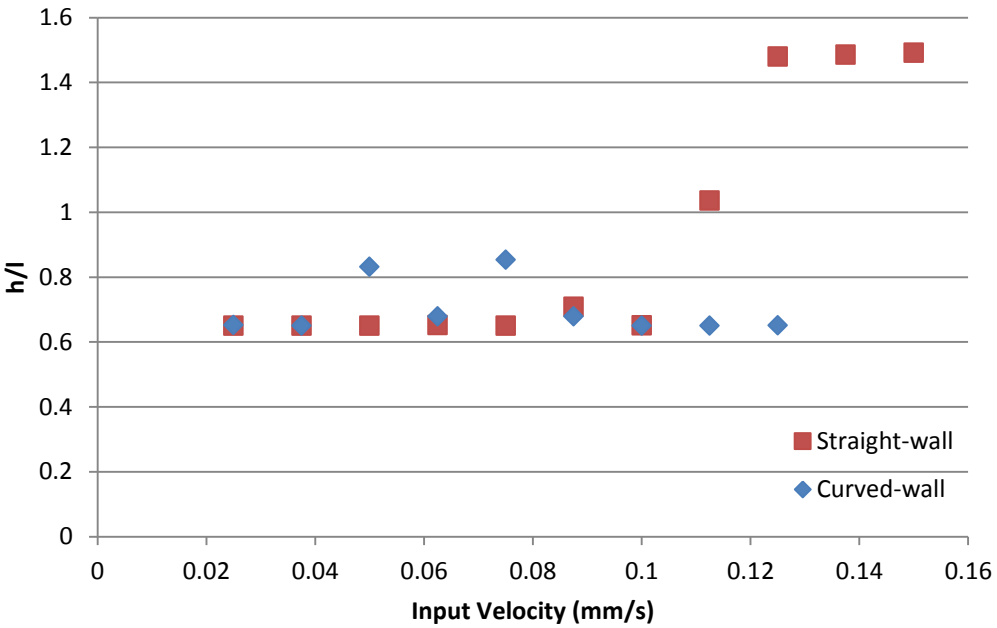

Figure 3.29: Comparison of *h/l* for the Two-variable Optimization Constrained by the Manufacturing Process as Input Velocity Increases

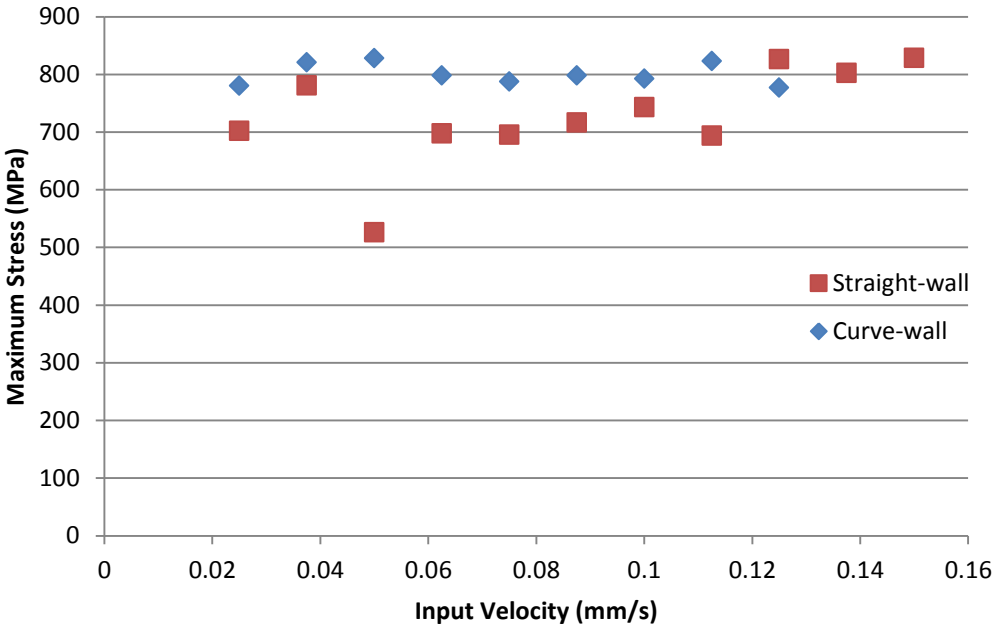

Figure 3.30: Comparison of the Maximum Stress for the Two-variable Optimization Constrained by the Manufacturing Process as Input Velocity Increases

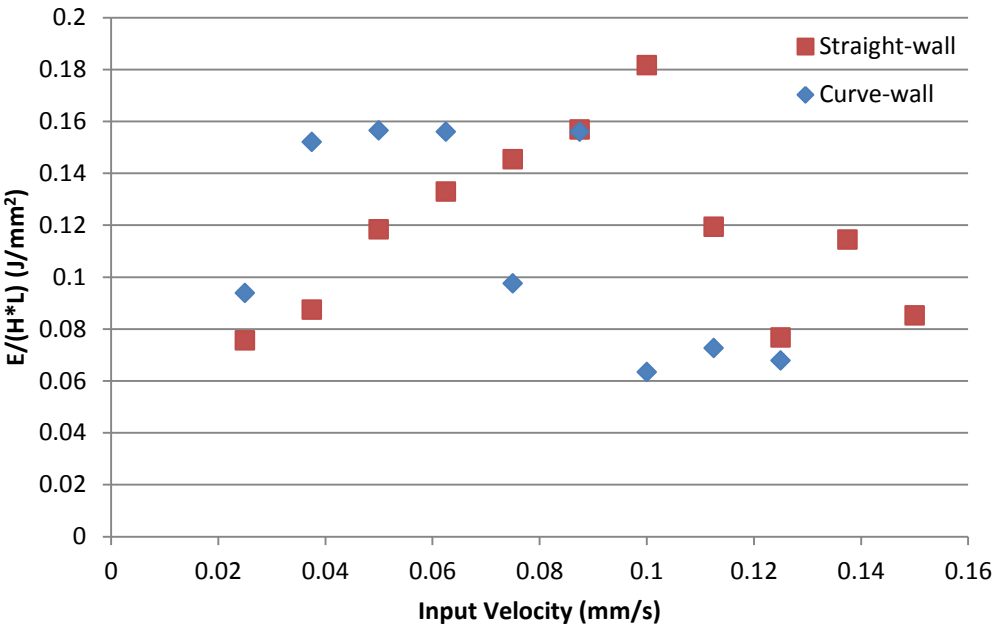

Figure 3.31: Comparison of *E/(H*L)* for the Two-variable Optimization Constrained by the Manufacturing Process as Input Velocity Increases

3.3.2 Two-variable Unconstrained by the Manufacturing Process

The comparison of the straight-walled cells versus the curved-walled cells is important because it determines which cell would be the best to manufacture through the use of a different manufacturing process. The optimum cell angle θ decreases for both the straight- and curved-walled cells as shown in Figure 3.32. For the curved-walled cells, the optimum *h/l* varies between the bounds whereas the straight-walled cells, the optimum *h/l* increases with an increase in input velocity shown in Figure 3.33. Figure 3.34 shows that the maximum stress in the cell increases with increasing input velocity for the straight-walled cells and varies greatly for the curved-walled cells. For all input velocities, the straight-walled cells have a better objective function by approximately a minimum factor of ten shown in Figure 3.35. This large discrepancy in the objective function is a result of a lower *E* and a much higher *(H*L)*. The values of *(H*L)* for the straight-walled cells are always lower when compared to those for the curved-walled cells.

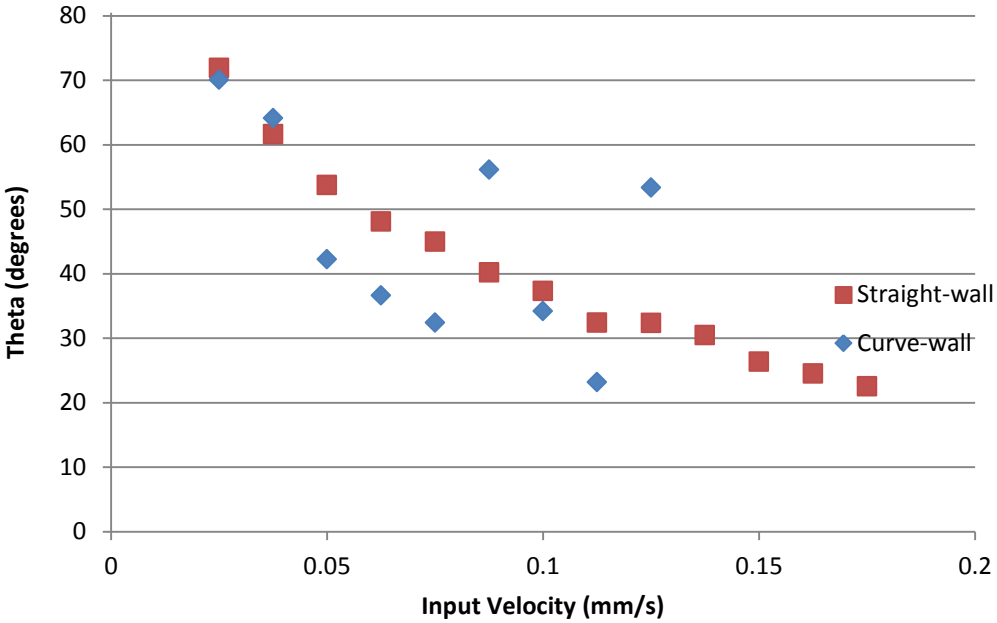

Figure 3.32: Comparison of θ for the Two-variable Optimization Unconstrained by the Manufacturing Process as Input Velocity Increases

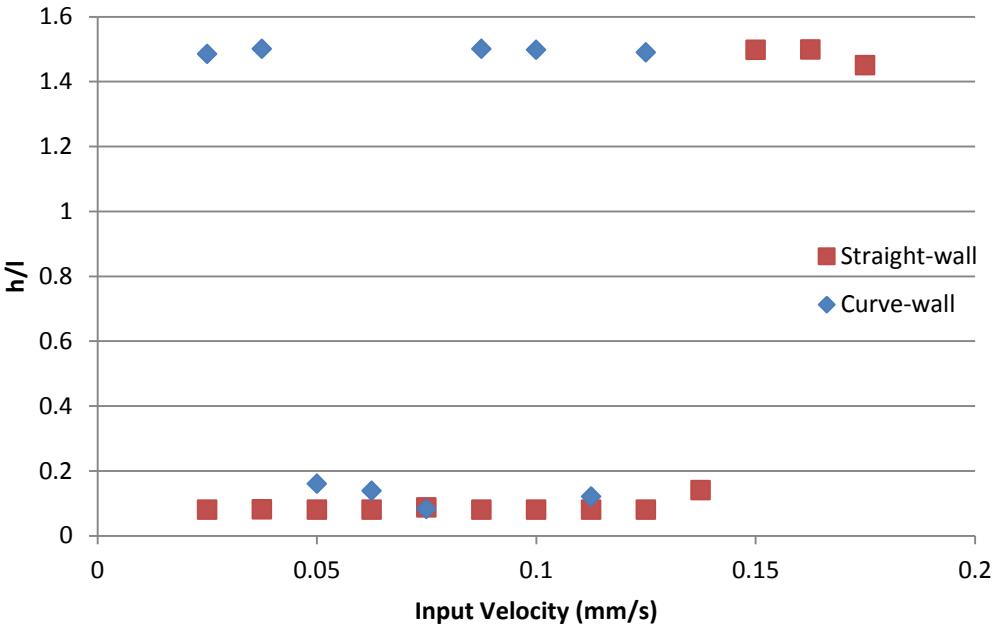

Figure 3.33: Comparison of *h/l* for the Two-variable Optimization Unconstrained by the Manufacturing Process as Input Velocity Increases

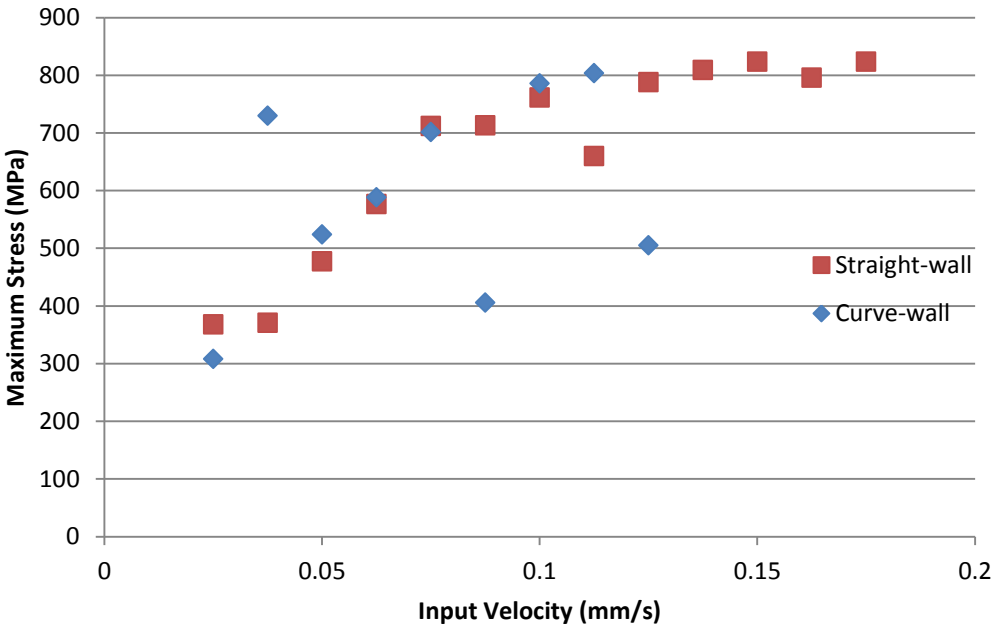

Figure 3.34: Comparison of the Maximum Stress for the Two-variable Optimization Unconstrained by the Manufacturing Process as Input Velocity Increases

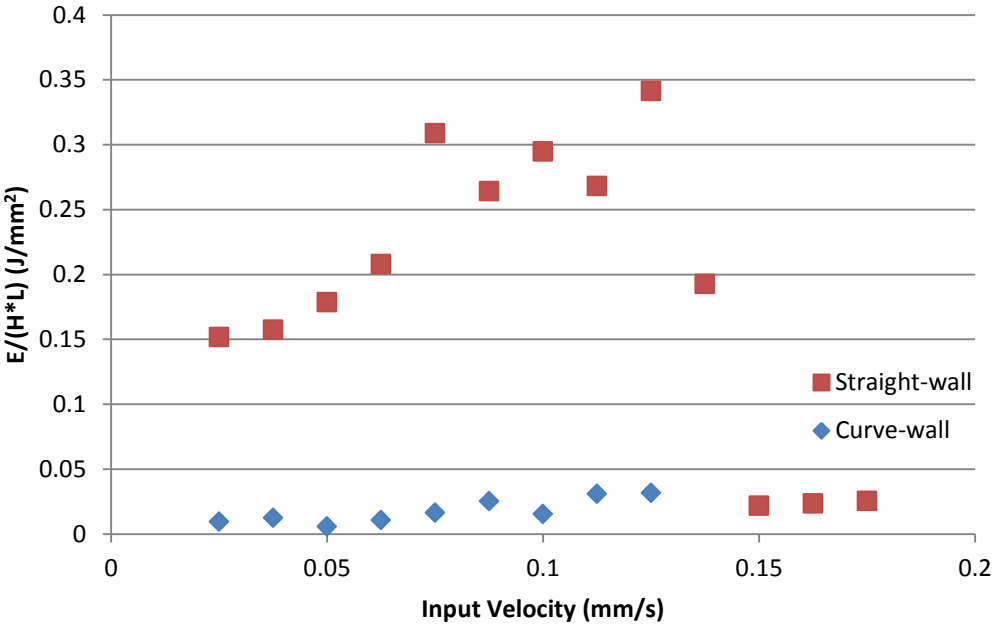

Figure 3.35: Comparison of *E/(H*L)* for the Two-variable Optimization Unconstrained by the Manufacturing Process as Input Velocity Increases

3.3.3 Three-variable Constrained by the Manufacturing Process

The comparison of the straight-walled cells versus the curved-walled cells is important because it determines which cell is the best to manufacture. The optimum cell angle decreases slightly for both the straight- and curved-walled cells as shown in Figure 3.36. For both cells, the optimum *h/l* increases with an increase in input velocity shown in Figure 3.37. Figure 3.38 shows the optimum contact gap for each cell. For the smaller input velocities and the curved-walled cells, the contact gap is at the lower limit as expected from the results shown in Figures 3.34 and 3.35. As the input velocity increases, the contact gap varies. Figure 3.39 shows that the maximum stress in the cell increases with increasing input velocity for the straight-walled cells and remains close to the stress limit for the curved-walled cells. As shown for the two-variable problem, at the lower input velocities, the curved-walled cells have a better objective function but, as the input velocity increase, the straight-wall cells have a better function as shown in Figure 3.40. For all cells, the curved-walled cells have a higher *E* but as the input velocity increases, so does *(H*L)*. There is a larger increase in *(H*L)* for the curved-walled cells. The transition from the curved-walled cells to the straight-walled cells being optimum occurs when the values of *(H*L)* diverge.

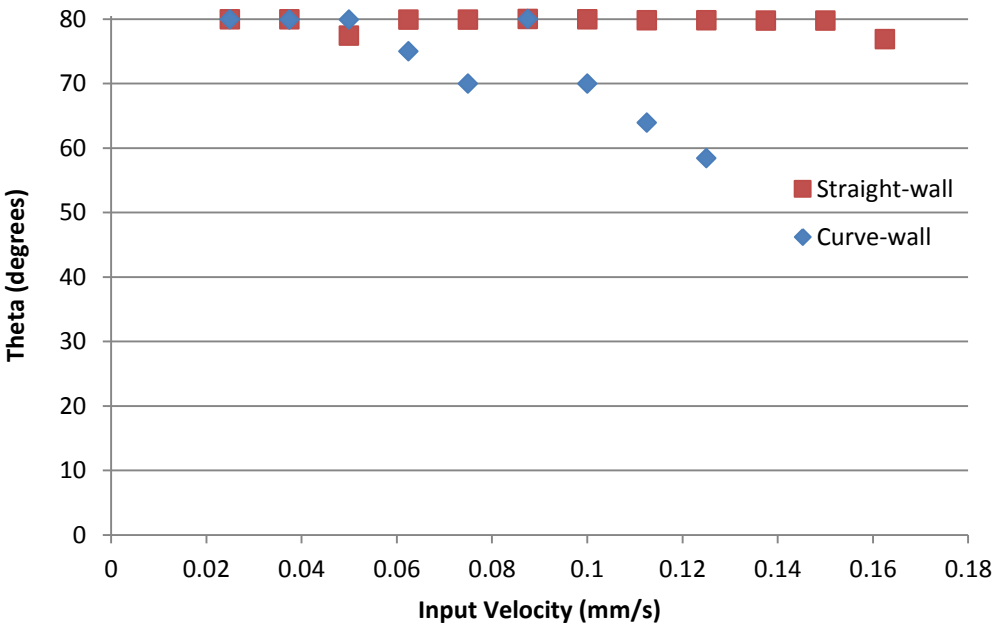

Figure 3.36: Comparison of θ for the Three-variable Optimization Constrained by the Manufacturing Process as Input Velocity Increases

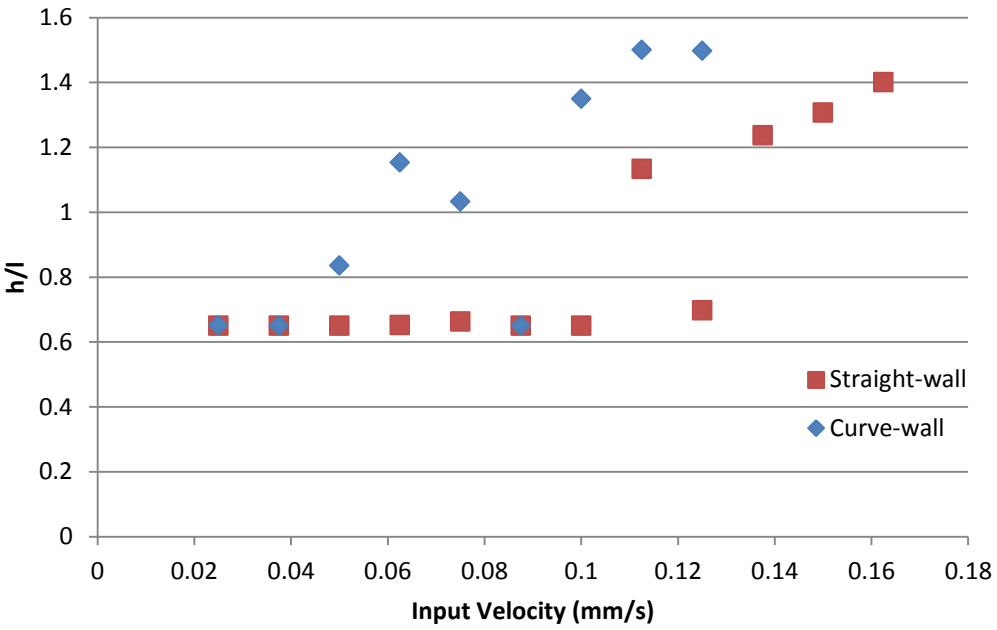

Figure 3.37: Comparison of *h/l* for the Three-variable Optimization Constrained by the Manufacturing Process as Input Velocity Increases

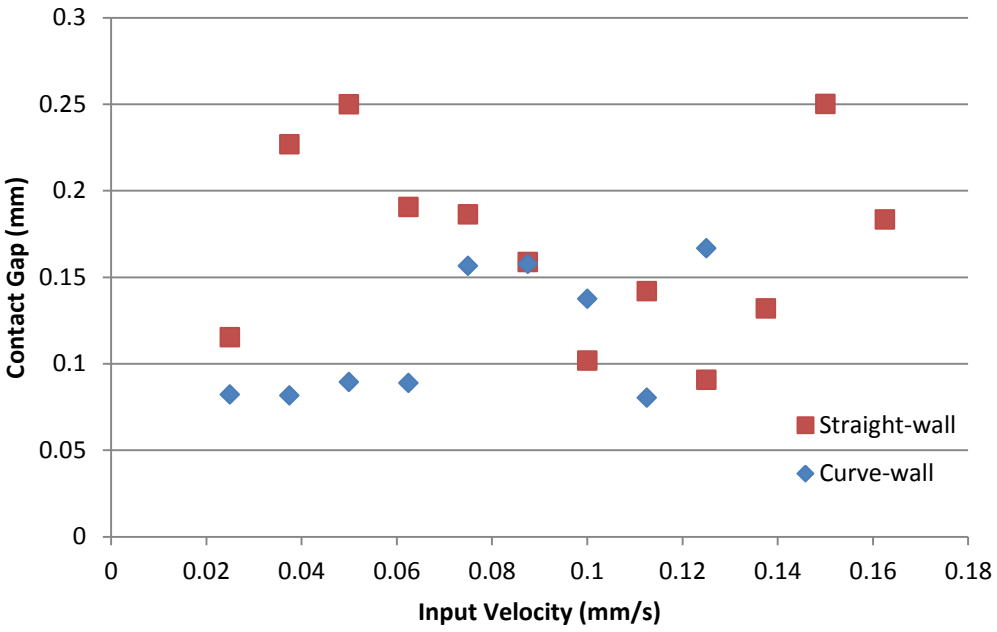

Figure 3.38: Comparison of γ for the Three-variable Optimization Constrained by the Manufacturing Process as Input Velocity Increases

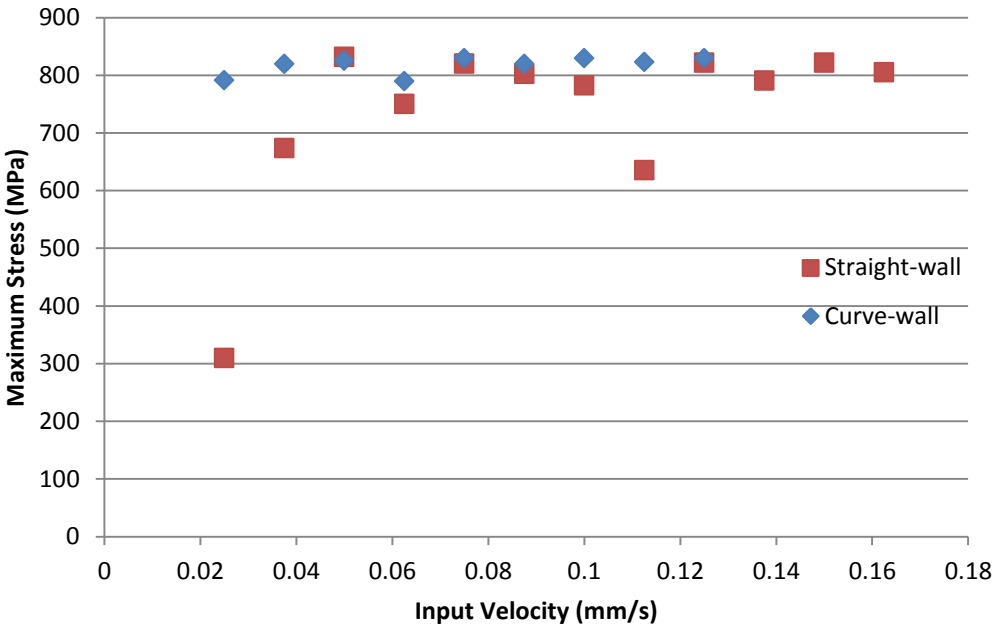

Figure 3.39: Comparison of the Maximum Stress for the Three-variable Optimization Constrained by the Manufacturing Process as Input Velocity Increases

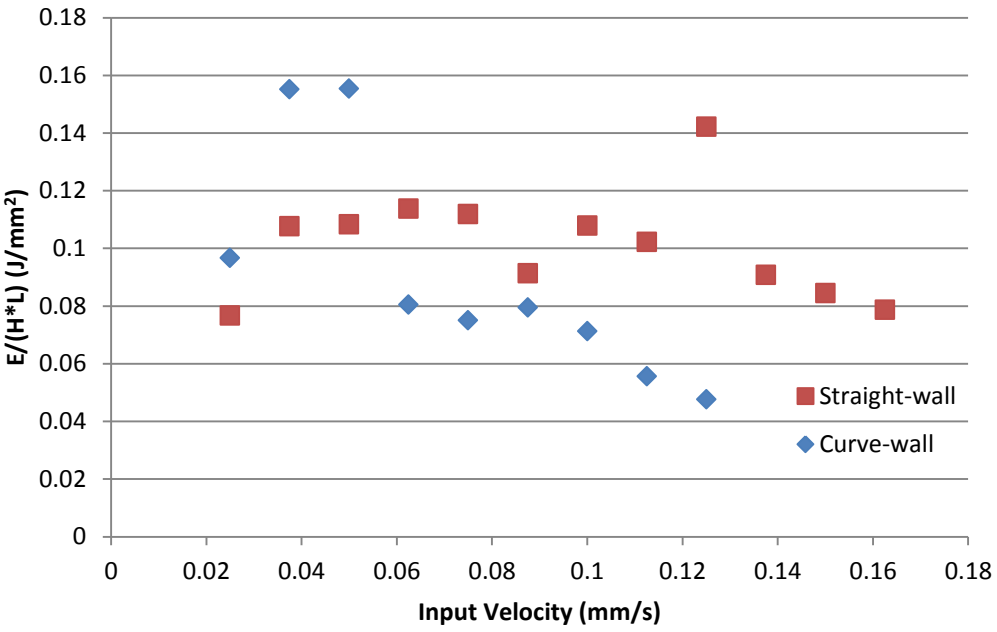

Figure 3.40: Comparison of *E/(H*L)* for the Three-variable Optimization Constrained by the Manufacturing Process as Input Velocity Increases

3.3.4 Three-variable Unconstrained by the Manufacturing Process

If the cells were not constrained by the manufacturing process, the three-variable cells are important to explore. The optimum cell angle decreases for the straight- and curved-walled cells as shown in Figure 3.41. For both cells, the optimum *h/l* increases with an increase in input velocity shown in Figure 3.42. However, the straight-walled cells always have a *h/l* value closer to the lower limit whereas the curved-walled cell approach the upper limit. Figure 3.43 shows the optimum contact gap for each cell. The contact gap varies throughout the range for both the straight- and curved-walled cells. Figure 3.44 shows that the maximum stress in the cell increases with increasing input velocity for the straight-walled cells and remains close to the stress limit for most of the curved-walled cells. The stress increases with increasing input velocity for the straight walled cells. The straight-walled cells have a better objective function when compared to the curved-walled cells as shown in Figure 3.45. This large discrepancy in the objective function is a result of a much lower *E* and a slightly higher *(H*L)* for the curved-walled cells. The values of *(H*L)* for the straight-walled cells are lower when compared to those for the curved-walled cells while the values of *E* are much higher.

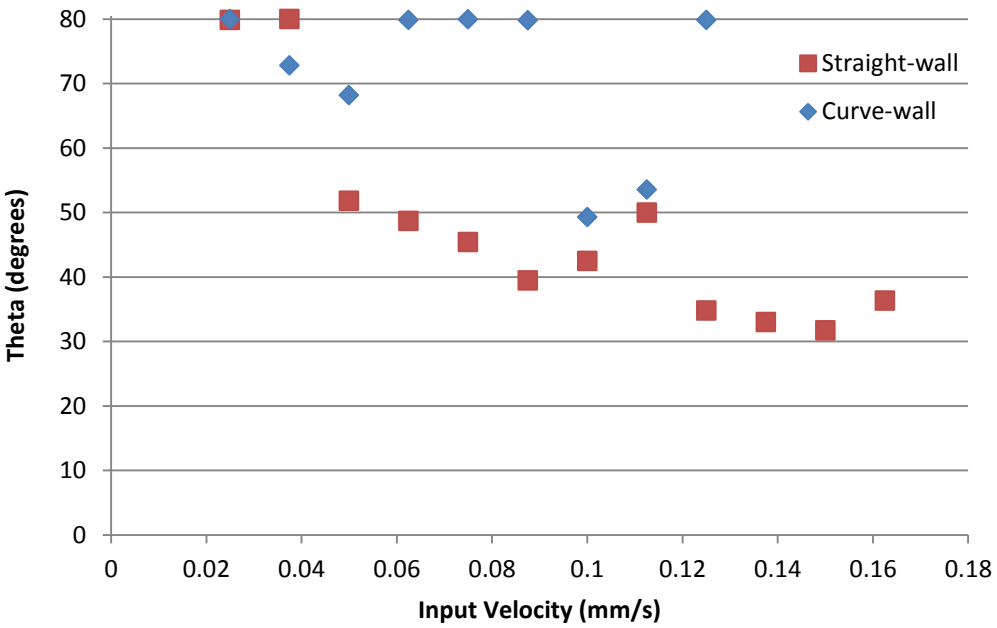

Figure 3.41: Comparison of θ for the Three-variable Optimization Unconstrained by the Manufacturing Process as Input Velocity Increases

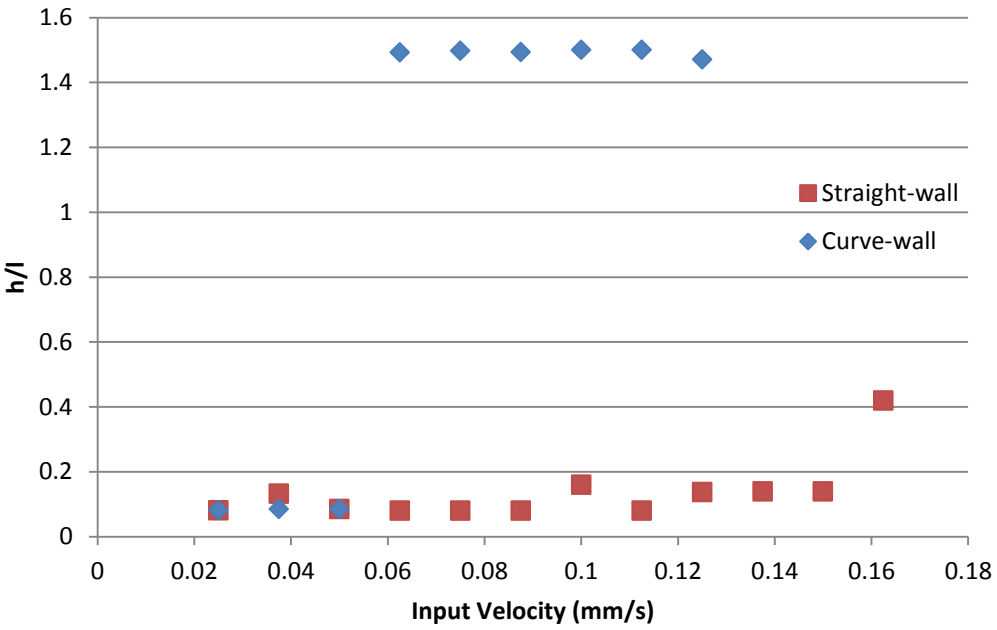

Figure 3.42: Comparison of *h/l* for the Three-variable Optimization Unconstrained by the Manufacturing Process as Input Velocity Increases

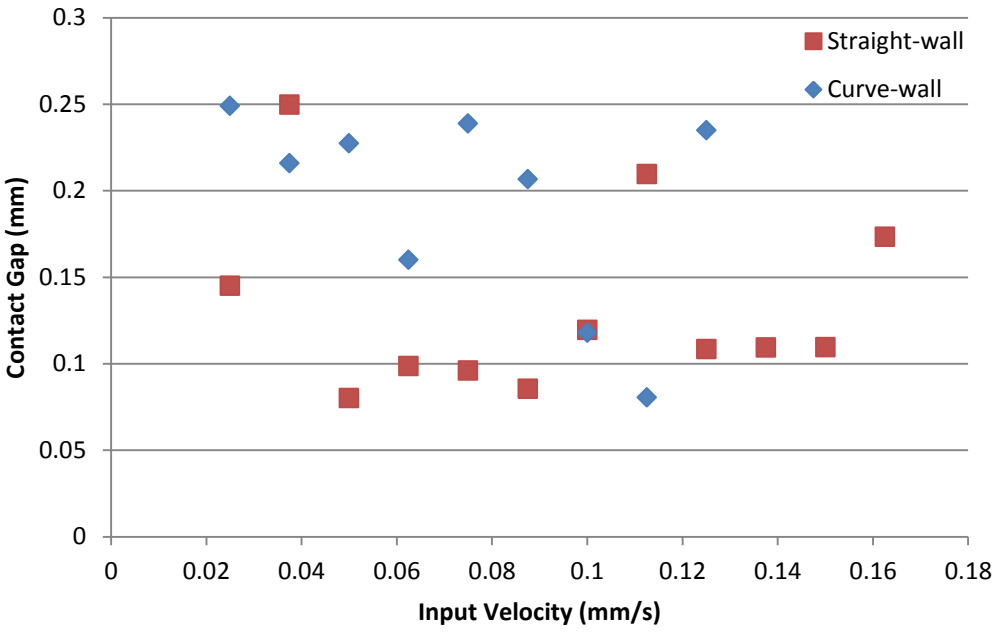

Figure 3.43: Comparison of γ for the Three-variable Optimization Unconstrained by the Manufacturing Process as Input Velocity Increases

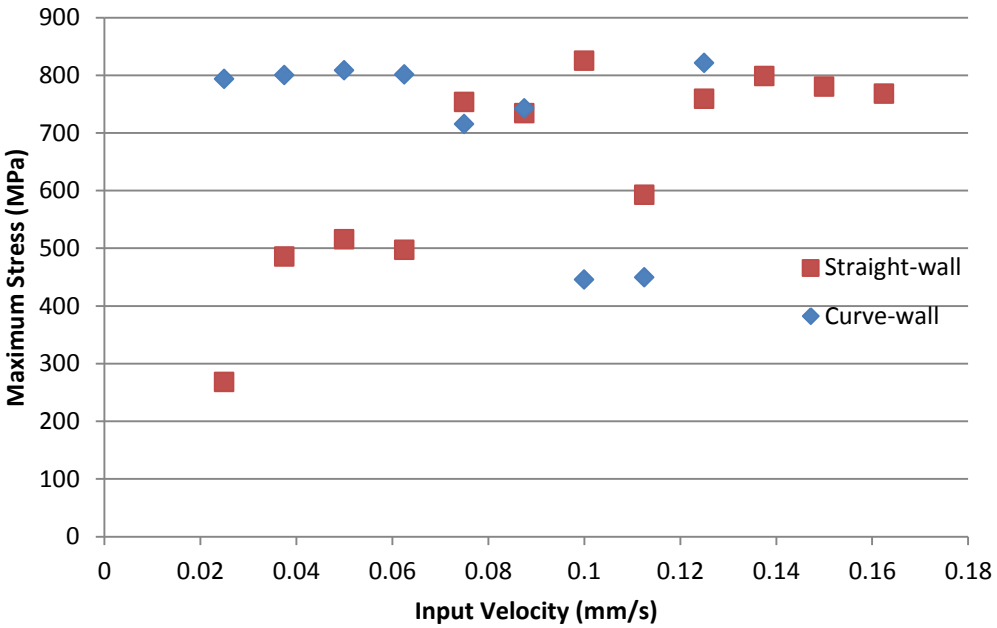

Figure 3.44: Comparison of the Maximum Stress for the Three-variable Optimization Unconstrained by the Manufacturing Process as Input Velocity Increases

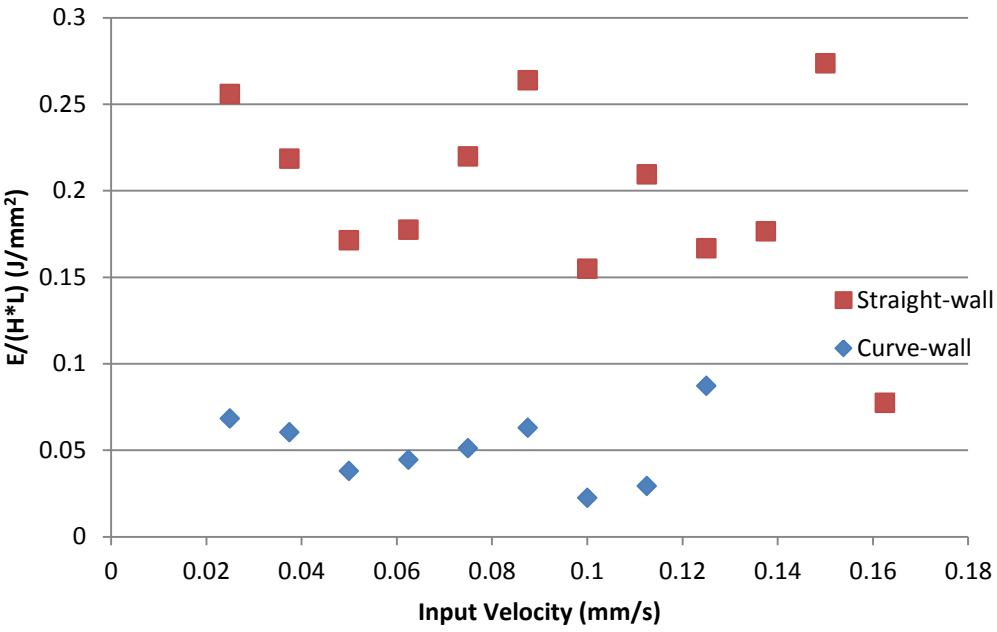

Figure 3.45: Comparison of *E/(H*L)* for the Three-variable Optimization Unconstrained by the Manufacturing Process as Input Velocity Increases

3.4 Summary of Results

When comparing all of the results, there is indeed an optimum cell to use. When looking at the cells that could be built by the LM-RIF process, the ideal cell changes with an increase in the input velocity. Table 3.11 shows the ideal shape for each input velocity when constrained by the manufacturing process. The green color indicates the three-variable curved-walled cells. The blue color indicates the same cell from both the two- and three-variable curved-walled cell. The red color indicates a two-variable curved-walled design. The purple color indicates two-variable straight-walled cells. The orange color indicates three-variable straight-walled cells. For all input velocities, both straight- and curved-walled, the cells look very similar. As shown in Figures 3.21 and 3.22, the curved-walled cells perform better with a smaller h/l and a larger angle, θ. The optimum curved-walled cells have an h/l value that approaches the lower bound and a θ that approaches the upper bound. This combination results in a shorter cell and a smaller fillet as shown in Figure 3.20. The results for the curved-walled cells look very similar to the straight-walled cells due to the small fillet.

When not constrained by the manufacturing process, the cells change as shown in Table 3.12. All optimum cells are straight-walled cells. The best cells with input velocities of 0.025, 0.0375, 0.1375, and 0.15 mm/s are cells found through the three-variable optimization. All other cells were found through the two-variable optimization.

Table 3.11: Ideal Cell Shape for Various Input Velocities While Constrained by the Manufacturing Process

Three-variable curved-wall	Two- & Three-variable curved-wall	Two-variable curved-wall	Two-variable straight-wall	Three-variable straight-wall
Input Velocity (mm/s)	Cell Shape -------- 4 mm	Input Velocity (mm/s)	Cell Shape -------- 4 mm	
0.025	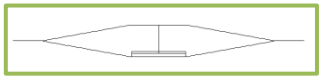	0.1	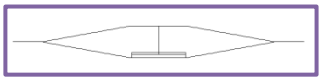	
0.0375	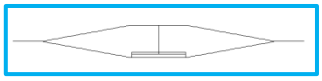	0.1125	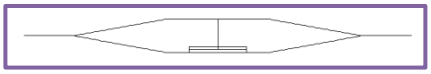	
0.05	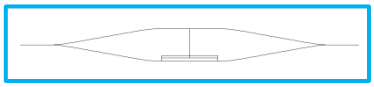	0.125	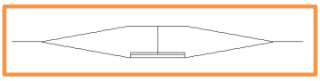	
0.0625	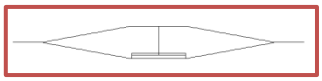	0.1375	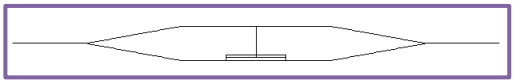	
0.075	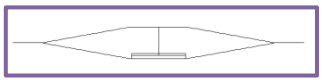	0.15	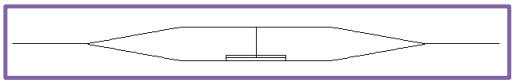	
0.0875	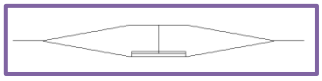	0.1625	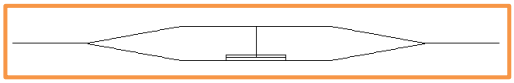	

Table 3.12: Ideal Cell Shape for Various Input Velocities While Not Constrained by the Manufacturing Process

Input Velocity (mm/s)	Cell Shape ——— 4 mm	Input Velocity (mm/s)	Cell Shape ——— 4 mm
0.025	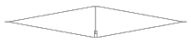	0.1	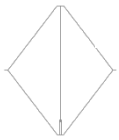
0.0375		0.1125	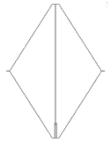
0.05	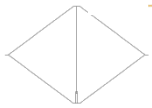	0.125	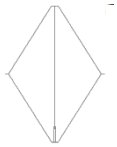
0.0625	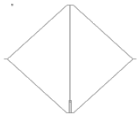	0.1375	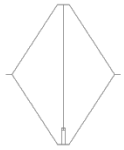
0.075	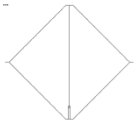	0.15	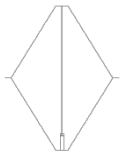
0.0875	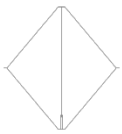	0.1625	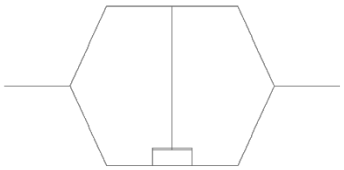

3.5 Summary

This chapter has described the optimized results for the optimization algorithm presented in Chapter 2. It first introduced the bounds selected for the cells. Two sets of bounds were selected. The first set of bounds was selected based on the constraints imposed by the manufacturing process. The second set of bounds was selected based on the ideal contact mechanism width, w_{cm}. The optimization algorithm was then run and the results

were presented. A comparison was made between the cells where w_{cm} was constrained by the manufacturing process and where it was fixed at 30% of h. There was also a comparison between the straight-walled cells and the curved-walled cells. The results presented in this chapter will be used in Chapter 4 to fabricate and test cells.

Chapter 4: Fabrication and Testing

After finding the optimized C^3M designs, the designs must be fabricated and tested in order to validate the predicted results. Two different manufacturing processes, LM-RIF as discussed in Chapter 1 and laser micro-machining, were used to fabricate the parts. First, the exact part dimensions were determined. Next, the mask layout is created and the parts are manufactured. The parts were also fabricated using laser micromachining. The parts are then tested and the results are presented.

4.1 Designs for Fabrication Using LM-RIF

Fabricating the C^3M structures using the LM-RIF process reveals that there are various constraints that need to be taken into account when designing the structures. Most of these constraints were taken into account during the design of these C^3M structures as seen in Section 3.1. These constraints affect the minimum in-plane wall thickness, t_{min}, minimum out-of-plane wall thickness, d_{min}, minimum contact gap, γ_{min} and the maximum aspect ratio, AR_{max}.

The first design constraint limits the minimum values for in-plane and out-of-plane wall thickness, t and d. This constraint is dictated by two things, manufacturability of the mold and parts, and particle size. First, the mold must be at least 100 microns thick because it is very difficult to manufacture molds that are very thin using the LM-RIF process. It would also be infeasible to manufacture specimens with an in-plane wall thickness that is less than 100 microns because they would be very fragile and difficult to handle. Because of this, a minimum in-plane and out-of-plane wall thickness of at least 100 microns will be assumed as the smallest manufacturable thickness. Second, the maximum particle size of the powder is also important to consider. In order for the design to be feasible, we have assumed that there must be at least 10 particles of powder across any dimension in the part [32]. The average particle size of the metallic powders are 10 microns [29]. This means that in order to have at least 10 particles across the smallest allowable in-plane and out-of-plane wall thicknesses are 100 microns for meso-scale 316L SS. During the optimization process, it

was assumed that *t* will be 300 microns and *d* will be 400 microns which are both larger than the minimum constraints.

The next design constraint involves the smallest feature resolution that can be obtained in the mold, which is a function of the mold thickness, or out-of-plane thickness of the part. As a guideline, it has been assumed that the smallest feature resolution is about equal to 1/10 of the out-of-plane thickness [32]. In the design of C^3M specimen, the smallest feature size is generally the contact gap. The minimum contact gap is therefore set to 1/10 of the out-of-plane thickness, *d*. The C^3M specimens will be fabricated with an out-of-plane thickness of 400 microns, therefore 40 microns will be assumed as the minimum contact gap.

The final manufacturing constraint involves the aspect ratio of the C^3M structures. Aspect ratio, *AR*, has to do with the slenderness of the walls in the structure, and is a function of both wall length and thickness. The percentage of successful parts, or part yield, decreases with an increase in aspect ratio, as shown in [58]. Because of this, there is a limitation on the maximum aspect ratio. The maximum aspect ratios that can be manufactured using the LM-RIF process are assumed to be 40 for meso-scale 316L SS [29]. Equation 4.1 will be used to calculate the aspect ratio of the cells [32].

$$AR = \frac{\max(l, h)}{\min(t, w)} \tag{4.1}$$

There were three cells that were chosen to manufacture. The first cell was one of the optimized contact-aided designs. Because there is not much of a difference between the straight- and curved-walled optimized designs, two comparison cells were selected. The cells were selected based on the fact that with an input velocity of 0.075 mm/s over a period of two seconds, the curved-walled cell had a *E/(H*L)* value of 0.0030437 J/mm^2 and the straight-walled cell had a *E/(H*L)* value of 0.0028454 J/mm^2. The reason the two cells were chosen for a comparison is that the curved-walled cell had a higher *E/(H*L)* value when compared to the straight-walled cells. As stated before, curved-walled cells are easier to manufacture and have fewer stress concentrations. Table 4.1 shows that three cells manufactured and their corresponding dimensions. All minimum requirements are met and the aspect ratio is below the maximum.

Table 4.1: Dimensions for each of the manufactured C^3M designs

	Optimized Contact-aided 	Straight-walled Comparison 	Curved-walled Comparison 
h	2.6 mm	4.4 mm	4.4 mm
l	4 mm	4 mm	4 mm
θ	80 deg	60 deg	60 deg
γ	90 μm	90 μm	90 μm
w_{cm}	2.42 mm	2.42 mm	2.42 mm
t	300 μm	300 μm	300 μm
r	---	---	3.689 mm
d	400 μm	400 μm	400 μm
AR	13.333	14.667	14.667

4.2 Mask Design

Once the final designs were selected, single parts and their corresponding arrays were designed. Because the basis for this work was to show that the addition of the contact mechanism improves the performance of the cell, both contact-aided and non-contact cells are fabricated. Figure 4.1 shows the optimized cells that were fabricated. Figure 4.2 shows the straight-walled comparison cells that were fabricated. Figure 4.3 shows the curved-walled comparison cells that were fabricated. For all cells, if there was a sharp corner, a fillet of 50 microns was included to help reduce stress concentrations. The cellular arrays were not selected to be any larger than a 2x2 because previous arrays larger than 2x2 were usually not testable and take up valuable space on the mask. It was more beneficial to have more single cells and smaller arrays because the part yield of larger arrays is typically poor using the LM-RIF process.

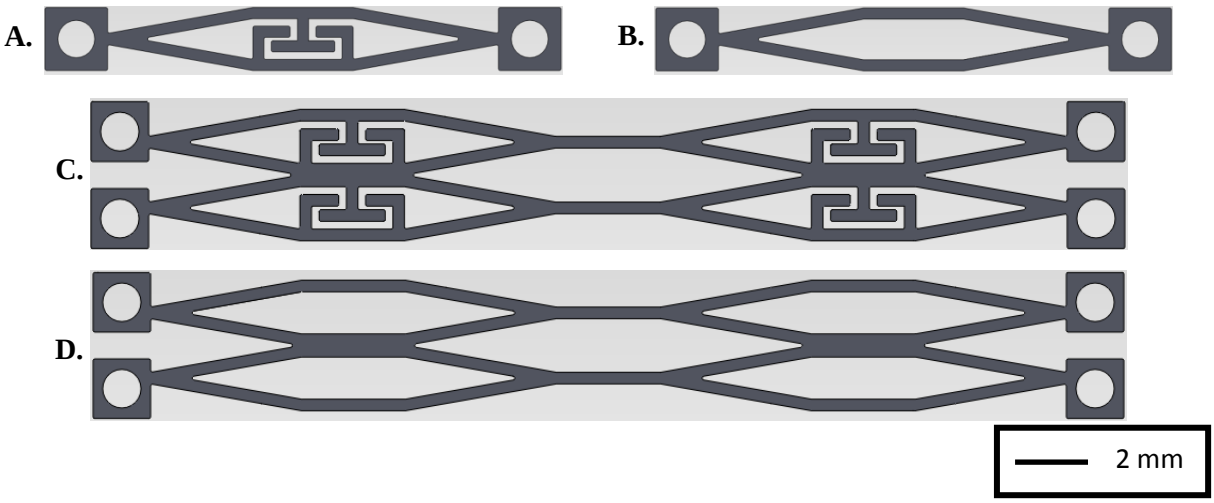

Figure 4.1: The designs to be fabricated, a single contact-aided cell (A), a single non-contact cell (B), a 2x2 contact-aided array (C), and a 2x2 non-contact array (D) using the LM-RIF process based on the optimized results in Chapter 3.

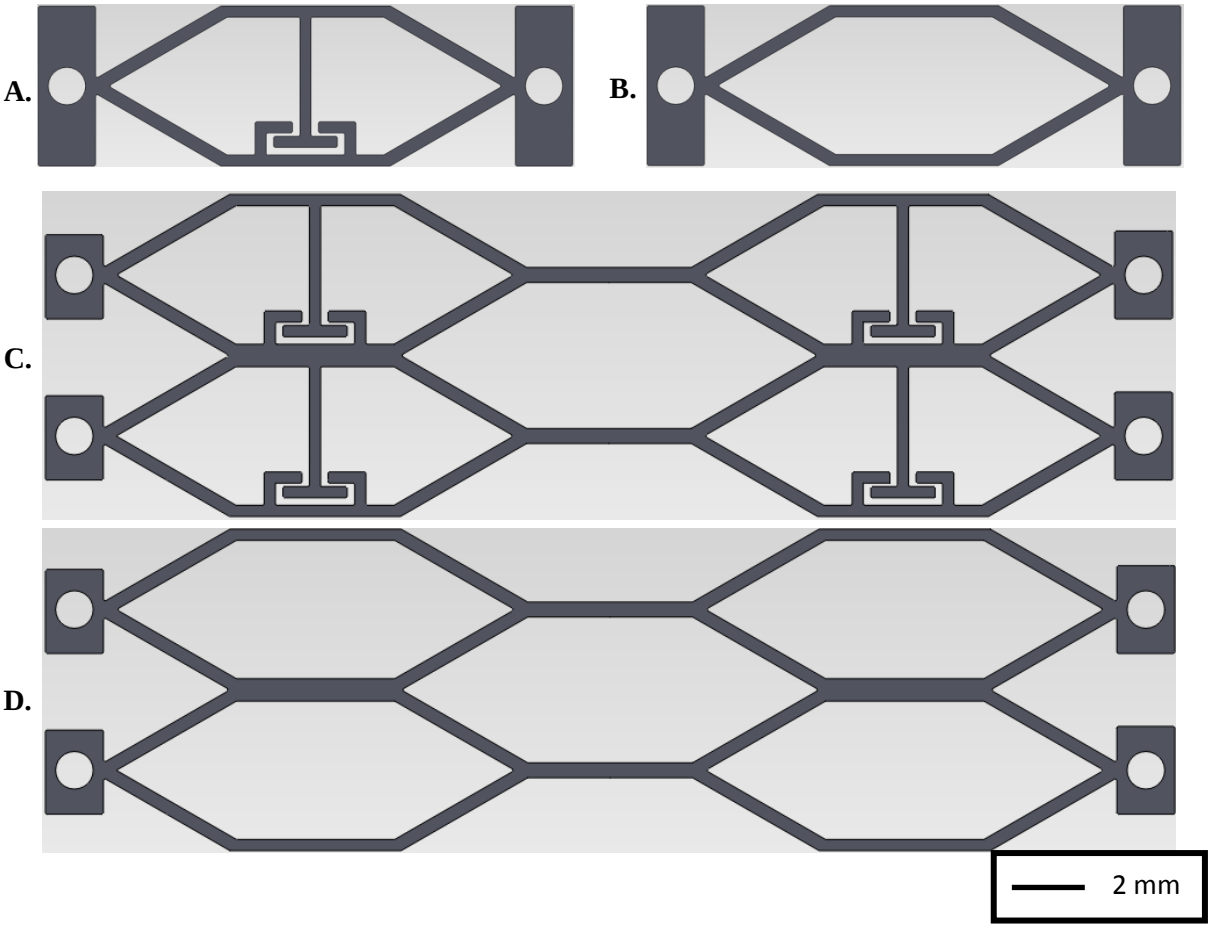

Figure 4.2: The designs to be fabricated, a single straight-walled contact-aided cell (A), a straight-walled single non-contact cell (B), a straight-walled 2x2 contact-aided array (C), and a straight-walled 2x2 non-contact array (D) using the LM-RIF process.

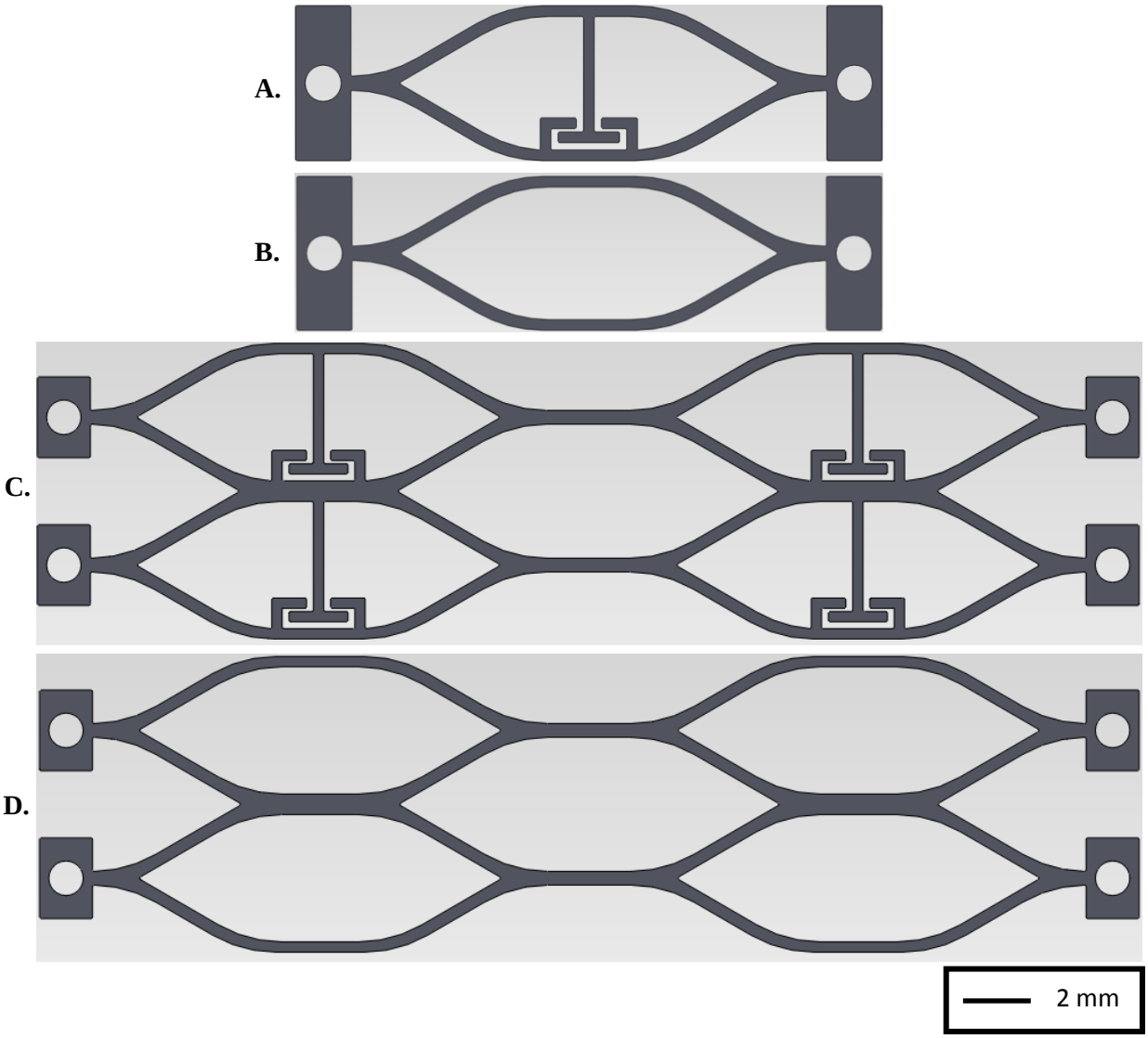

Figure 4.3: The designs to be fabricated, a single curved-walled contact-aided cell (A), a single curved-walled non-contact cell (B), a 2x2 curved-walled contact-aided array (C), and a 2x2 curved-walled non-contact array (D) using the LM-RIF process.

Due to constraints imposed by the size of the mask, the non-contact comparison cells and arrays were not put on the mask. Once fabricated parts were made, the contact mechanism for these cells and arrays can cut out to result in non-contact comparison cells and arrays. This was not done to the optimized cells because of how compact the cell is. Figure 4.4 shows the mask layout that was created by our collaborators Brian Babcox and Dr. Jim Adair. The minimum gap between parts is assumed to be 400 microns. There are 30 optimized contact-aided cells, 16 optimized cells without a contact mechanism, and 7 optimized contact-aided cellular arrays. For the comparison cells, there are 16 straight-

walled contact-aided cells, 4 straight-walled contact aided arrays, 17 curved-walled contact-aided cells, and three curved-walled contact-aided arrays. There are several parts on the mask that are not shown above. These parts will be used by our collaborators for future material testing purposes.

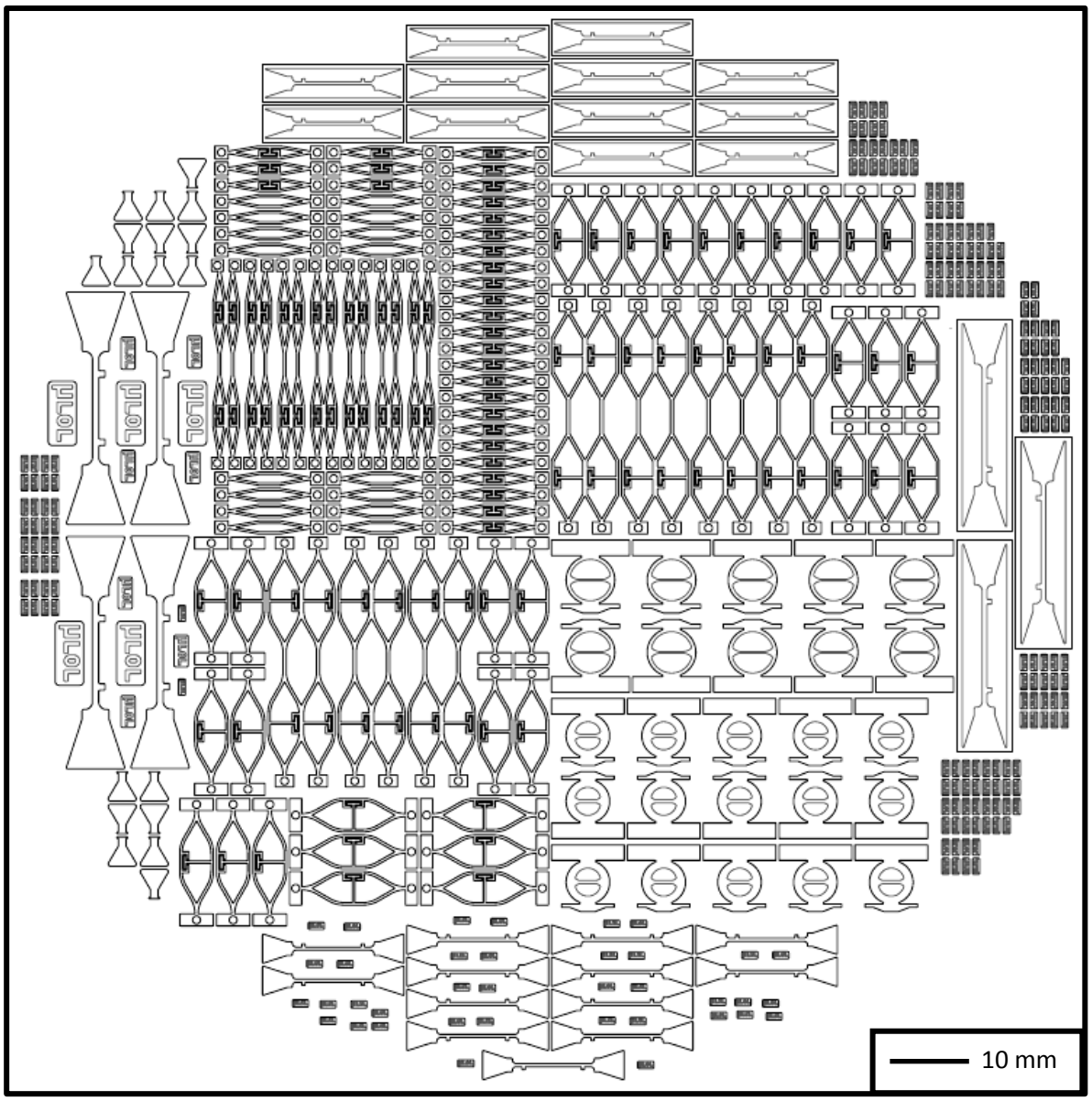

Figure 4.4: Mask layout

4.3 Fabrication using LM-RIF

Once the mask has been designed, it is sent out to be fabricated by Photo Sciences Inc. This photolithographic mask is used to begin the LM-RIF process. Once the mask is created, it is used to fabricate the molds, which are then use to fabricate the four designs. All fabrication is completed by our collaborators Brian Babcox, Chris Leh, and Dr. Jim Adair. To date, the curved C^3M structures have only been fabricated using the meso-scale 316L stainless steel material, however straight-walled C^3M structures have been fabricated using a composite meso-scale stainless steel and zirconia material [11]. Several key stages in fabricating the meso-scale 316L SS C^3M structures are shown in Figure 4.5 including a picture of the fabricated mask, the empty SU-8 mold, the mold filled with slurry and the finished parts. Figure 4.6 shows a close up view of the contact mechanism from the cell found in Figure 4.5 (D). As anticipated, the fabrication process does not result in parts that look exactly like the designed parts. These parts have flaws that are a result of the stresses caused on the parts by the molds. The parts tend to be bent, warped, or have inconsistent wall thicknesses. When the parts are bent and warped, the parts are not able to be tested. As seen in Figure 4.6 there is leftover SU-8 mold material and possibly some 316L SS material within the contact mechanism. Material in the contact mechanism will interfere with the contact surfaces and therefore the part was not tested. Currently, this process is being perfected. Because parts manufactured via the LM-RIF process were not testable, parts were also laser micro-machined.

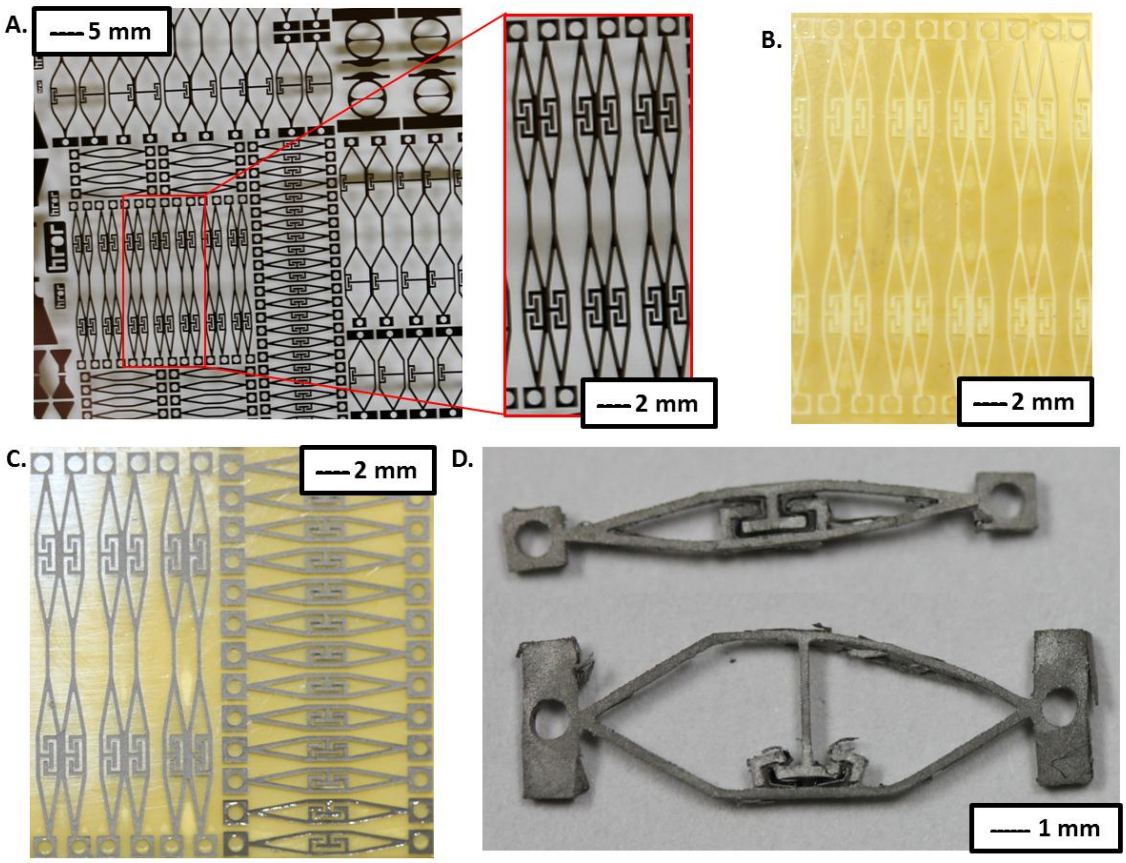

Figure 4.5: Fabrication of C^{3}M structures: the mask (A), the empty mold (B), the filled mold (C) and a finished part (D)

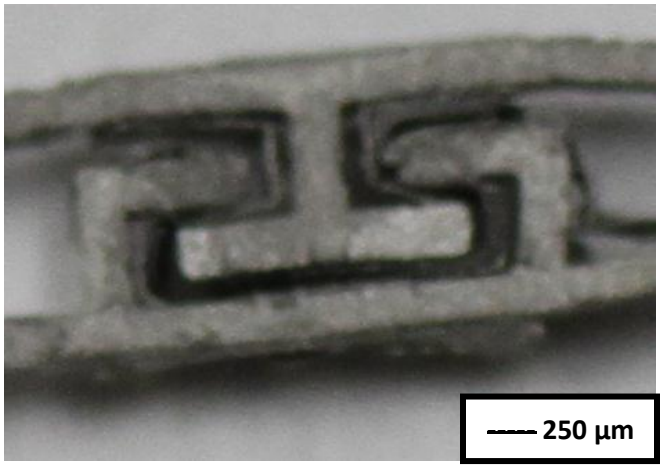

Figure 4.6: Zoomed in view of the contact mechanism

4.4 Fabrication via Laser Micro-machining

The parts were also fabricated using laser micro-machining by Benjamin Hall and Dr. Ted Reutzel at Penn State Applied Research Lab. The laser that was used was a Coherent Avia ultraviolet Q-switched laser with pulse energy of about 100 micro-Joules. Q-switched lasers have pulse durations in the nano-second range. They offer a processing regime where the material is ablated. Two different methods were used to attempt to fabricate the parts. The first method was the vector method. The vector method follows the outline of the part and leaves all material intact except the outline. Due to the complexity of the contact mechanism, it was not possible to remove the remaining material surrounding the contact mechanism without bending the parts. The second method that was used was the raster method. Although this technique is usually used for engraving purposes, this method was chosen because it allows for complete removal of the material surrounding the contact mechanism. The raster method is done by the laser moving back and forth over the material like a printer and removes material where desired. This method takes much longer because it travels over the whole part rather than just over the outline. Using the raster method, the contact gap was able to be fabricated. Figure 4.7 shows two parts fabricated using the two different methods. The top cell was fabricated using the raster method whereas the bottom cell was fabricated using the vector method.

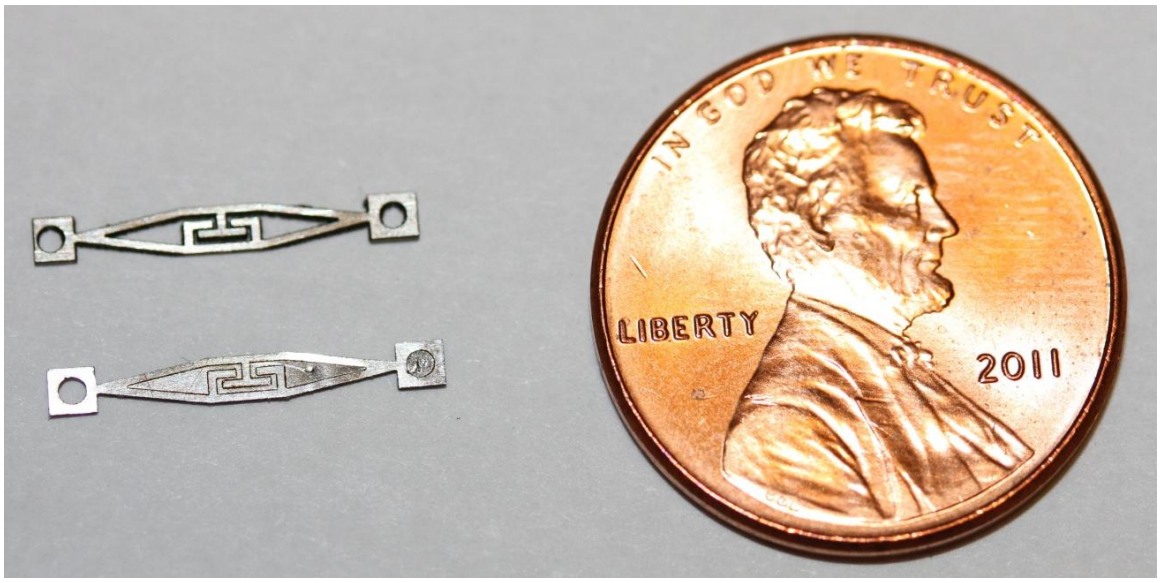

Figure 4.7: The same optimized cell fabricated using the raster method (top) and the vector method (bottom).

Due to limitation with the power of the laser, the parts were fabricated from 316 stainless steel shims with a thickness of 254 microns. Figure 4.8 shows one of each of the single C^3M cells fabricated using the raster method. Figure 4.9 shows the back side of the part showing that the laser did cut all the way through the metal shim. Although the laser cut through the metal shim, the gap on the back side of the cell is slightly less than the gap on the top side. The material test report (MTR) for these shims can be found in Appendix C. With a more powerful laser, the parts could be fabricated much faster and with larger thicknesses.

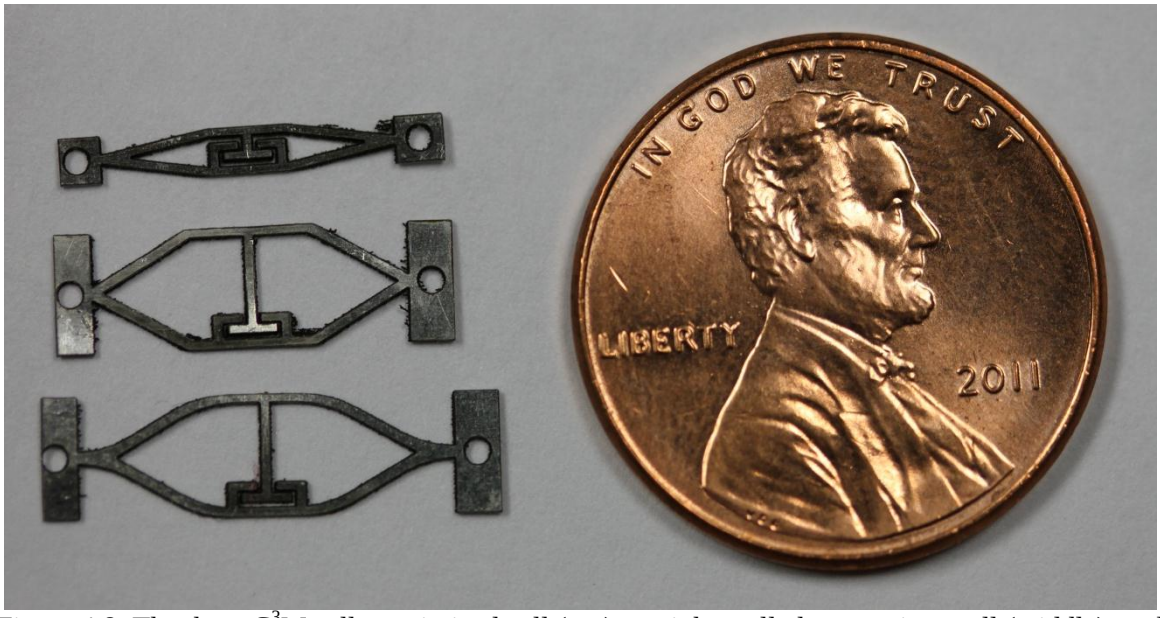

Figure 4.8: The three C^3M cells, optimized cell (top), straight-walled comparison cell (middle), and curved-walled comparison cell (bottom), fabricated using the raster method.

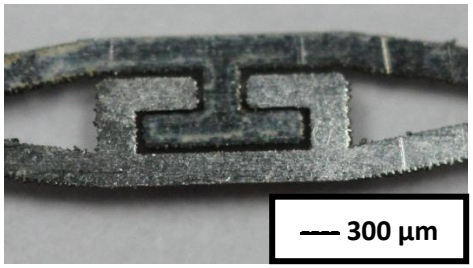

Figure 4.9: The back side of the part showing that the laser did cut all the way through the metal shim.

4.5 Test Rig

A custom test rig was built by our collaborators Brian Babcox and Chris Leh. This test rig was built to be used with an Instron machine for compression testing. A schematic of the test rig can be seen in Figure 4.10. The test-rig was built in three parts and then combined. This allows for versatility in future testing. The two components, indicated in blue, are made of Teflon. The black component is a piece of sheet metal which is interchangeable. For these tests, the sheet metal is 400 microns thick. Bolts are then threaded through the components and tightened. The part is then inserted into the test rig and is resting on the sheet metal. The test rig with a part inserted can be seen in Figure 4.11. A glass slide is inserted to insure that the cells do not deflect out of plane.

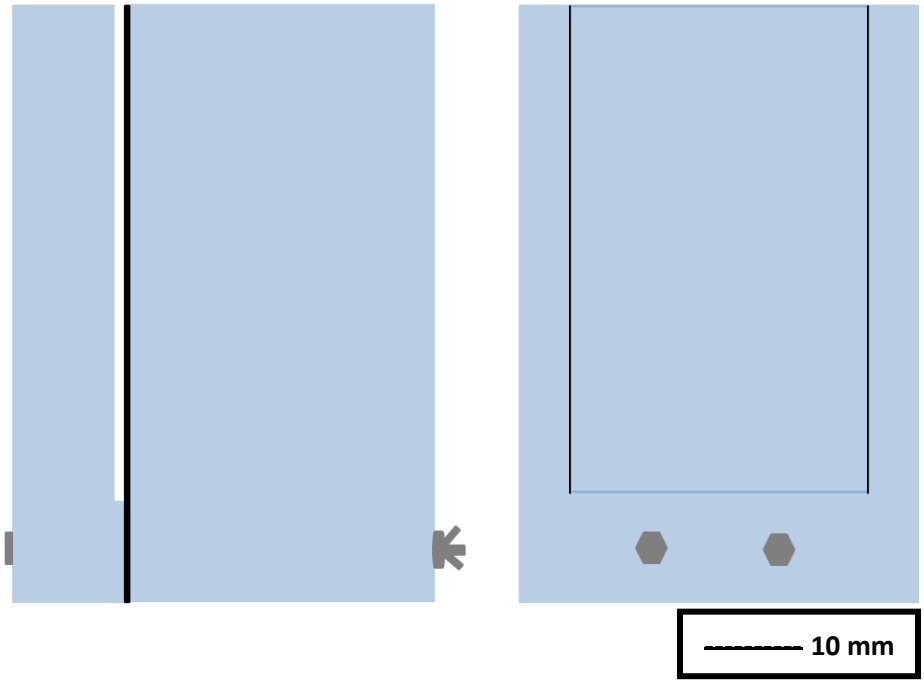

Figure 4.10: Schematic of test rig fabricated for use with the Instron for compression testing.

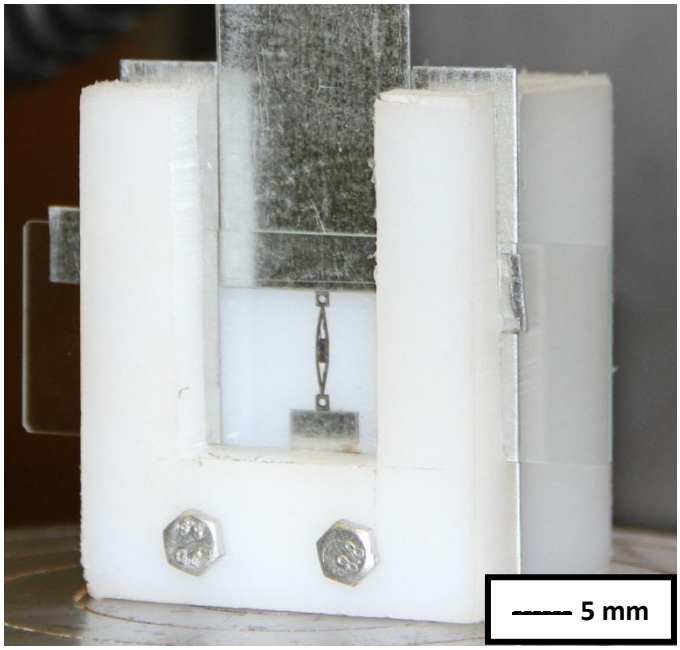

Figure 4.11: Test rig fabricated for use with the Instron for compression testing with a part inserted.

4.6 Testing Procedure

For the testing of the fabricated C^3M parts, an Instron series 5800 load frame was used. The model used was the Instron 5866. The load cell that was chosen was a 1 kN load cell, serial number 688. This load cell was chosen because it ensures the full load profile will be captured and it has an easy attachment for the vertical compression plate. The part is then inserted into the test rig and aligned so the compression plate will compress the part vertically. The load rate and time duration can be selected and adjusted as needed. The load rates were determined by ANSYS simulation runs with the new material model. The simulation results indicated that contact would occur. A Dino-Lite AM311S video camera was used to record the cell deforming under compression. The camera is used to see when contact occurs while also allowing it to be seen if the cell deforms out of plane by a change in the lighting. Figure 4.12 shows the full test set-up including the custom built test rig and the video camera. The compression testing was completed with the assistance of Brian Babcox.

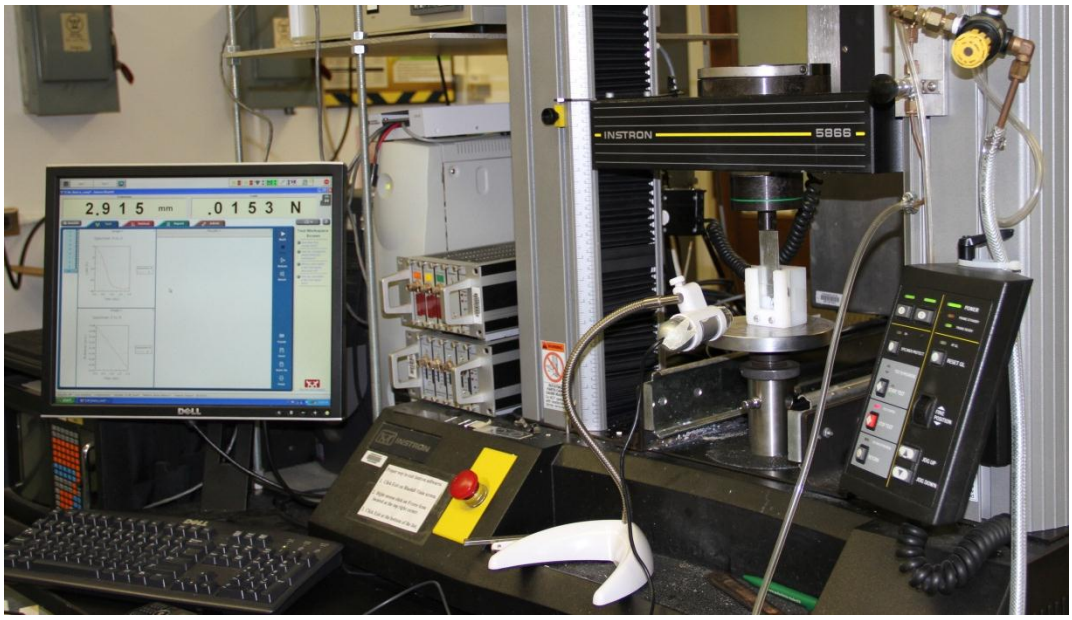

Figure 4.12: The complete test set-up including the test rig and the video camera.

4.7 Results

Due to issues with the LM-RIF process, the only parts that were tested were those that were laser micro-machined. ANSYS simulations were re-run with the new part thickness of 254 microns and the assumed material model show in Figure 4.13. This material model was extracted from the MTR found in Appendix C. The assumed Young's Modulus is 193 GPa. Using the assumed Young's Modulus, the strain value of 0.003535 for the 0.2% yield strength was calculated. An additional point was inserted at 0.001 strain with a value of 193 MPa. Force-deflection data is used as the metric for comparison because of the ability to extract this data from the compression testing along with the simulation results. It would have been extremely difficult to calculate the energy absorption of the single cells due to their small sizes.

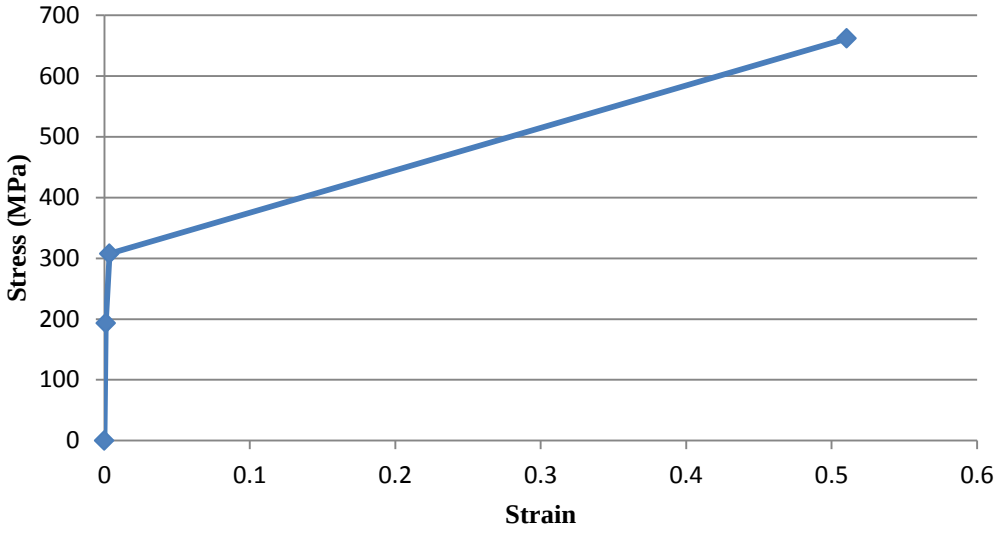

Figure 4.13: Stress-strain curve extracted from the material testing report found in Appendix C used for simulation to compare to test results.

The first test that was run was on the straight-walled comparison cell. Using the Instron, the load rate was 75 microns/sec for 2 seconds. To compare with the simulation results, two simulations were run. The reason that two different simulations were run was due to the fact that the cells are only single cells and not part of the array. The first simulation that was run was one utilizing the boundary conditions found in Section 2.2.3. For the second simulation, the boundary conditions are shown in Figure 4.14. The nodes on the entire bottom edge of the cell are permitted to displace only in the X-direction, i.e., there is no Y-displacement and no rotation. The right side of the cell is subjected to an input velocity, *V*, in the negative X-direction, and the left most node of the cell is fixed in the X- and Y-directions.

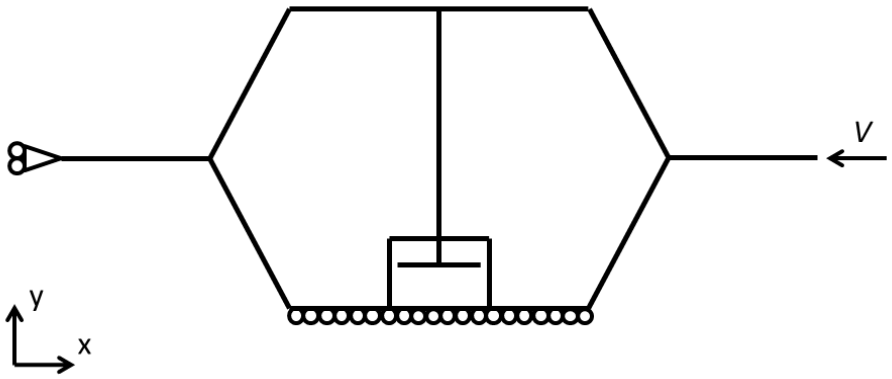

Figure 4.14: Boundary Conditions Applied Using FEA for Second Simulation Run

For the testing using the Instron, there was a slight pre-load to ensure that the cell experiences the full input over the time. The only way to ensure this is to slightly pre-load the cell without causing visible deformation. The results are presented in in Figure 4.15 and the pre-load of 0.140 N was removed from all force values to represent an initial zero load. The blue diamonds indicate the results obtained through the compression testing. These values were obtained through the compressive load measured by the load cell and the displacement measured by the cross-head. The green triangles indicate the first simulation where both the top and bottom walls on constrained as part of a cellular array. The red squares indicate the second simulation run where the top wall was no longer constrained. The vertical purple line indicates when contact occurs during the simulation runs. The simulation results were obtained by extracting the reaction force in the X-direction from the left hand side of the cell and the displacement in the X-direction from the right hand side of the cell. It can be seen that the test results differ from the two simulation runs. As seen in Figures 4.16 and 4.17, the simulation where the top wall is not constrained shows the same deformation in the top wall when compared to the actual deformed cell. The ratio of the height of the middle of the cell to the original cell height for the test results is 1.0864 where the simulation results have a ratio of 1.0195. When the top wall is constrained, the contact mechanism contains the highest stress. When the top wall is not constrained, the highest stress can be seen in the top wall. The stress distribution plots can be seen in Appendix D. The discrepancies between the simulations and the test results can be attributed to a few testing errors. Although the test rig is made out of Teflon, there is still friction that results

from the part sliding against either the Teflon or the glass slide. There is also friction between the compression plate and the guide plates. This friction would cause higher forces to be seen. The compression plate also slides against the Teflon and the glass slide. Any friction seen be the compression plate would be transferred to the load cell even if the part does not directly experience this added force. Also, as the part is being compressed, it is possible that the plate compressing the part can shift slightly to either side causing a change in the force-displacement graph. The material model that was used is also an approximate model based on three data points. If a more accurate material model was known, the simulation results should be much closer. The laser micro-machining also changes the micro structure of the material. These changes are not accounted for in the material model.

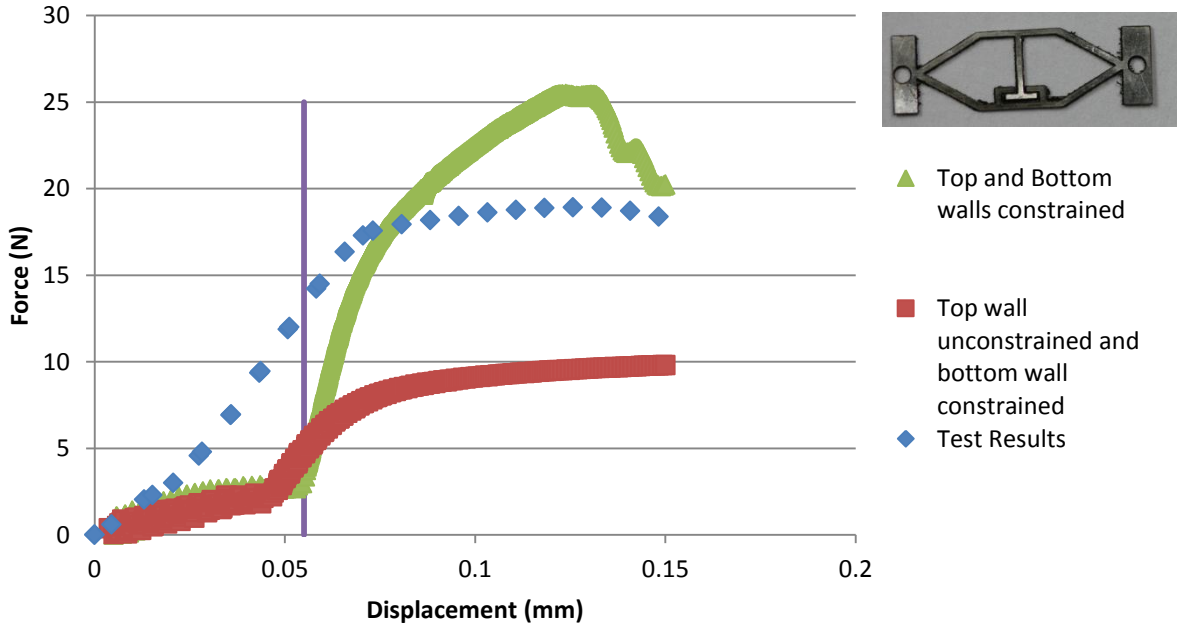

Figure 4.15: Comparison of Instron Compression Testing and ANSYS Simulation Results for the Straight-walled Comparison Cell

Figure 4.16: Deformed Cell After Compression Testing

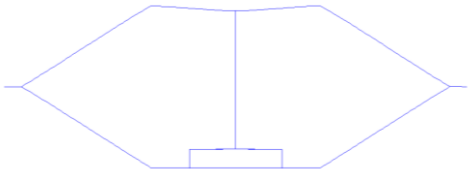

Figure 4.17: Deformed Cell Via Simulation where the Top Wall was not Constrained

`The next test that was run was that of the curved-wall comparison cell. For this cell, the load rate was 60 microns/sec for 2 seconds. Again, two simulations were run with the two different sets of boundary conditions. For the testing using the Instron, there was a slight pre-load. The results are presented in in Figure 4.18 where the pre-load of 0.126 N was removed and all values were adjusted accordingly. Again, the blue diamonds indicate the results obtained through the compression testing. The green triangles indicate the first simulation where both the top and bottom walls on constrained as part of a cellular array. The red squares indicate the second simulation run where the top wall was no longer constrained. The vertical purple line indicates when contact occurs during the simulation runs. It can be seen that the test results differ from the two simulation runs. For these results, comparison of the compression test results and the simulation results where the top and bottom walls are constrained are similar. Again, sliding friction could have caused an increase in the force felt by the load cell. As the part was being compressed, the part buckled out-of-plane. This was caused by the fact that the gap between the Teflon and the glass slide was 400 microns and the part was 254 microns. The stress distribution plots can be seen in Appendix D.

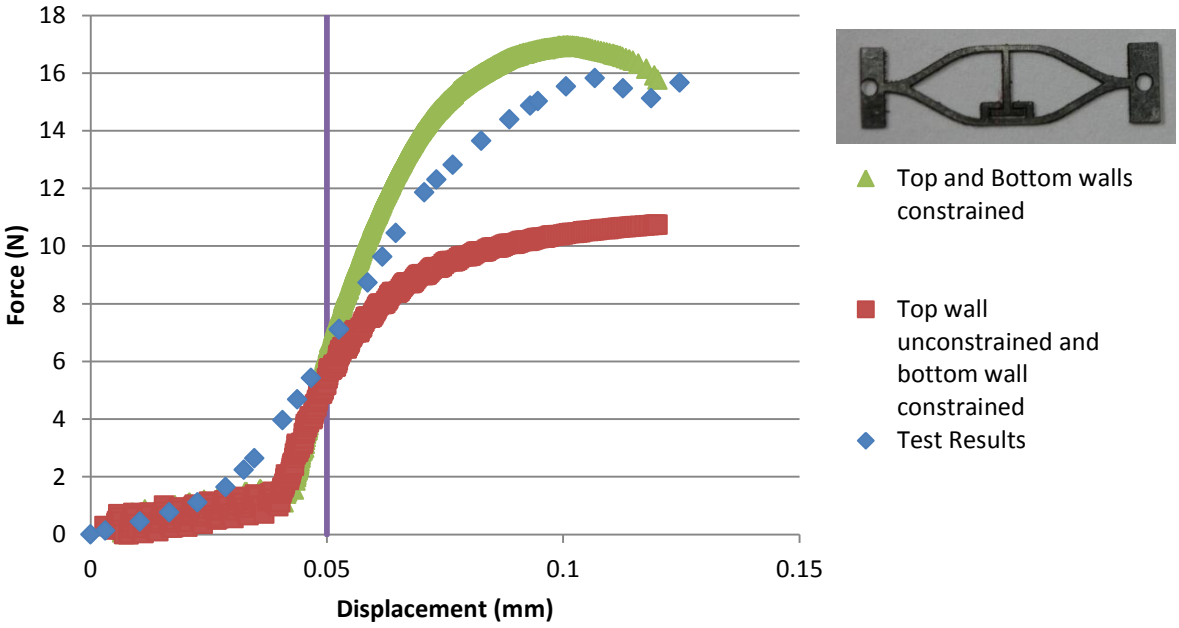

Figure 4.18: Comparison of Instron Compression Testing and ANSYS Simulation Results for the Curved-walled Comparison Cell

The two tests that were run were on the optimized cell. For the first test, the load rate was 30 microns/sec for 2 seconds. For the second test, the load rate was 50 microns/sec for 2 seconds because contact did not occur at the slower load rate. Again, two simulations were run with the two different sets of boundary conditions. For the testing using the Instron, there was a slight pre-load. The results for the first test are presented in in Figure 4.19 where the pre-load of 0.141 N was removed and all values were adjusted accordingly. The results for the second test are presented in in Figure 4.20 where the pre-load of 0.626 N was removed and all values were adjusted accordingly. Again, the blue diamonds indicate the results obtained through the compression testing. The green triangles indicate the first simulation where both the top and bottom walls on constrained as part of a cellular array. The red squares indicate the second simulation run where the top wall was no longer constrained. The vertical purple line indicates when contact occurs during the simulation runs. For the first test, the cell barely moved at all and contact did not visibly occur. The simulations indicate that contact occurs with a force of about 5 N. The maximum force extracted from the load cell was only 8.13 N. It is possible that the cell never experienced the 5 N of force that the simulation predicted necessary of contact to occur due to the cell buckling out of plane. For the second test, contact occurred on the back face of the part and then the part buckled out of plane. The stress distribution plots for the various simulation runs can be seen in Appendix D.

The highest load rate and time that was used for compression testing is 75 microns/sec for 2 seconds. With a larger array of cells, higher load rates could be used which would result in rates closer to that of a real impact. For the single cells, the load rates are closer to those used for quasi-static crushing.

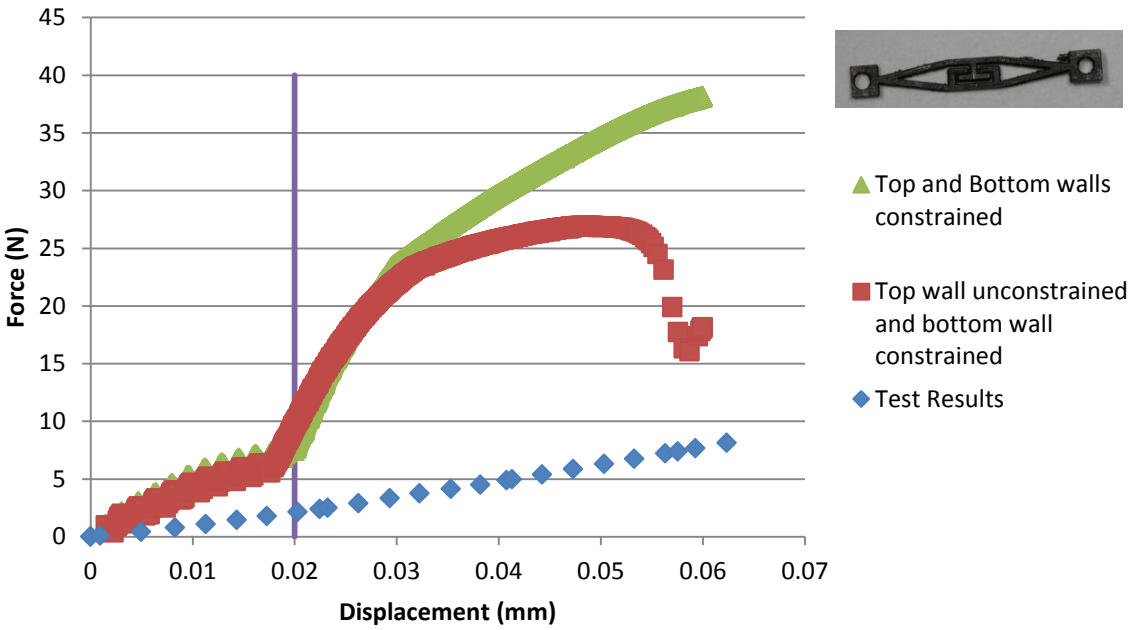

Figure 4.19: Comparison of Instron Compression Testing and ANSYS Simulation Results for the Optimized Cell for an Input Velocity of 30 microns/sec for 2 seconds

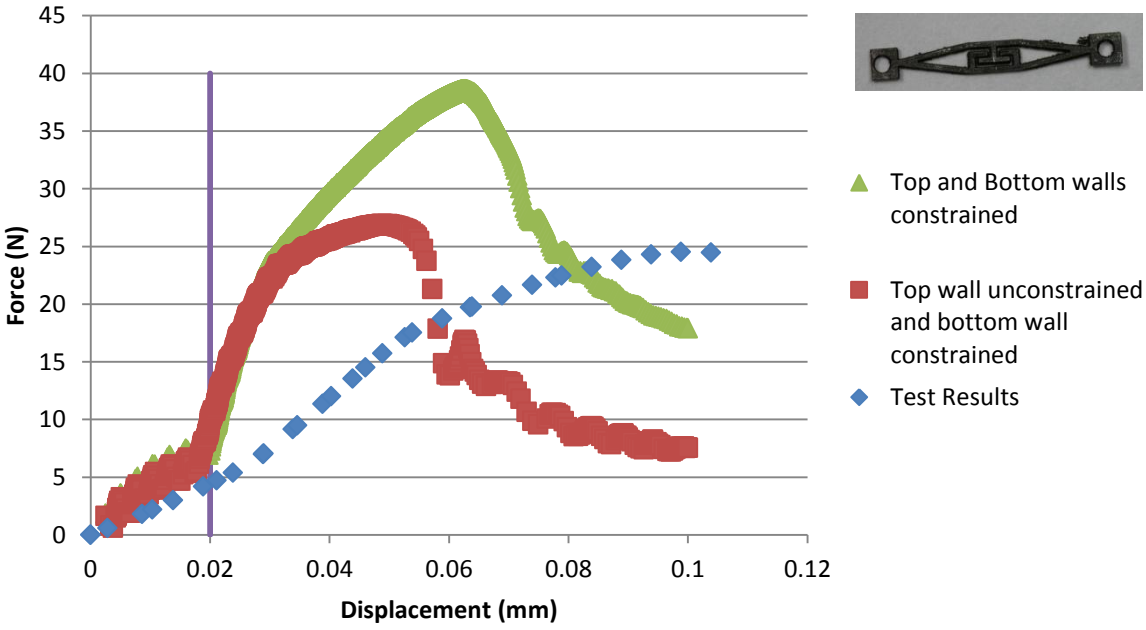

Figure 4.20: Comparison of Instron Compression Testing and ANSYS Simulation Results for the Optimized Cell for an Input Velocity of 50 microns/sec for 2 seconds

4.8 Summary

This chapter has described the fabrication of the cells via two methods. It was found that there were geometric variations in the parts fabricated via LM-RIF, which could be seen in the form of warping, cracks, and inconsistent wall thicknesses which resulted in parts that were not testable. Due to the time required to raster the parts, only four cells were fabricated via laser micro-machining. The test rig and testing procedure were first introduced. Finally, the experimental results from mechanical testing of the three different C^3M structures were presented.

Chapter 5: Conclusions, Recommendations, and Future Work

This thesis has presented C^3M specimens with straight and curved walls to be used as energy absorbing structures. The goal of this work was to develop a cellular structure with a contact mechanism that can absorb more energy compared to the same sized cell without a contact mechanism. The preceding chapters of this thesis have presented a review of the related existing work, and the design and analysis, fabrication and mechanical testing of the C^3M structures. This chapter will summarize the thesis, discuss the major conclusions drawn from the work, and present the contributions made and possible future work.

5.1 Summary and Conclusions

First, different cellular structures were presented followed by an overview of compliant mechanisms. The manufacturing process, LM-RIF, was reviewed. Work pertaining to the crushing of honeycomb structures for the purpose of energy absorption was also reviewed.

Next, the modeling of the C^3M structure and the formulation of the optimization problem were presented. The straight-walled unit cells were presented and then the process by which the curved-walled cell was created. The geometry of the unit cells were then used to create a finite element model used for analysis. The designs were then used to implement an optimization procedure in order to determine the best possible C^3M structure. The objective function, *E/(H*L)*, was shown, along with the variables to be optimized. The optimization algorithm was presented. The optimization algorithm was used to run two different optimization problems; one with two variables, *h/l* and θ, and one with three variables, *h/l*, θ, and γ.

The bounds for the optimization problem were then selected and explained. A comparison of the cells was presented comparing the cells where the contact mechanism width was constrained by the manufacturing process and where it was held constant at 30% of *h*. Both straight- and curved-walled cells were presented using both the two- and three-variable optimization procedure. It was shown that for the curved-walled cells, a smaller *h/l* and a larger angle, θ, is more beneficial. For the lower input velocities, the curved-walled

cells are more beneficial. When looking at these optimized curved-walled cells, they appeared very similar to the straight-walled cells because of the large angle, θ. For the higher input velocities, the straight-walled cells are more beneficial.

After determining the best possible C^3M designs, the cells were then fabricated. It was found that there were geometric variations in the parts fabricated via LM-RIF, which could be seen in the form of warping, cracks, and inconsistent wall thicknesses which resulted in parts that were not testable. Due to the time required to raster the parts, only four cells were fabricated via laser micro-machining. Finally, the experimental results from mechanical testing of the C^3M structures were presented. The test rig and testing procedure were first introduced. Three different types of C^3M structures were tested. The experimental data was found and there were differences in the measured data and predictions. The discrepancies come from friction during compression testing which resulted in higher measured forces. Although contact occurred in all simulations, it did not occur in all test runs. Out of plane bending was also an issue that arose during testing. The material model used also only has a few data points. If a more extensive material model was known, the simulation result may be much closer.

5.2 Contributions

This work has contributed to the design of cellular materials for use in energy absorption. A novel cellular structure, which has not yet been considered in the literature, was developed that incorporated a contact mechanism to achieve higher energy absorption. Previously in the literature, contact-aided compliant cellular mechanisms and cellular mechanisms for energy absorption have each been presented, however combining these two concepts is a novel approach. Incorporating a contact mechanism into the cell resulted in greater energy absorption in the cell when contact takes place, allowing the cell to absorb more energy than it could without contact. Therefore, the inclusion of both of these concepts into the final design resulted in a novel and improved cellular structure that has provided a substantial improvement in these cases in terms of more energy absorption. Previous work completed in our group also only considered quasi-static loading. A methodology was developed to maximize the energy absorption of the cell. This methodology was

implemented in the form of a computer code that links Matlab and ANSYS to optimize the cell for the maximum energy absorption. The developed computer code was embedded within an optimization routine to find the best C^3M structures. As future compression testing is completed on parts either fabricated using the LM-RIF process or laser micro-machining, the material model within the FEA simulation can be updated as more information is known and the simulations re-run. The test set-up built by our collaborators can be used for the compression testing of a variety of parts including the future C^3M structures and theta specimens. Refinishing the Teflon face of the test rig and lubricating contact between the compression plate and the guide rails can reduce friction in the test set-up.

5.3 Recommendations for Future Work

There are many ways that this work can be continued or further developed in the future. It would be beneficial to further analyze the C^3M structures for energy absorbing structures. In this study, only one contact mechanism design was considered for the cellular structure, therefore it may be beneficial to broaden the study by including other contact mechanism structures. Additionally, it may be beneficial to try different contact mechanism locations and geometries. One example can be seen in Figure 5.1. It could be interesting to try to create a contact mechanism with multiple contact points or a rolling contact mechanism. On example of a cell with multiple contact points can be seen in Figure 5.2. The designs in Figures 5.1 and 5.2 were initially proposed as a design for stress relief. These cells could potentially be used to absorb energy. Additionally, it could be useful to look into different contact mechanism locations, instead of the simple single vertical contact mechanism, which is perpendicular to the direction of crushing, used in this thesis. It may be possible to achieve more energy absorption if a different configuration were used. Finally, determining the flexural stiffness of the cells could be useful, in order to determine how effective this structure will perform as a sandwich structure. This study could provide a better idea of what a desirable out-of-plane thickness of the cellular structure would be, due to the fact that a thicker specimen would have a higher stiffness.

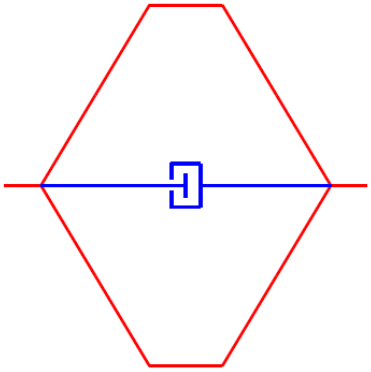

Figure 5.1: Potential design for a honeycomb structure with a different contact location and design [11]

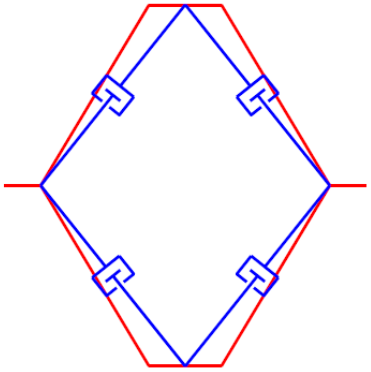

Figure 5.2: Potential design for a honeycomb structure with multiple contact points [11]

The final application of the C^3M structure dramatically determines the input parameters for the optimization problem. Once the design parameters are known, the inputs to the algorithm can be altered. The algorithm that was developed can be used for larger input velocities over the same time or over a smaller time. The material model can also be changed along with the bounds for the variables that define the cells. The addition of friction should also be added to the model to account for any sliding within the contact mechanism. The use of friction would cause of more energy to be dissipated.

In this thesis, the C^3M structures were only fabricated from 254 micron thick stainless steel shims using laser micro-machining. Laser micro-machining allows for parts to be fabricated that are much smaller than those fabricated via the LM-RIF process. This allows for cells with smaller features as seen in Figure 5.3. The bottom cell is one that was tested in Chapter 4. The other cell and the array are much smaller and all features surrounding the contact mechanism are still intact. The limit on the contact mechanism width does not need to be enforced if laser micro-machining is the only method of fabrication. Laser micro-machining also allows for other configurations to be fabricated. Laser micro-machining has different constraints in terms of the feature sizes and contact gap. These constraints could be added to allow for more complex geometries with smaller feature sizes to be fabricated. Figure 5.4 shows four cells that were cut out of aluminum foil, approximately 25 microns thick, then bent up to a 90° angle. With a more powerful laser, these three-dimensional structures could be cut out of a stainless steel shim and then used to create a sandwich structure. These sandwich structures can then be tested.

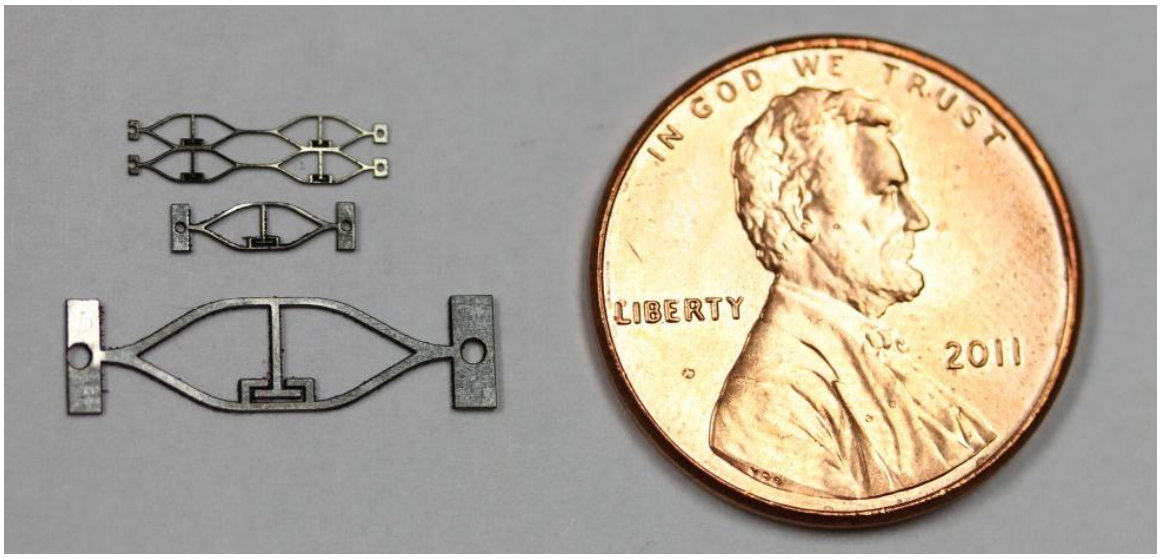

Figure 5.3: A cellular array, a single cell and a full scale single cell all fabricated via the raster method.

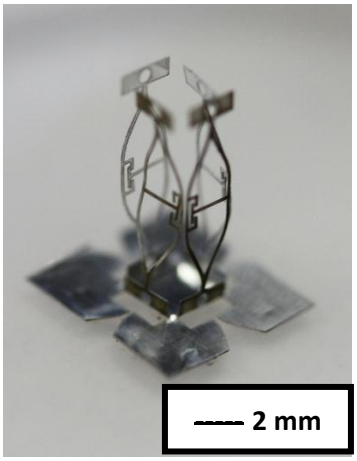

Figure 5.4: Four cells cut out of aluminum foil then bent up to a 90° angle.

Finally, it would be advantageous to investigate other potential uses for these energy absorbing C^3M structures. Although the original design was intended as a component for a crushing, cellular structures find many uses and could be beneficial in many other areas as well. Because the stainless steel and zirconia materials are biocompatible, it may be useful to investigate biomedical applications for these structures. One potential biomedical application could involve taking an array of these structures, and using the contact to determine the stiffness of the material it is pressed against. Other potential uses for these C^3M structures could include applications involving energy harvesting.

Appendix A: Node Location Results

This appendix presents the stress distribution images for different node locations in Chapter 2. Each image shows the plots for each node location from ANSYS. The plots correspond to the node locations found in Figure 2.7 and reproduced here as Figure A.1. The maximum stress was always located at the first node which is indicated by the square, found in Figure A.4. The stress at this node was used to define σ in the optimization problem.

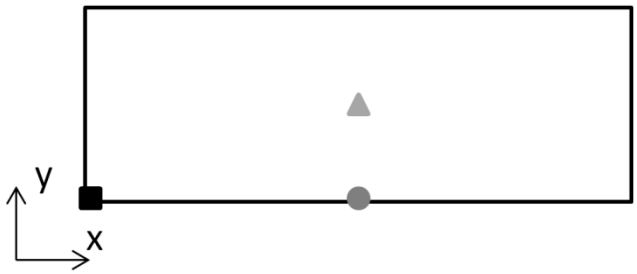

Figure A.1: Location of Beam Element Nodes Used Reproduced from Figure 2.7

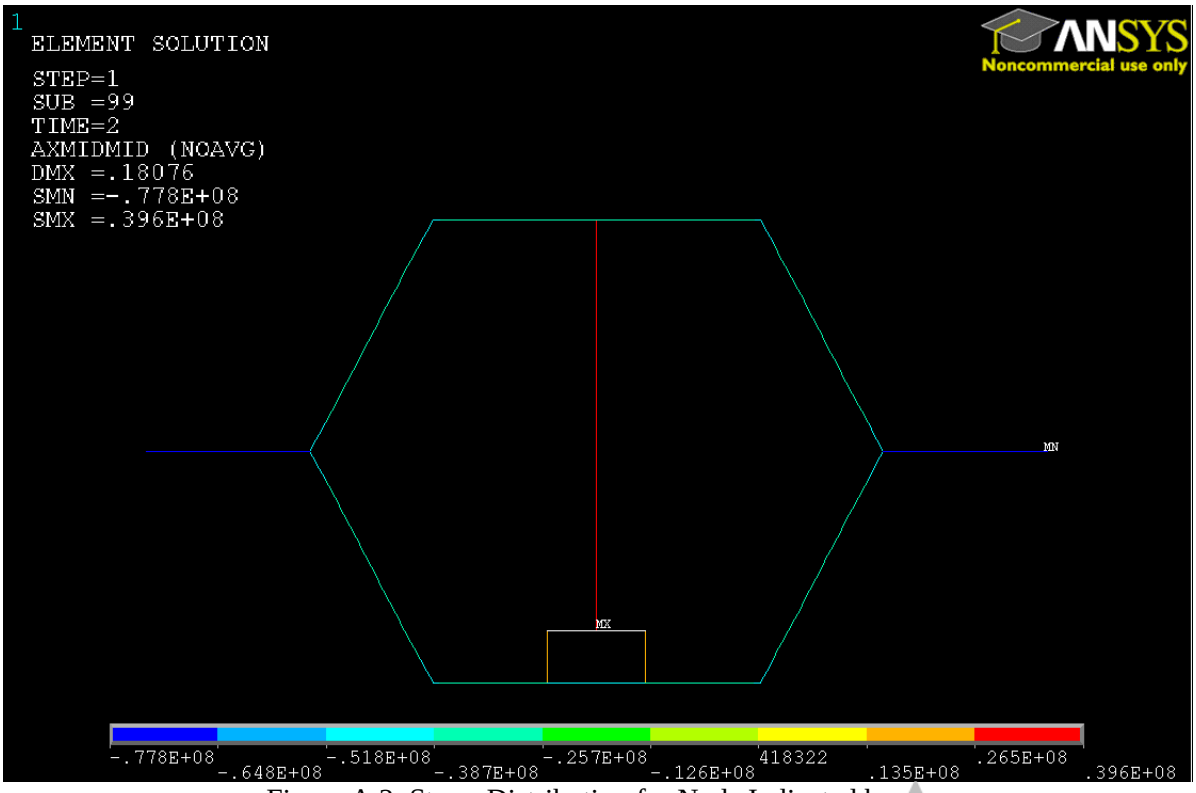

Figure A.2: Stress Distribution for Node Indicated by

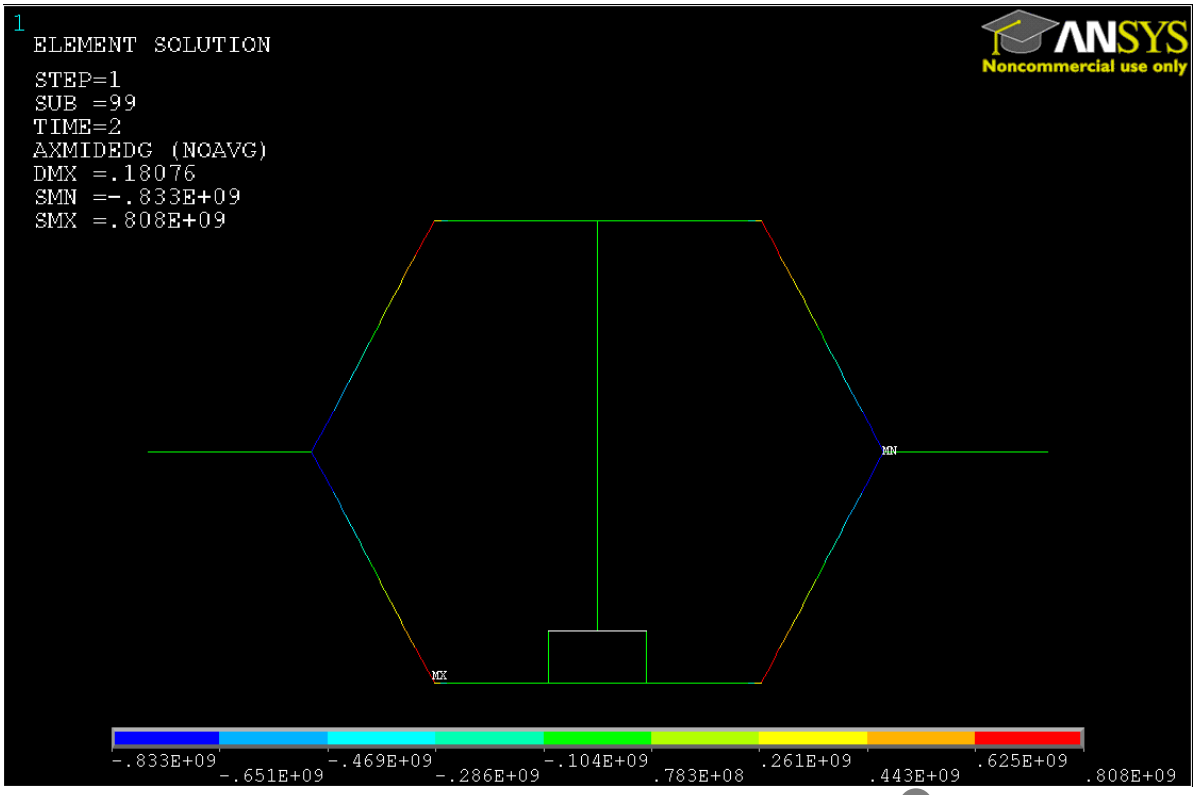

Figure A.3: Stress Distribution for Node Indicated by ●

Figure A.4: Stress Distribution for Node Indicated by ■

Appendix B: Computer Codes

The codes below were used to run the optimization algorithms.

Two-Variable Optimization Algorithm

Used for each starting point for a two-variable optimization problem indicating the value for h/l, and θ.

```
global fid
delete('0.4, -80inpt.txt');
fid = fopen('0.4, -80inpt.txt','w');
[fval] = calcinpt( 0.4, -80*pi/180)
fclose(fid)


function [fval] = calcinpt(x1, x2)
format long
x0 = [x1; x2];
lb = [0.65; -80*pi/180];
ub = [1.5; 0];
global i
i=1;
options = optimset('Algorithm','interior-point','Hessian','bfgs', 'TolCon', 1e-2,
'TolFun', 1e-2, 'TolX', 1e-2,'AlwaysHonorConstraints', 'bounds');
[x,fval,exitflag]=fmincon(@coninptobjfunc,x0,[],[],[],[],lb,ub,[],options)

function [f] = coninptobjfuncpbs (x)
global i

% User Defined Variables
d=.4;
stresslimit = 832000000;
allstrain = .006;
E=200e9;
Poisson=0.3;
toverperim=0.015;

format long

% 1 = straight wall contact
% 2 = straight wall non-contact
% 3 = curved wall contact
% 4 = curved wall non-contact
celltype = 1
```

```
%open text file (do at very start of script)
hoverl=x(2)
theta=x(1); %positive for auxetic based, negative for honeycomb based
contactgap=.09;
input = -0.15;
inputtime = 2;

l=4;
h=hoverl*l;
Len=2*h-2*l*sin(theta);
Hei=2*l*cos(theta);
HL = Len*Hei;
perim=Len+Hei;
FP = Len*Hei;
t=0.3;
tcon=t;
ttop=t;
d=0.254;

allstrain=0.00335;
E=193e9;
Poisson=0.3;
i = 1;

CM=2.42/h
r = tan((3.14/2-theta)/2)*(1-CM)*(h/2)


inputvect = [1;input];
save /gpfs/home/jeh5096/inputvect.txt inputvect -ascii

CMvect=[1;CM];
save /gpfs/home/jeh5096/CMvect.txt CMvect -ascii

contactgapvect=[1;contactgap];
save /gpfs/home/jeh5096/contactgapvect.txt contactgapvect -ascii


if celltype == 1 %straight wall contact
   % Export variables to text file
   vars=[(1:1:10)',[l; h; t; tcon; ttop; d; theta; allstrain; E; Poisson, inputtime]];
   save /gpfs/home/jeh5096/vars.txt vars –ascii
!ansys130 < /gpfs/home/jeh5096/swcontact.txt > gpfs/home/jeh5096/ /results.txt
!rm file.*
```

```
elseif celltype == 2 %straight wall non-contact
   % Export variables to text file
   vars=[(1:1:10)',[l; h; t; tcon; ttop; d; theta; allstrain; E; Poisson, inputtime]];
   save /gpfs/home/jeh5096/vars.txt vars –ascii
!ansys130 < /gpfs/home/jeh5096/swnoncontact.txt > gpfs/home/jeh5096/ /results.txt
!rm file.*


elseif celltype == 3 %curved wall contact
   % Export variables to text file
   vars=[(1:1:11)',[l; h; t; tcon; ttop; d; theta; r; allstrain; E; Poisson, inputtime]];
   save /gpfs/home/jeh5096/vars.txt vars –ascii
!ansys130 < /gpfs/home/jeh5096/cwcontact.txt > gpfs/home/jeh5096/ /results.txt
!rm file.*


elseif celltype == 4 %curved wall non-contact
   % Export variables to text file
   vars=[(1:1:11)',[l; h; t; tcon; ttop; d; theta; r; allstrain; E; Poisson, inputtime]];
   save /gpfs/home/jeh5096/vars.txt vars –ascii
!ansys130 < /gpfs/home/jeh5096/cwnoncontact.txt > gpfs/home/jeh5096/ /results.txt
!rm file.*


else
   fprintf('Not Valid Cell Type')
end

strain_new = load('/gpfs/home/jeh5096/work/cw1/tot_strain_max.txt')
stressmax = load('/gpfs/home/jeh5096/work/cw1/stress_max.txt')
sumenergy = load('/gpfs/home/jeh5096/work/cw1/sumenergy.txt');
vertdisp = load('/gpfs/home/jeh5096/work/cw1/max_vert_disp.txt');

if ((stressmax>stresslimit) ||(stressmax == 0))
   stressmax = -1000;
   sumenergy = -10000;
end

EHL = sumenergy/(HL)

%output all to a text file for post processing
outputThis = [x(1), x(2), EHL, sumenergy, HL, stressmax, vertdisp];

%output new line of data
fprintf(fid,'%f, \t', outputThis);
```

```
%leave a space after last family:
space = [0];
fprintf(fid,'%f, \n',space);


f=-EHL;
```

Three-variable Optimization Algorithm

Used for each starting point for a three-variable optimization problem indicating the value for h/l, θ, and γ.

```
global fid
delete('0.4, -80inpt, 0.08.txt');
fid = fopen('0.4, -80inpt, 0.08.txt','w');
[fval] = calcinpt( 0.4, -80*pi/180, 0.08)
fclose(fid)


function [fval] = calcinpt(x1, x2,x3)
format long
x0 = [x1; x2;x3];
lb = [0.65; -80*pi/180;0.08];
ub = [1.5; 0;0.25];
global i
i=1;
options = optimset('Algorithm','interior-point','Hessian','bfgs', 'TolCon', 1e-2,
'TolFun', 1e-2, 'TolX', 1e-2,'AlwaysHonorConstraints', 'bounds');
[x,fval,exitflag]=fmincon(@coninptobjfunc,x0,[],[],[],[],lb,ub,[],options)

function [f] = coninptobjfuncpbs (x)
global i

% User Defined Variables
d=.4;
stresslimit = 832000000;
allstrain = .006;
E=200e9;
Poisson=0.3;
toverperim=0.015;

format long

% 1 = straight wall contact
% 2 = straight wall non-contact
```

```
% 3 = curved wall contact
% 4 = curved wall non-contact
celltype = 1

%open text file (do at very start of script)
hoverl=x(2)
theta=x(1); %positive for auxetic based, negative for honeycomb based
contactgap=x(3);
input = -0.15;
inputtime = 2;

l=4;
h=hoverl*l;
Len=2*h-2*l*sin(theta);
Hei=2*l*cos(theta);
HL = Len*Hei;
perim=Len+Hei;
FP = Len*Hei;
t=0.3;
tcon=t;
ttop=t;
d=0.254;

allstrain=0.00335;
E=193e9;
Poisson=0.3;
i = 1;

CM=2.42/h
r = tan((3.14/2-theta)/2)*(1-CM)*(h/2)

inputvect = [1;input];
save /gpfs/home/jeh5096/inputvect.txt inputvect -ascii

CMvect=[1;CM];
save /gpfs/home/jeh5096/CMvect.txt CMvect -ascii

contactgapvect=[1;contactgap];
save /gpfs/home/jeh5096/contactgapvect.txt contactgapvect -ascii

if celltype == 1 %straight wall contact
   % Export variables to text file
   vars=[(1:1:10)',[l; h; t; tcon; ttop; d; theta; allstrain; E; Poisson, inputtime]];
   save /gpfs/home/jeh5096/vars.txt vars –ascii
!ansys130 < /gpfs/home/jeh5096/swcontact.txt > gpfs/home/jeh5096/ /results.txt
!rm file.*
```

```
elseif celltype == 2 %straight wall non-contact
   % Export variables to text file
   vars=[(1:1:10)',[l; h; t; tcon; ttop; d; theta; allstrain; E; Poisson, inputtime]];
   save /gpfs/home/jeh5096/vars.txt vars –ascii
!ansys130 < /gpfs/home/jeh5096/swnoncontact.txt > gpfs/home/jeh5096/ /results.txt
!rm file.*


elseif celltype == 3 %curved wall contact
   % Export variables to text file
   vars=[(1:1:11)',[l; h; t; tcon; ttop; d; theta; r; allstrain; E; Poisson, inputtime]];
   save /gpfs/home/jeh5096/vars.txt vars –ascii
!ansys130 < /gpfs/home/jeh5096/cwcontact.txt > gpfs/home/jeh5096/ /results.txt
!rm file.*


elseif celltype == 4 %curved wall non-contact
      % Export variables to text file
   vars=[(1:1:11)',[l; h; t; tcon; ttop; d; theta; r; allstrain; E; Poisson, inputtime]];
   save /gpfs/home/jeh5096/vars.txt vars –ascii
!ansys130 < /gpfs/home/jeh5096/cwnoncontact.txt > gpfs/home/jeh5096/ /results.txt
!rm file.*


else
   fprintf('Not Valid Cell Type')
end

strain_new = load('/gpfs/home/jeh5096/work/cw1/tot_strain_max.txt')
stressmax = load('/gpfs/home/jeh5096/work/cw1/stress_max.txt')
sumenergy = load('/gpfs/home/jeh5096/work/cw1/sumenergy.txt');
vertdisp = load('/gpfs/home/jeh5096/work/cw1/max_vert_disp.txt');

if ((stressmax>stresslimit) ||(stressmax == 0))
   stressmax = -1000;
   sumenergy = -10000;
end

EHL = sumenergy/(HL)

%output all to a text file for post processing
outputThis = [x(1), x(2), x(3),EHL, sumenergy, HL, stressmax, vertdisp];

%output new line of data
```

```
fprintf(fid,'%f, \t', outputThis);

%leave a space after last family:
space = [0];
fprintf(fid,'%f, \n',space);


f=-EHL;
```

The MATLAB code below is used to store the variable used to run the ANSYS simulations manually.

```
% 1 = straight wall contact
% 2 = straight wall non-contact
% 3 = curved wall contact
% 4 = curved wall non-contact
celltype = 1

%open text file (do at very start of script)
delete('data.txt');
fid = fopen('data.txt','a');
hoverl=.65
theta=-80*pi()/180; %positive for auxetic based, negative for honeycomb based
contactgap=.09;
input = -0.15;
inputtime = 2;

l=4;
h=hoverl*l;
Len=2*h-2*l*sin(theta);
Hei=2*l*cos(theta);
HL = Len*Hei;
perim=Len+Hei;
FP = Len*Hei;
t=0.3;
tcon=t;
ttop=t;
d=0.254;

allstrain=0.00335;
E=193e9;
Poisson=0.3;
i = 1;
```

```
CM=2.42/h
r = tan((3.14/2-theta)/2)*(1-CM)*(h/2)


if celltype == 1 %straight wall contact
   % Export variables to text file
   vars=[(1:1:10)',[l; h; t; tcon; ttop; d; theta; allstrain; E; Poisson, inputtime]];
   save /gpfs/home/jeh5096/vars.txt vars -ascii

elseif celltype == 2 %straight wall non-contact
   % Export variables to text file
   vars=[(1:1:10)',[l; h; t; tcon; ttop; d; theta; allstrain; E; Poisson, inputtime]];
   save /gpfs/home/jeh5096/vars.txt vars -ascii

elseif celltype == 3 %curved wall contact
   %calc_filletsize;
   % Export variables to text file
   vars=[(1:1:11)',[l; h; t; tcon; ttop; d; theta; r; allstrain; E; Poisson, inputtime]];
   save /gpfs/home/jeh5096/vars.txt vars -ascii

elseif celltype == 4 %curved wall non-contact
   %calc_filletsize;
   % Export variables to text file
   vars=[(1:1:11)',[l; h; t; tcon; ttop; d; theta; r; allstrain; E; Poisson, inputtime]];
   save /gpfs/home/jeh5096/vars.txt vars -ascii

else
   fprintf('Not Valid Cell Type')
end

inputvect = [1;input];
save /gpfs/home/jeh5096/inputvect.txt inputvect -ascii

CMvect=[1;CM];
save /gpfs/home/jeh5096/CMvect.txt CMvect -ascii

contactgapvect=[1;contactgap];
save /gpfs/home/jeh5096/contactgapvect.txt contactgapvect -ascii
```

The code below is read into ANSYS to build the geometry and run the simulations. Because there is a difference in the way in which the cells are built, there are two different ANSYS files, one for straight-walled cells and one for curved-walled cells, were used. After the geometry is built, the remaining code is identical. Below are both codes. The code in

bold is used to build the straight-walled geometry. The code in italics is used to build the curved-walled geometry. The code that is neither bolded or italicized is used after the code used to build the geometry. The code that is underlined creates the contact surfaces. If a non-contact cell is desired, this section of code can be removed.

```
finish
/clear,nostart
y

/CWD,/gpfs/home/jeh5096
/FILNAME,swcontact,0
/CONFIG,NRES,100000
/PLOPTS,DATE,0
/triad,off
/PREP7


*DIM,vars,table,11,1,1
vars(0,1)=1
*TREAD,vars,/gpfs/home/jeh5096/vars,txt

l=vars(1,1)
h=vars(2,1)
t=vars(3,1)
tcon=vars(4,1)
ttop=vars(5,1)
w=vars(6,1)
theta=vars(7,1)
allstrain=vars(8,1)
E=vars(9,1)
Poisson=vars(10,1)
inputtime=vars(11,1)

*DIM,inputvect,table,1,1,1
inputvect(0,1)=1
*TREAD,inputvect,/gpfs/home/jeh5096/inputvect,txt
input=inputvect(1,1)

*DIM,contactgapvect,table,1,1,1
contactgapvect(0,1)=1
*TREAD,contactgapvect,/gpfs/home/jeh5096/contactgapvect,txt
contactgap=contactgapvect(1,1)

*DIM,CMvect,table,1,1,1
```

```
CMvect(0,1)=1
*TREAD,CMvect,/gpfs/home/jeh5096/CMvect,txt
CM=CMvect(1,1)

CMmult=CM/2
conh=2*l*cos(theta)
relconw=h
Len=2*h-2*l*sin(theta)

ET,1,BEAM23
KEYOPT,1,6,0
r,1,t*w,w*t**3/12,t
r,2,tcon*w,w*tcon**3/12,tcon
r,3,ttop*w,w*ttop**3/12,ttop

MP,EX,1,E
MP,PRXY,1,Poisson
MP,DENS,1,7990

TB,KINH,1,1,3,

TBPT,,.001,193e6
TBPT,,.003535,307.5063e6
TBPT,,.0510425,661.8969e6

k,1,0,0,0
k,2,h,0,0
k,3,h-l*sin(theta),l*cos(theta),0
k,4,h,2*l*cos(theta),0
k,5,0,l*2*cos(theta),0
k,6,l*sin(theta),l*cos(theta),0
k,7,l*sin(theta)-h/10,l*cos(theta),0
k,8,h+(h/10-l*sin(theta)),l*cos(theta),0

k,9,relconw/2,conh,0
k,10,relconw/2,conh/10+contactgap,0
k,11,relconw/2,conh/10,0
k,12,relconw/2-h*CMmult,conh/10,0
k,13,relconw/2+h*CMmult,conh/10,0
k,14,relconw/2+h*CMmult,0,0
k,15,relconw/2-h*CMmult,0,0
k,16,relconw/2+h*CMmult,conh/10+contactgap,0
k,17,relconw/2-h*CMmult,conh/10+contactgap,0
k,18,relconw/2,conh/10+contactgap,0

l,1,15
```

l,15,14
l,14,2
l,2,3
l,3,4
l,4,9
l,9,5
l,5,6
l,6,1
l,3,8
l,6,7

l,9,10
l,11,10
l,12,11
l,11,13
l,14,16
l,17,15
l,16,18
l,18,17

finish
/clear,nostart
y

/CWD,/gpfs/home/jeh5096
/FILNAME,cwcontactjen,0
/CONFIG,NRES,50000
/PLOPTS,DATE,0
/triad,off
/PREP7

**DIM,vars,table,12,1,1*
vars(0,1)=1
**TREAD,vars,/gpfs/home/jeh5096/vars,txt*

l=vars(1,1)
h=vars(2,1)
t=vars(3,1)
tcon=vars(4,1)
ttop=vars(5,1)
d=vars(6,1)
theta=vars(7,1)
fillet=vars(8,1)
allstrain=vars(9,1)
E=vars(10,1)

```
Poisson=vars(11,1)
inputtime=vars(12,1)

*DIM,inputvect,table,1,1,1
inputvect(0,1)=1
*TREAD,inputvect,/gpfs/home/jeh5096/inputvect,txt
input=inputvect(1,1)

*DIM,contactgapvect,table,1,1,1
contactgapvect(0,1)=1
*TREAD,contactgapvect,/gpfs/home/jeh5096/contactgapvect,txt
contactgap=contactgapvect(1,1)

*DIM,cmvect,table,1,1,1
cmvect(0,1)=1
*TREAD,cmvect,/gpfs/home/jeh5096/CMvect,txt
CM=cmvect(1,1)

CMmult=CM/2
conh=2*l*cos(theta)
relconw=h
Len=2*h-2*l*sin(theta)

ET,1,BEAM23
KEYOPT,1,6,0
r,1,t*w,w*t**3/12,t
r,2,tcon*w,w*tcon**3/12,tcon
r,3,ttop*w,w*ttop**3/12,ttop

MP,EX,1,E
MP,PRXY,1,Poisson
MP,DENS,1,7990


TB,KINH,1,1,3,
TBPT,,.001,193e6
TBPT,,.003535,307.5063e6
TBPT,,.0510425,661.8969e6

k,1,0,0,0
k,2,h,0,0
k,3,h-l*sin(theta),l*cos(theta),0
k,4,h,2*l*cos(theta),0
k,5,0,l*2*cos(theta),0
k,6,l*sin(theta),l*cos(theta),0
k,7,l*sin(theta)-h/2,l*cos(theta),0
```

*k,8,h+(h/2-l*sin(theta)),l*cos(theta),0*

k,9,relconw/2,conh,0
k,10,relconw/2,conh/10+contactgap,0
k,11,relconw/2,conh/10,0
*k,12,relconw/2-h*CMmult,conh/10,0*
*k,13,relconw/2+h*CMmult,conh/10,0*
*k,14,relconw/2+h*CMmult,0,0*
*k,15,relconw/2-h*CMmult,0,0*
*k,16,relconw/2+h*CMmult,conh/10+contactgap,0*
*k,17,relconw/2-h*CMmult,conh/10+contactgap,0*
k,18,relconw/2,conh/10+contactgap,0

l,1,15
l,15,14
l,14,2
l,2,3
l,3,4
l,4,9
l,9,5
l,5,6
l,6,1
l,3,8
l,6,7
l,9,10
l,11,10
l,12,11
l,11,13
l,14,16
l,17,15
l,16,18
l,18,17
lfillt,1,9,fillet
lfillt,3,4,fillet
lfillt,7,8,fillet
lfillt,5,6,fillet
lfillt,4,10,fillet
lfillt,11,9,fillet
l,3,8
l,6,7
lfillt,8,27,fillet
lfillt,5,26,fillet

TYPE, 1
MAT, 1

```
REAL,      1
ESYS,      0
SECNUM,
ESIZE,0.1,0,
FLST,2,12,4,ORDE,8
FITEM,2,3
FITEM,2,4
FITEM,2,7
FITEM,2,8
FITEM,2,11
FITEM,2,-16
FITEM,2,19
FITEM,2,20
LMESH,P51X

TYPE,   1
MAT,      1
REAL,      2
ESYS,      0
SECNUM,
ESIZE,0.1,0,
FLST,2,11,4,ORDE,4
FITEM,2,17
FITEM,2,18
FITEM,2,21
FITEM,2,-29
LMESH,P51X

TYPE,   1
MAT,      1
REAL,      3
ESYS,      0
SECNUM,
ESIZE,0.1,0,
FLST,2,6,4,ORDE,6
FITEM,2,1
FITEM,2,2
FITEM,2,5
FITEM,2,6
FITEM,2,9
FITEM,2,10
LMESH,P51X


/COM, CONTACT PAIR CREATION - START
ET,2,169
```

```
ET,3,172
KEYOPT,3,5,0
KEYOPT,3,9,1
KEYOPT,3,10,2
KEYOPT,3,11,0
KEYOPT,3,12,1
R,99
REAL,99
R,99,,,,0.001
MP,MU,1,1

! Generate the target surface
LSEL,S,,,18
LSEL,A,,,19
TYPE,2
NSLL,S,1
ESLN,S,0
ESURF

! Generate the contact surface
LSEL,S,,,14
LSEL,A,,,15
TYPE,3
NSLL,S,1
ESLN,S,0
ESURF
TYPE,1
REAL,1
ALLSEL,ALL
!Contact Done


!LSEL,S,line, ,       6,7
!NSLL,S,1
!CP,1,UY,ALL
!ALLSEL,ALL

LSEL,S,line, ,       1,3
NSLL,S,1
CP,2,UY,ALL
ALLSEL,ALL

FLST,2,1,4,ORDE,1
FITEM,2,2
!*
/GO
```

```
DL,P51X, ,UY,0

FLST,2,1,3,ORDE,1
FITEM,2,7
!*
/GO
DK,P51X, ,0, ,0,UX,

FLST,2,1,3,ORDE,1
FITEM,2,8
!*
/GO
DK,P51X, ,input, ,0,UX, , , , , ,

ALLSEL,ALL
/SOL
ANTYPE,4
NLGEOM,1
DELTIM,0.05,,
OUTRES,ALL,ALL
kbc,0
TIME,inputtime
nropt,unsym

FINISH
allsel,all
/SOL
/REPLOT,RESIZE
/STATUS,SOLU
SOLVE

/POST1
/DSCALE,ALL,1.0
/post1
ETABLE,senergy,SENE,
ETABLE,kenergy,KENE,
etable,axstress,ls,1
!etable,estress,nlin,1
!etable,equplastrain,nlin,4 !equ
etable,axplastrain,leppl,1 !axial
etable,axelastrain,lepel,1
etable,ydisp,U,Y
etable,xdisp,U,X
etable,volu,volu
SADD,totstrain,AXPLASTR,AXELASTR,1,1,0,
```

```
esort,etab,axstress,0,0
*get,stress_max,sort,0,max
*cfopen,/gpfs/home/jeh5096/stress_max,txt
*vwrite,stress_max
(1x, e16.8)

esort,etab,axplastrain,0,0
*get,ax_strain_max,sort,0,max
*cfopen,/gpfs/home/jeh5096/ax_strain_max,txt
*vwrite,ax_strain_max
(1x, e16.8)

esort,etab,axelastrain,0,0
*get,elas_strain_max,sort,0,max
*cfopen,/gpfs/home/jeh5096/elas_strain_max,txt
*vwrite,elas_strain_max
(1x, e16.8)

esort,etab,totstrain,0,0
*get,tot_strain_max,sort,0,max
*cfopen,/gpfs/home/jeh5096/tot_strain_max,txt
*vwrite,tot_strain_max
(1x, e16.8)

esort,etab,kenergy,0,0
*get,kenergy_max,sort,0,max
*cfopen,/gpfs/home/jeh5096/kenergy_max,txt
*vwrite,kenergy_max
(1x, e16.8)

esort,etab,senergy,0,0
*get,senergy_max,sort,0,max
*cfopen,/gpfs/home/jeh5096/senergy_max,txt
*vwrite,senergy_max
(1x, e16.8)

SSUM
*get,sumenergy,ssum,,item,senergy
*cfopen,/gpfs/home/jeh5096/sumenergy,txt
*vwrite,sumenergy
(1x, e16.8)

SSUM
*get,sumvolu,ssum,,item,volu
*cfopen,/gpfs/home/jeh5096/sumvolu,txt
*vwrite,sumvolu
```

```
(1x, e16.8)

LSEL,S,LINE,,14,15
esll,s
etable,ydisp,U,Y
esort,etab,ydisp,0,1
*get,max_vert_disp,sort,0,max
*cfopen,/gpfs/home/jeh5096/max_vert_disp,txt
*vwrite,max_vert_disp
(1x, e16.8)

allsel,all

*cfclos
```

Appendix C: Metal Shims Material Testing Report

This appendix presents the material test report that states the specifications for the stainless steel plates that were used to fabricate the parts with the laser. The information found on this material testing report was used to create the stress-strain curve found in Section 4.7.

Zapp Precision Strip, Inc. 12633 Clark Street, Santa Fe Springs, CA 90670

MAUDLIN & SON MFG. CO, INC.
1929 HWY 146
KEMAH TX 77565

Zapp Precision Strip, Inc.
12633 Clark Street
Santa Fe Springs, California
90670
Phone+1 562-944-5484
Fax+1 562-944-1874
Tollfree 888-236-0004
www.zapp.com

Member of the Zapp Group

February 09, 2012

Inspection certificate Type 3.1 per EN 10204:2004

Certificate No.	**2210031653000010 01**
Your purchase Order	0087815 dated 02/03/2012
Sales Order	2302018902 Delivery Note 2210031653
Production Lot	2674041 Inspection Lot 020000238885
Item 10	STAINLESS STEEL
Grade / Alloy	SS316/316L
Dimensions	0.0100 " X 24.0000 "
Thickness tolerance	-0.00050 " / 0.00050 "
Width tolerance	0.00000 " / 0.06250 "
Conditions	ANN
Surface	BA
Edge	slit edges
Cust. Specification	GRAIN SIZE PER ASTM E112
Techn. Specification	AMS 5507 REV. F
Techn. Specification	AMS 5524 REV. K
Techn. Specification	ASTM A240/A240M-11A
Techn. Specification	SA-240/SA-240M
Techn. Specification	DIN EN 10088-2:2005
Specifications	AMS 5507 AMS 5524 ASTM A 240 ASME SA240 DIN EN 10088-2 DIN EN 10088-2 Grain Size per ASTM E112
Material	8800201
Customer part no	SS316-010-24-C
Quantity / Weight	**216.000 LB**

Chemical composition **Heat 7410184**

C (%)	Si (%)	Mn (%)	S (%)	P (%)	Cr (%)
0.019	0.500	1.35	0.0010	0.0280	16.28
Ni (%)	**Mo (%)**	**Cu (%)**	**N (%)**	**Co (%)**	
10.10	2.04	0.250	0.030	0.150	

Melt Source AK Steel - US

Quality inspection results

Tensile Strength	96.0 KSI
.2% Yield Strength	44.6 KSI

Zapp Precision Strip, Inc. 12633 Clark Street, Santa Fe Springs, CA 90670

MAUDLIN & SON MFG. CO, INC.
1929 HWY 146
KEMAH TX 77565

February 09, 2012

Elongation 2"	66.60	%
Hardness	85.0	HRB

Batch DC14252055

This material is melted and produced in the United States and meets the requirements of DFARS 252.225-7008.

Sizes and Quality identification test examined and in order.
Surface visual inspection at finish: without objection
In compliance with the conditions mentioned in the acknowledgement of order.
This certificate signifies that the material meets the appropriate requirements defined in the current revision of the following specifications:
Strip-Products: ISO 9445-1; ISO 9445-2; ASTM A480/480M and DIN EN 10140.
Wire/Bar-Products: ASTM A370; ASTM A555/A555M; ASTM A580/A580M.

This certificate has been issued by computer and is valid without signature.

ZPS / GENE SHELDON (MANAGER TECHNICAL SERVICES) +1 508-998-6300

ZAPP Precision Strip does not use mercury in the testing or production of material.
ZAPP Precision Strip is certified to ISO 9001, AS 9100 and is approved as a manufacturer according to AD2000-MERKBLATT W0 and the Pressure Equipment Directive PED 97/23/EC. To view certificates go to customer information www.zapp.com

Appendix D: Stress Distribution Plots for Testing Simulations

This appendix presents the stress distribution images for the various simulation results presented in Chapter 4.

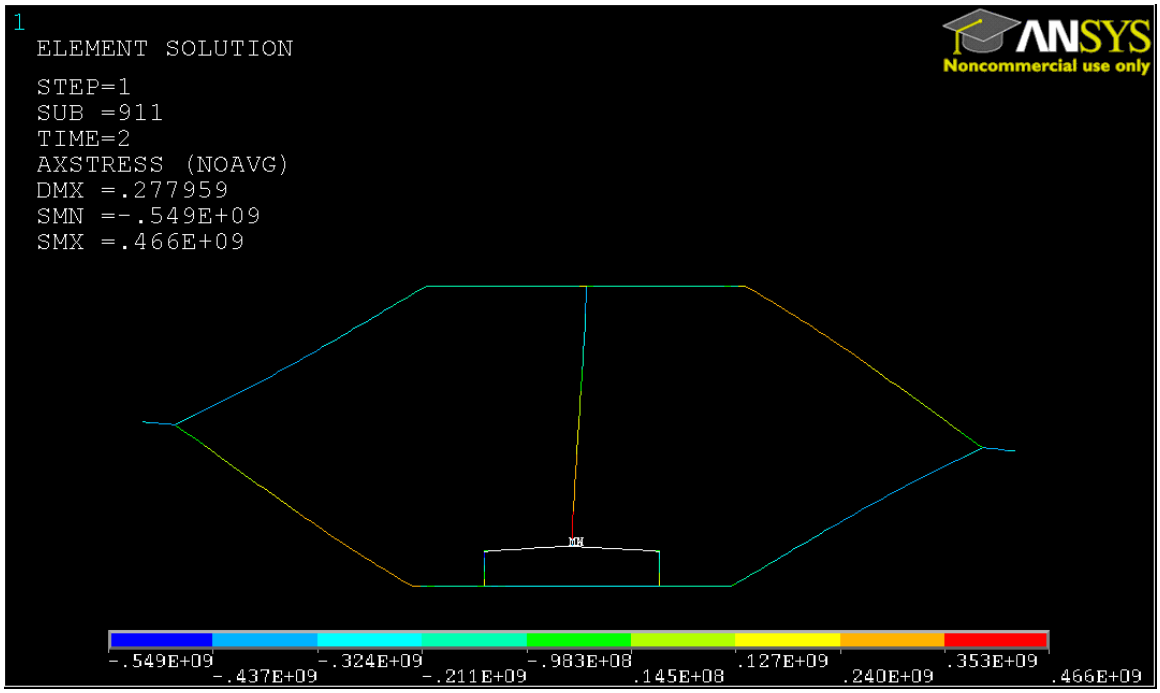

Figure D.1: Stress Distribution for the Straight-wall Comparison Cell Deformed Using an Input Velocity of 75 microns/sec for 2 seconds where the Top and Bottom Walls are Constrained to Represent a Unit Cell

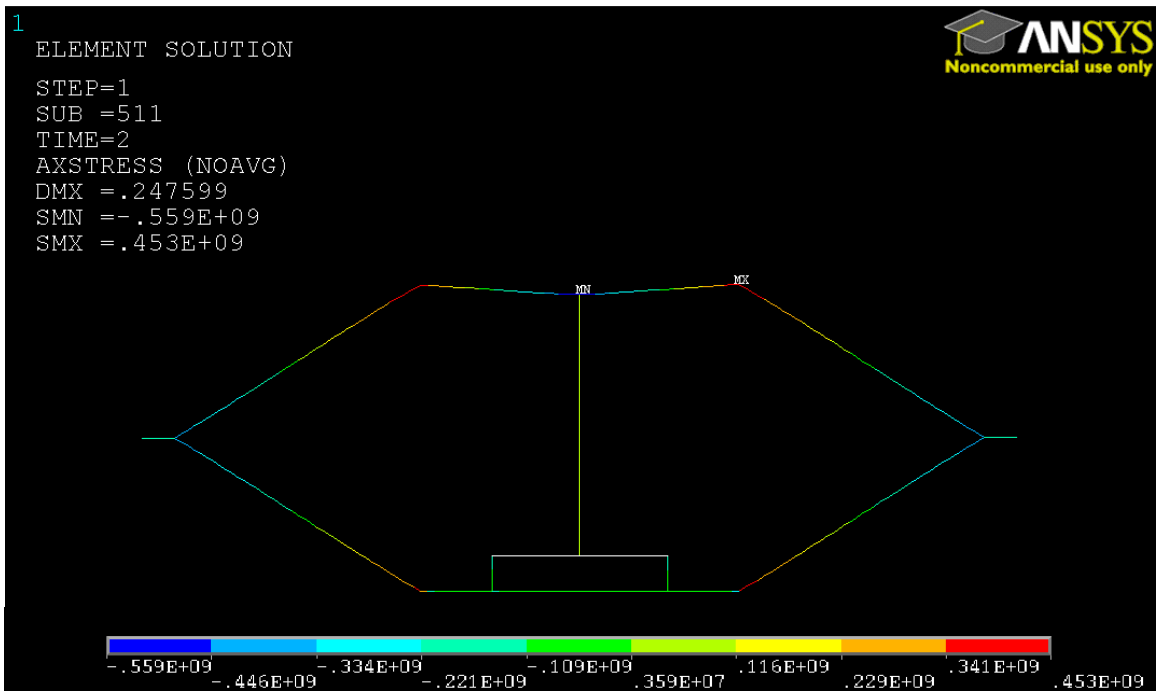

Figure D.2: Stress Distribution for the Straight-wall Comparison Cell Deformed Using an Input Velocity of 75 microns/sec for 2 seconds where the Top Wall is not constrained

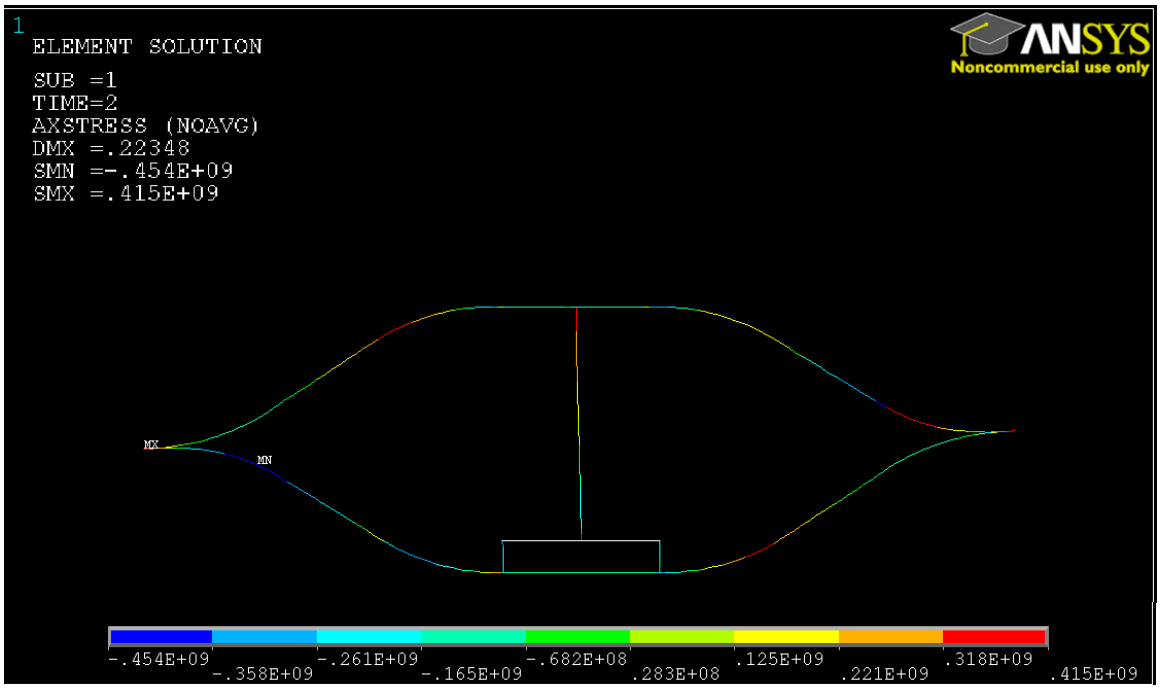

Figure D.3: Stress Distribution for the Curved-wall Comparison Cell Deformed Using an Input Velocity of 60 microns/sec for 2 seconds where the Top and Bottom Walls are constrained to Represent a Unit Cell

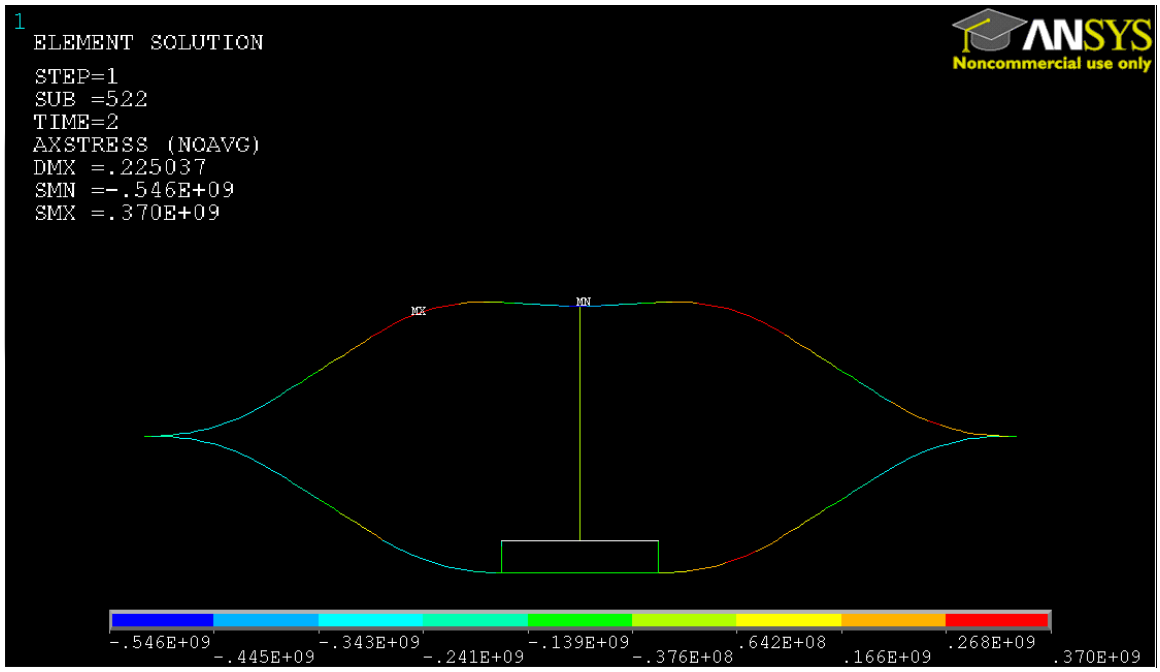

Figure D.4: Stress Distribution for the Curved-wall Comparison Cell Deformed Using an Input Velocity of 60 microns/sec for 2 seconds where the Top Wall is not constrained

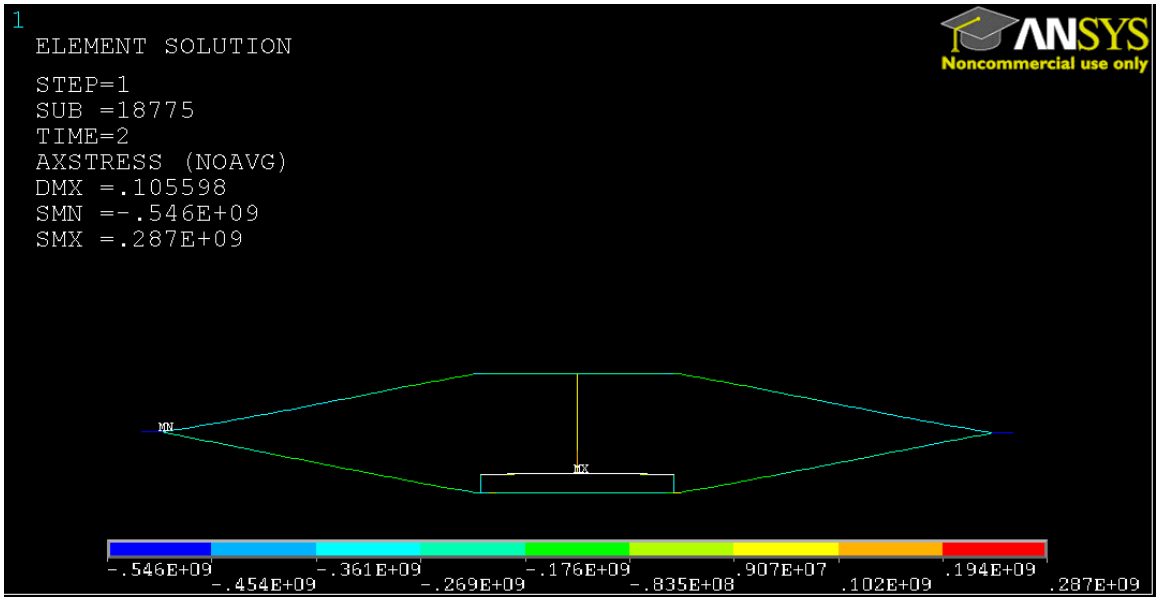

Figure D.5: Stress Distribution for the Optimized Cell Deformed Using an Input Velocity of 30 microns/sec for 2 seconds where the Top and Bottom Walls are constrained to Represent a Unit Cell

Figure D.6: Stress Distribution for Optimized Cell Deformed Using an Input Velocity of 30 microns/sec for 2 seconds where the Top Wall is not constrained

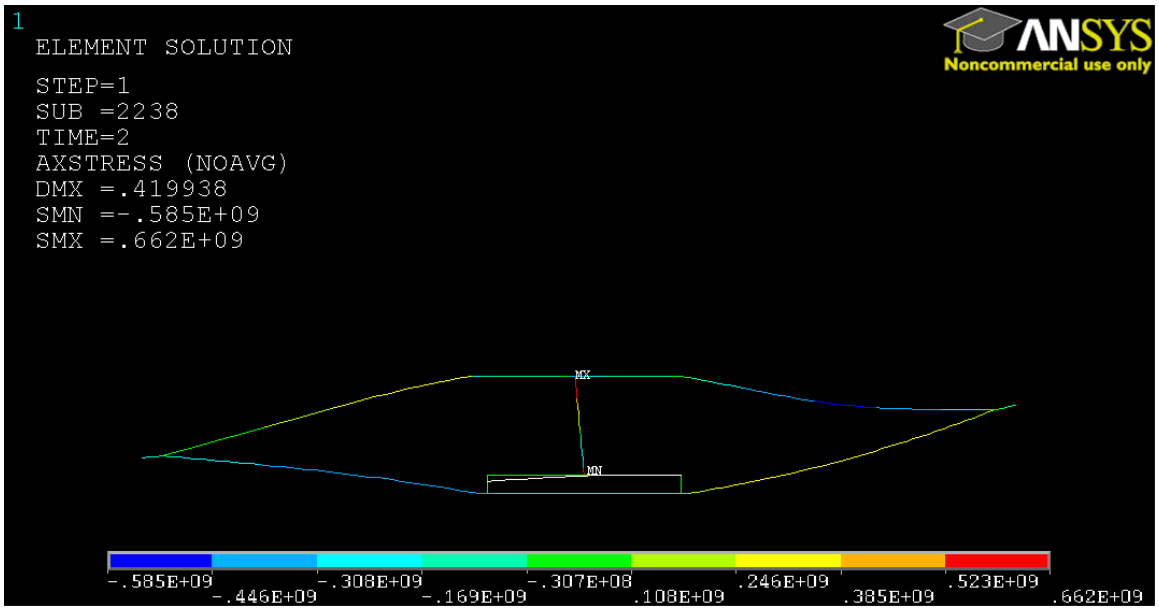

Figure D.7: Stress Distribution for the Optimized Cell Deformed Using an Input Velocity of 50 microns/sec for 2 seconds where the Top and Bottom Walls are constrained to Represent a Unit Cell

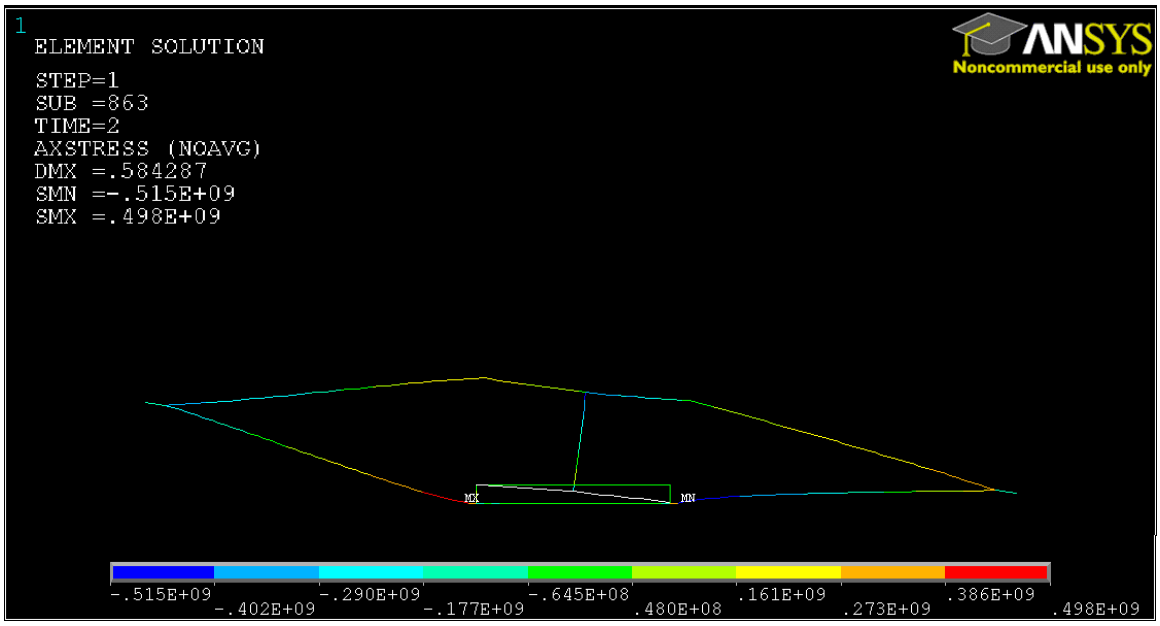

Figure D.8: Stress Distribution for Optimized Cell Deformed Using an Input Velocity of 50 microns/sec for 2 seconds where the Top Wall is not constrained

Bibliography

[1] Gibson, L. J. and Ashby, M. F., 1997, *Cellular Solids - Structures and Properties*, 2 ed. Cambridge University Press.

[2] Henry, C. and McKnight, G., 2006, "Cellular variable stiffness materials for ultra-large reversible deformations in reconfigurable structures," *In Smart Structures and Materials 2006: Active Materials: Behavior and Mechanics* Proc. of SPIE 6170, pp. 1-12.

[3] Olympio, K. R. and Gandhi, F., 2010, "Flexible Skins for Morphing Aircraft Using Cellular Honeycomb Cores," *Journal of Intelligent Material Systems and Structures*, 21(2010), pp. 1719-35.

[4] Shaw, J. A., Grummon, D. S. and Foltz, J., 2007, "Superelastic NiTi honeycombs: fabrication and experiments," *Smart Materials & Structures*, 16(1), pp. 170-178.

[5] Abd El-Sayed, F. K., Jones, R. and Burgess, I. W., 1979, "A theoretical approach to the deformation of honeycomb based composite materials," *Composites*, 10(4), pp. 209-14.

[6] Kim, B. and Christensen, R. M., 2000, "Basic two-dimensional core types for sandwich structures," *International Journal of Mechanical Sciences*, 42(4), 657-676.

[7] Spadoni, A., Ruzzene, M. and Scarpa, F., 2005, "Chiral hexagonal cellular sandwich structures: dynamic response", SPIE - The International Society for Optical Engineering. San Diego, CA, USA, pp. 324-34.

[8] Bubert, E. A., Woods, B. K. S., Kothera, C. S. and Werely, N. M., 2008, "Design and fabrication of a passive 1-D morphing aircraft skin", In 49th AIAA/ASME/ASCE/AHS/ASC Structures, Structural Dynamics and Materials Conference. Schaumburg, IL, pp. 1-13.

[9] Larsen, U. D., Sigmund, O. and Bouwstra, S., 1997, "Design and fabrication of compliant micromechanisms and structures with negative Poisson's ratio," *Journal of Microelectromechanical Systems*, 6(2), 99-106.

[10] Hassan, M. R., Scarpa, F., Ruzzene, M. and Mohammed, N. A., 2008, "Smart shape memory alloy chiral honeycomb," *Materials Science and Engineering a-Structural Materials Properties Microstructure and Processing*, 481, 654-657.

[11] Mehta, V., 2010, "Design, Analysis, and Applications of Cellular Contact-Aided Compliant Mechanisms", Dissertation, The Pennsylvania State University.

[12] Bornengo, D., Scarpa, F. and Remillat, C., 2005, "Evaluation of hexagonal chiral structure for morphing airfoil concept," *Proceedings of the Institution of Mechanical Engineers Part G-Journal of Aerospace Engineering*, 219(G3), pp. 185-192.

[13] Prall, D. and Lakes, R. S., 1997, "Properties of a chiral honeycomb with a Poisson's ratio of -1.," *International Journal of Mechanical Sciences*, 39(3), 305-&.

[14] Grima, J. N., Gatt, R., Ellul, B. and Chetcuti, E., 2010, "Auxetic behavior in non-crystalline materials having star or triangular shaped perforations," *Journal of Non-Crystalline Solids*, 356(37-40), pp. 1980-1987.

[15] Foo, C. C., Chai, G. B. and Seah, L. K., 2007, "Mechanical properties of Nomex material and Nomex honeycomb structure," *Composite Structures*, 80(4), 588-594.

[16] Gibson, L. J., Ashby, M. F. and Harley, B. A., 2010, *Cellular Materials in Nature and Medicine*, Cambridge University Press.

[17] Scarpa, F. and Tomlinson, G., 1999, "Theoretical characteristics of the vibration of sandwich plates with in-plane negative Poisson's ratio values," *Journal of Sound and Vibration*, 230(1), 45-67.

[18] Olympio, K. R. and Gandhi, F., 2007, "Zero Poisson's Ratio Cellular Honeycombs for Flex Skins Undergoing One-Dimensional Morphing," *Journal of Intelligent Material Systems and Structures*, 21(2010), pp. 1737-53.

[19] Mehta, V., Frecker, M. and Lesieutre, G. A., 2008, "Contact-aided compliant mechanisms for morphing aircraft skin," *In Smart Structures and Materials 2008: Modeling, Signal Processing and Control for Smart Structures*, Proc. SPIE 6926, pp. 1-12.

[20] Wang, A. J. and McDowell, D. L., 2004, "In-plane stiffness and yield strength of periodic metal honeycombs," *Journal of Engineering Materials and Technology-Transactions of the Asme*, 126(2), 137-156.

[21] Alderson, A. and Alderson, K. L., 2007, "Auxetic materials," *Proceedings of the Institution of Mechanical Engineers Part G-Journal of Aerospace Engineering*, 221(G4), 565-575.

[22] Scarpa, F., Panayiotou, P. and Tomlinson, G., 2000, "Numerical and experimental uniaxial loading on in-plane auxetic honeycombs," *Journal of Strain Analysis for Engineering Design*, 35(5), pp. 383-388.

[23] Theocaris, P. S., Stavroulakis, G. E. and Panagiotopoulos, P. D., 1997, "Negative Poisson's ratios in composites with star-shaped inclusions: A numerical homogenization approach," *Archive of Applied Mechanics*, 67(4), 274-286.

[24] Howell, L. L., 2002, *Compliant Mechanisms*, John Wiley & Sons, Inc.

[25] Mankame, N. D. and Ananthasuresh, G. K., 2007, "Synthesis of contact-aided compliant mechanisms for non-smooth path generation," *International Journal for Numerical Methods in Engineering*, 69(12), pp. 2564-2605.

[26] Mankame, N. D. and Ananthasuresh, G. K., 2004, "Topology optimization for synthesis of contact-aided compliant mechanisms using regularized contact modeling," *Computers & Structures*, 82(15-16), 1267-1290.

[27] Guerinot, A. E., Magleby, S. P., Howell, L. L. and Todd, R. H., 2005, "Compliant joint design principles for high compressive load situations," *Journal of Mechanical Design*, 127(4), pp. 774-781.

[28] Cannon, J. R. and Howell, L. L., 2005, "A compliant contact-aided revolute joint," *Mechanism and Machine Theory*, 40(11), pp. 1273-1293.

[29] Aguirre, M. E., Hayes, G., Frecker, M., Adair, J. H. and Antolino, N. E., 2008, "Fabrication and design of a nanoparticulate enabled micro forceps", ASME 2008 International Design Engineering Technical Conferences & Computers and Information in Engineering Conference. New York City, NY, USA.

[30] Mehta, V., Frecker, M. and Lesieutre, G. A., 2009, "Stress Relief in Contact-Aided Compliant Cellular Mechanisms," *Journal of Mechanical Design*, 131(9), pp. 1-11. *Journal of the American Ceramic Society*, 92(1), pp. S70-S78.

[31] Aguirre, M., G. Hayes, R. Meirom, M. Frecker, C. Muhlstein, and J. Adair, 2011. "Optimal Design and Fabrication of Narrow-Gauge Compliant Forceps," *ASME Journal of Mechanical Design,* 133(8), DOI: 10.1115/1.4004539

[32] Cirone, S., 2011, "Design, Fabrication and Testing of Contact-Aided Compliant Cellular Mechanisms with Curved Walls ", Thesis, The Pennsylvania State University.

[33] Zhou, H. and Ting, K., 2006, "Shape and size synthesis of compliant mechanisms using wide curve theory," *Journal of Mechanical Design*, 128, pp. 551-558.

[34] Xu, D. and Ananthasuresh, G. K., 2003, "Freeform skeletal shape optimization of compliant mechanisms," *ASME Journal of Mechanical Design*, 125(2), pp. 253-61.

[35] Heule, M. and Gauckler, L. J., 2001, "Gas sensors fabricated from ceramic suspensions by micromolding in capillaries," *Advanced Materials*, 13(23), 1790-1793.

[36] Maeda, R., Tsaur, J. J., Lee, S. H. and Ichiki, M., 2004, "Piezoelectric microactuator devices," *Journal of Electroceramics*, 12(1-2), 89-100.

[37] Christian and Kenis, P. J. A., 2007, "Fabrication of ceramic microscale structures," *Journal of the American Ceramic Society*, 90(9), 2779-2783.

[38] Garino, T., Morales, A., Buchheit, T. and Boyce, B., 2002, The Fabrication of Stainless Steel Parts for MEMs, Sand Report. Albuquerque, New Mexico, Sandia National Laboratories.

[39] Zhu, Z. G., Hassanin, H. and Jiang, K., 2010, "A soft moulding process for manufacture of net-shape ceramic microcomponents," *International Journal of Advanced Manufacturing Technology*, 47(1-4), 147-152.

[40] Imbaby, M. F. and Jiang, K., 2009, "Stainless Steel-Titania Composite Micro Gear Fabricated by Soft Moulding and Dispersing Technique," *Journal of Microelectronic Engineering*, 87(2010), 1650-1654.

[41] Evans, K. E. and Caddock, B. D., 1989, "Microporous Materials with Negative Poisson Ratios .2. Mechanisms and Interpretation," *Journal of Physics D-Applied Physics*, 22(12), 1883-1887.

[42] Levy, O., Krylov, S. and Goldfarb, I., 2006, "Design considerations for negative Poisson ratio structures under large deflection for MEMS applications," *Smart Materials & Structures*, 15(5), 1459-1466.

[43] Jackman, R. J., Brittain, S. T. and Whitesides, G. M., 1998, "Fabrication of three-dimensional microstructures by electrochemically welding structures formed by microcontact printing on planar and curved substrates," *Journal of Microelectromechanical Systems*, 7(2), pp. 261-266.

[44] Hawkins, G. F., O'Brien, M., Zaldivar, R. and von Bremen, H., 2002, "Machine-augmented composites", SPIE - The International Society for Optical Engineering. San Diego, CA, USA.

[45] Rothenburg, L. and Bathurst, R. J., 1991, "Microstructure of isotropic materials with negative Poisson's ratio," *Nature*, 354(6353), pp. 470-2.

[46] Heule, M., Vuillemin, S. and Gauckler, L. J., 2003, "Powder-based ceramic meso- and microscale fabrication processes," *Advanced Materials*, 15(15), 1237-1245.

[47] Madou, M. J., 2004, "Microfabrication challenge," *Analytical and Bioanalytical Chemistry*, 378(1), 11-14.

[48] Frazier, A. B., Warrington, R. O. and Friedrich, C., 1995, "The Miniaturization Technologies - Past, Present, and Future," *Ieee Transactions on Industrial Electronics*, 42(5), 423-430.

[49] Clark, T. D., Tien, J., Duffy, D. C., Paul, K. E. and Whitesides, G. M., 2001, "Self-assembly of 10-um-sized objects into ordered three-dimensional arrays," *Journal of the American Chemical Society*, 123(31), pp. 7677-7682.

[50] Xia, Y. N. and Whitesides, G. M., 1998, "Soft lithography," *Annual Review of Materials Science*, 28, 153-184.

[51] Heule, M., Schonholzer, U. P. and Gauckler, L. J., 2004, "Patterning colloidal suspensions by selective wetting of microcontact-printed surfaces," *Journal of the European Ceramic Society*, 24(9), pp. 2733-9.

[52] Zhao, X. M., Xia, Y. and Whitesides, G. M., 1996, "Fabrication of three-dimensional microstructures: Microtransfer molding," *Advanced Materials*, 8(10), pp. 837-840.

[53] Lewis, J. A., Smay, J. E., Stuecker, J. and Cesarano, J., 2006, "Direct ink writing of three-dimensional ceramic structures," *Journal of the American Ceramic Society*, 89(12), 3599-3609.

[54] Chrisey, D. B., 2000, "The power of direct writing," *Science*, 289(5481), pp. 879-81.

[55] Knitter, R., Gohring, D., Risthaus, P. and Hausselt, J., 2001, "Microfabrication of ceramic microreactors," *Microsystem Technologies*, 7(3), pp. 85-90.

[56] Schonholzer, U. P., Hummel, R. and Gauckler, L. J., 2000, "Microfabrication of ceramics by filling of photoresist molds," *Advanced Materials*, 12(17), pp. 1261-3.

[57] Lawes, R. A., 2007, "Manufacturing costs for microsystems/MEMS using high aspect ratio microfabrication techniques," *Microsystem Technologies*, 13(1), pp. 85-95.

[58] Hayes, G. R., 2011, "Mesoscale Fabrication and Design", Dissertation, The Pennsylvania State University.

[59] Cohen, A. L., 2002, Method for Electrochemical Fabrication. Patent, U. USA. 6,475,369,B1.

[60] Yuangyai, C., Nembhard, H. B., Hayes, G., Antolino, N. and Adair, J. H., 2009, "Yield Improvement for Lost Mold Rapid Infiltration Forming Process by a Multi-Stage Fractional Fractorial Split Plot Design," *International Journal of Nanomanufacturing*, 3(4), 351-367.

[61] Antolino, N. E., Hayes, G., Kirkpatrick, R., Muhlstein, C. L., Frecker, M. I., Mockensturm, E. M. and Adair, J. H., 2009, "Lost Mold Rapid Infiltration Forming of Mesoscale Ceramics: Part 1, Fabrication," *Journal of the American Ceramic Society*, 92(1), pp. S63-S69.

[62] Antolino, N. E., Hayes, G., Kirkpatrick, R., Muhlstein, C. L., Frecker, M. I., Mockensturm, E. M. and Adair, J. H., 2009, "Lost Mold-Rapid Infiltration Forming of Mesoscale Ceramics: Part 2, Geometry and Strength Improvements," " *Journal of the American Ceramic Society*, 92(1), pp. S70-S78.

[63] Hayes, G., M. Frecker, and J. Adair, 2011. Fabrication of Compliant Mechanisms on the Mesoscale. *Mechanical Sciences*, 2, pp. 129-137

[64] Ajdari, A., Nayeb-Hashemi, H., and Vaziri, A., 2011, "Dynamic Crushing and energy absorption of regular, irregular and functionally graded cellular solids," *International Journal of Solids and Structures*, 48, pp. 506-516.

[65] Schultz, J., Griese, D., Shankar, P., Summers, J.D., Ju, J., and Thompson, L., 2011, "Optimization of Honeycomb Cellular Meso-Structures for High Speed Energy Absorption ", ASME 2011 International Design Engineering Technical Conferences & Computers and Information in Engineering Conference. Washington, DC, USA.

[66] Ju, J., and Summers, J.D., 2011, "Shear Compliant Hexagonal Cellular Solids with a Shape Memory Alloy," ASME 2011 International Design Engineering Technical

Conferences & Computers and Information in Engineering Conference. Washington, DC, USA.

[67] Zou, Z., Reid, S.R., Tan, P.J., Li, S., and Harrigan, J.J., 2009, "Dynamic crushing of honeycombs and features of shock fronts," *International Journal of Impact Engineering*, 36, pp. 165-176.

[68] Hu, L.L., and Xu, T.X., 2010, "Dynamic crushing strength of hexagonal honeycombs," *International Journal of Impact Energy,* 37, pp. 467-474.

[69] Zarei, H. and Kroger, M., 2008, "Optimum honeycomb filler crash absorber design," *Materials and Design,* 29, pp. 193-204.

[70] Li, K., Gao, X.-L., and Wang, J., 2007, "Dynamic crushing behavior of honeycomb structures with irregular cell shapes and non-uniform cell wall thickness," *International Journal of Solids and Structures,* 44, pp. 5003-5026.

[71] Atli-Veltin, B. and Gandhi, F., 2010, "Effect of Cell Geometry on Energy Absorption of Honeycombs Under In-Plane Compression," *AIAA Journal,* 48(2), pp. 466-478.

[72] Reddy, B., Naik, S., and Saxena, A., 2012, "Systematic Synthesis of Large Displacement Contact-Aided Monolithic Compliant Mechanisms," *ASME Journal of Mechanical Design,* 134(1), DOI: 10.1115/1.4005326

[73] Cirone, S., Hayes, G., Babcox, B., Frecker, M., Adair, J., and G. Lesieutre, 2011. Design, fabrication and testing of contact-aided compliant cellular mechanisms with curved walls. *Proceedings SPIE 18th International Symposium on Smart Structures and Materials*, San Diego, CA, March, 2011

[74] Davis, Joseph R. Tensile Testing. Materials Park: ASM International, 2004. Print.

[75] Wang, Y., Xue, P., Wang, J.P., "Comparing study of energy-absorbing behavior for honeycomb structures," *Key Engineering Materials*, v 462-463, p 13-17, 2011, *Fracture and Strength of Solids VII*